

UNIVERSITY OF CALGARY

Nanophotonic Optomechanical Devices for Torque Magnetometry

by

Marcelo Wu

A THESIS

SUBMITTED TO THE FACULTY OF GRADUATE STUDIES
IN PARTIAL FULFILLMENT OF THE REQUIREMENTS FOR THE
DEGREE OF DOCTOR OF PHILOSOPHY

GRADUATE PROGRAM IN PHYSICS AND ASTRONOMY

CALGARY, ALBERTA

NOVEMBER, 2016

© Marcelo Wu 2016

Abstract

Torque magnetometry is a powerful and sensitive method for studying intricate mesoscopic magnetic events inside magnetic materials using nanomechanical resonators. Over the years, the field of cavity optomechanics has demonstrated ever increasing sensitivity, with measurements limited by the quantum motion of a device possible in state-of-the-art devices. In this thesis, a nanophotonic cavity is integrated into a nanomechanical resonator for optomechanical detection of torque driven by the interaction of a permalloy island with applied magnetic fields. This marks the first time where a nanocavity optomechanical sensor is applied to a nanoscale condensed matter system. This cavity optomechanics platform enabled torque magnetometry measurements to be performed with sufficient sensitivity for detection of Barkhausen features that were previously undetected in ambient conditions. The device was used to demonstrate a new form of nanomechanical radio-frequency susceptometry where enhanced magnetic susceptibility associated with single pinning and depinning events of a magnetic vortex core were observed. This optomechanical device increased torque magnetometer sensitivity by over an order of magnitude.

The torque sensitivity of the device derives from the optimization of the optomechanical interactions in a photonic crystal split-beam cavity. Two types of dissipative optomechanical couplings were observed as a result of the mechanical motion modulating the intra-cavity photon lifetime and the cavity input-output coupling rate. Interference between dissipative and dispersive optomechanical mechanisms enhance detection sensitivity and generate mechanical-mode-dependent optomechanical wavelength response. Dissipative coupling of up to ~ 500 MHz/nm and dispersive coupling of 2 GHz/nm, enables measurement of sub-pg torsional and cantilever-like mechanical resonances with a thermally-limited torque detection sensitivity of 1.2×10^{-20} Nm/ $\sqrt{\text{Hz}}$ in ambient conditions. Tuning of both dissipative and dispersive optomechanical couplings is also demonstrated through renormalization of

the cavity field mediated by its evanescent interaction with a fiber taper near-field probe. Strategic fiber taper placement allows for reconfiguration of the dominant optomechanical transduction mechanism and spatially selective optical readout of mechanical resonances such as out-of-plane cantilever modes suitable for sensing applications.

For the glory of God

Acknowledgements

Great are the works of the Lord; they are pondered by all who delight in them.

- Psalm 111:2

I would like to express my thanks to my family, friends, and colleagues who have made exceptional my journey toward a doctoral degree.

To my supervisor Paul, thank you for sharing your vast knowledge and experience with us. I am still amazed by your deep and detailed insights from the rich physics behind a theory to the exact parameters required for inducing plasma inside an etching chamber. Thank you for your patience in my (slow) development as a researcher.

To my labmates Behzad, Matt, and Chris, it was an honor to build the lab from scratch with you. Our days of sitting in a row by our experimental setup are over and, hopefully, so are the annual lab flooding events. To the Barclaylab group (adding Hamid, David, Thomas, Tamiko, and JP), thank you for making my time in the office memorable. To Hari in New York, I still cannot believe you put two dimpled fiber taper on one holder. To Adam, Mike, Deborah, Shantel, Jeremy, Lais, Davor, Guilhem, and many other undergraduates who graced the floor of our lab, best of luck in your future endeavors.

I am forever indebted to Aaron and Nathanael. Your contributions to my project was immense as well as your friendship. A big thank you is order for Mark Freeman's team: Joe, Miro, Tayyaba, and Fatemeh. You made me appreciate a whole new field of research. Thank you for the great team effort for the magnetometry project and your contagious enthusiasm.

I would like to thank all the people working hard behind the scenes who make everything run smoothly. To Nancy (IQST), Tracy, Leslie, Gerri, Camilla and the PHAS administrative gang, thank you for years of faithful service. To Scott, Jolene, Stephanie, Keith, Eric, Melissa, and the UofA nanoFab staff, thank you for your help with fabrication and for making me enjoy donning a bunny suit. To Rob and Mike in the NINT nanoFab, thank you for taking

care of the etcher; without it, our projects would come to a standstill. To Estella, Zarina, and the NINT administration, thank you for helping us navigate the red tape. To the expert machinists in the science workshop at UofC, thank you for the beautifully made acrylic box and fiber holders. To Dave, thank you for the amazing 3D printed sample holders and for troubleshooting the software in our lab in NINT.

To the members of the UofA and UofC nanoGroups, the PHAS DGA, and COPSS (formerly the UofC OSA/SPIE student chapter), there are too many of you to name but it was a pleasure to serve alongside you. I am looking forward to see you grow the team and organization in the years to come.

To my church community in Calgary and friends across the province and beyond, thank you for all the fond memories we have made. My time in Alberta always felt warm even in the midst of a cold winter storm. I am thankful for your gift of friendship.

Finally, I would like to thank my family, both in Calgary and Montreal, for your support and your blessing. To Elaine and my little boy Lochlan, you are a source of encouragement to no end. Thank you for putting up with me.

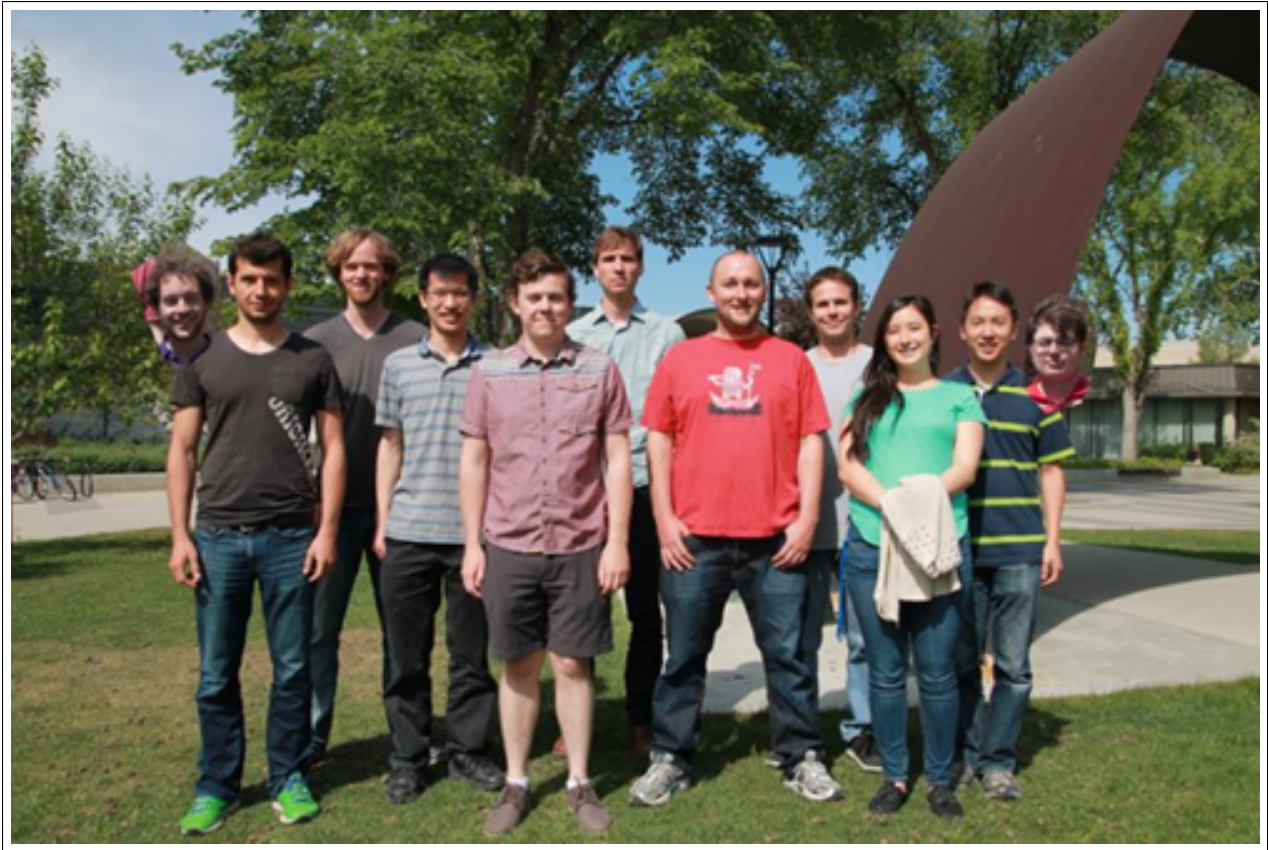


Figure 0.1: Group photo of BarclayLab taken in the summer of 2015. From left to right: Thomas, Behzad, David, Nathanael, Matt, Paul, J.P., Chris, Tamiko, Marcelo, Hamid.

Table of Contents

Abstract	i
Acknowledgements	iv
Table of Contents	vii
List of Tables	ix
List of Figures	x
List of Abbreviations	xii
1 Introduction	1
2 Optomechanical torque sensing	11
2.1 Concept	11
2.2 Torque	12
2.3 Mechanics	12
2.4 Optomechanics	14
2.5 Optics	15
2.6 Noise & measurement electronics	17
2.7 Sensitivity	22
2.8 Torque actuation	26
2.9 Challenges of higher frequency operation	27
2.10 Summary	28
3 Split-beam cavities: design, fabrication, characterization	30
3.1 Nanobeam photonic crystal cavity	30
3.2 Design philosophy for split-beam cavities	33
3.3 Nanofabrication of split-beam cavities	40
3.4 Fiber taper measurement setup	43
3.5 Split-beam cavity device characterization	49
3.6 Summary and implications	52
4 Dissipative and dispersive optomechanics	54
4.1 Origin of dissipative optomechanical coupling	54
4.2 Theory of dissipative and dispersive optomechanical coupling	56
4.3 Experimental observation of dissipative coupling	59
4.4 Numerical simulations of optomechanical couplings	62
4.5 Applications of dissipative optomechanics	64
4.6 Summary and implications	65
5 Tuning of dissipative and dispersive optomechanical coupling	67
5.1 Optical field renormalization using near-field fiber probe	67
5.2 Quarter-wave shifted photonic crystal cavities	69
5.3 Characterization of QWS optomechanical devices	70
5.4 Experimental tuning of optomechanical couplings using near-field fiber probe	73
5.5 Analysis of dissipative and dispersive optomechanical couplings	75
5.6 Perturbative approximations for dispersive and dissipative-external couplings	81
5.7 Dissipative – dispersive coupling transition via axial fiber motion	84
5.8 Summary and implications	85
6 Torque magnetometry	87

6.1	Micromagnetic theory	87
6.2	Torque magnetometry: experimental preparation	92
6.3	Torque magnetometry measurements	100
6.4	Summary and implications	120
	Conclusion	122
	Bibliography	125
A	List of publications	147
B	Numerical simulations using COMSOL	148
C	Signal processing	154
D	Nanofabrication tools and processes	156
E	Coupled mode theory including indirect coupling	162
F	Copyright permissions	164

List of Tables

3.1	Mechanical properties of SBC device	50
6.1	Torque terms for magnetization and susceptibility	115

List of Figures and Illustrations

0.1	BarclayLab group photo	vi
1.1	Torque magnetometry	3
1.2	Cavity optomechanics	7
2.1	Optomechanics concept	11
2.2	Optomechanical coupling schemes	15
2.3	Optics	16
2.4	Power spectral density conversions	21
2.5	Displacement and torque sensitivity graphs	23
2.6	Sensitivity graphs with driving torque	26
2.7	Ratio of ϕ	28
3.1	Photonic crystal cavity	31
3.2	PCC with near-field paddle	32
3.3	Split-beam cavity design	34
3.4	Wavelength vs. nanobeam width	36
3.5	Dispersion diagram for SBC	37
3.6	Mirror strength for tapering elliptical holes	38
3.7	First cycle of nanofabrication	40
3.8	Fabricated SBC device	41
3.9	Stiction	43
3.10	Fiber taper measurement setup	44
3.11	Fiber pulling station	45
3.12	Ceramic blade	46
3.13	Dimpled fiber taper	46
3.14	Fiber taper holder	47
3.15	Fiber taper measurement setup	48
3.16	Characterization of SBC device	49
3.17	Optomechanical signal and sensitivity	51
4.1	Optomechanics schematic including dissipative couplings	55
4.2	Dissipative/dispersive coupling schematics	56
4.3	Relative amplitude of dissipative/dispersive couplings	58
4.4	Experimental observation of dissipative coupling	60
4.5	Numerical simulation of optomechanical couplings	62
5.1	Cavity field renormalization	68
5.2	QWS device design	69
5.3	Fabricated QWS device	70
5.4	Characterization of QWS device	72
5.5	Selective mechanical mode detection using fiber taper	73
5.6	Tuning of optomechanical couplings	74

5.7	Q_o and $\Delta\lambda/\lambda$ at various fiber heights	77
5.8	Numerical simulations of dissipative/dispersive couplings vs fiber taper height	78
5.9	Electric field profiles of device and fiber taper	81
5.10	Dispersive coupling vs. fiber taper height	83
5.11	Dissipative coupling vs coupling and fiber length	84
5.12	Dissipative/dispersive coupling vs fiber axial position	85
6.1	Magnetic domains and walls	90
6.2	Magnetic vortex state	90
6.3	Pinning site	91
6.4	Second cycle of nanofabrication	93
6.5	Fabricated SBC device with permalloy	94
6.6	Measurement setup with magnetometry	96
6.7	Lab pictures of magnetometry measurement setup	97
6.8	Optomechanical signal of SBC device with permalloy	99
6.9	Sensitivity of SBC device with permalloy	102
6.10	Magnetic moment sensitivity	103
6.11	Broadband mechanical spectra	104
6.12	Magnetization hysteresis curve	109
6.13	Other SBC devices with permalloy	110
6.14	Magnetic field from coil in tilted position	111
6.15	Susceptibility peaks	112
6.16	Quantitative analysis of susceptibility peaks	117
6.17	DC bias field direction and thermo-optic heating	118
6.18	Transmission line platform	119
B.1	Comsol: optical and mechanical breathing modes	148
B.2	Comsol: model and variables	149
B.3	Comsol: optics to mechanics	150
B.4	Comsol: derived values	151
B.5	Comsol: effective mass	152
B.6	Comsol: join operation	153
F.1	APS-copyright	164
F.2	OSA-copyright	164
F.3	NNano-copyright	165

List of Abbreviations and Nomenclature

Abbreviation	Definition
AC	Alternative current
DC	Direct current
ECERF	Electrical & Computer Engineering Research Facility
EBL	Electron beam lithography
FDTD	Finite difference time domain
FEA	Finite element analysis
GDSII	Graphic database system 2
GPU	Graphics processing unit
HF	Hydrofluoric acid
ICPRIE	Inductive coupled plasma RIE
IPA	Isopropyl alcohol (not India pale ale)
IQST	Institute for Quantum Science and Technology
LLG	Landau-Lifshitz-Gilbert
MEMS	Micro-electromechanical systems
MIBK	Methyl isobutyl ketone
Nanofab	Nanofabrication facility
NEMS	Nano-electromechanical systems
NOMS	Nano-optomechanical systems
NINT	National Institute for Nanotechnology
NV	Nitrogen vacancy
PCC	Photonic crystal cavity
PHAS	Department of Physics & Astronomy
PMMA	Poly methyl methacrylate

PSD	Power spectral density
Py	Permalloy
QED	Quantum electrodynamics
QWS	Quarter-wave shifted
RBW	Resolution bandwidth
RF	Radiofrequency
RIE	Reactive ion etching
RMS	Root mean squared
RSA	Real-time spectrum analyzer
SBC	Split-beam cavity
SEM	Scanning electron microscope
SEMPA	Scanning electron microscope with polarization analysis
Si	Silicon
SiO ₂	Silicon dioxide or silica
SNR	Signal-to-noise ratio
SOI	Silicon-on-insulator
SQUID	Superconducting quantum interference device
TE	Transverse electric
UofA	University of Alberta
UofC	University of Calgary
UV	Ultraviolet light
ZED	Zeon electron-beam developer
ZEP	Zeon electron-beam positive

Chapter 1

Introduction

Project background

This doctoral thesis is the culmination of collaborative efforts between two research groups: the nanophotonics and optomechanics group of Dr. Paul Barclay at the University of Calgary (UofC) and the magnetometry group of Dr. Mark Freeman at the University of Alberta (UofA). The impetus for this work was to improve the sensitivity of torque magnetometry measurements by using a cavity optomechanical platform. Our goal was to design, fabricate, and characterize a cavity optomechanical device with sensitivity tailored for torsional measurement of magnetization from a nanoscale magnetic sample. Throughout our endeavors, various device designs were developed as each iteration was optimized from lessons learned previously. New optomechanical phenomena were discovered along the way and, in deciphering them, helped us understand interactions uniquely affecting our devices and measurement setup. Finally, we succeeded in incorporating magnetic material on our device, opening the door to optomechanical torque magnetometry measurements. These include observation of magnetic vortex dynamics and Barkhausen jumps as well as quantitative measurements of magnetization and susceptibility, all in ambient conditions. Many of these phenomena are typically observed in a vacuum setup, in a large ensemble, or in bulk magnetic material. Here, our experiments at room temperature and pressure are sensitive enough to provide high resolution signal of an individual mesoscopic magnetic structure. This collaboration has brought together two seemingly separate research fields, optomechanics and nanomagnetism, with fruitful results for both scientific communities.

Torque magnetometry

Historical perspective

Measurements of mechanical torque or rotation played an important role in both fundamental and experimental physics throughout history. In the 18th century, Coulomb made use of a torsional balance to measure repulsion between two charged spheres with one hanging by a torsion wire [1]. This experiment led him to postulate the famous Coulomb's law of electrostatic force. At the end of the century, Cavendish used a larger version of the torsional balance to measure attraction between massive spheres [2]. His experiment successfully estimated the mass of the earth while paving the way to future experiments to determine the gravitational constant as well as Newton's law of gravitational force.

As modern physics expanded at the beginning of the 20th century, Einstein and a few of his contemporaries explored the relationship between magnetism and angular momentum. In 1915, Barnett discovered that spinning a ferromagnet induces magnetization in it [3]. In the same year, Einstein and de Haas found the reciprocal effect where a change in magnetization induces rotation [4]. Both experiments established the relationship between spin angular momentum and mechanical angular momentum. Further studies by researchers led to the constant called the gyromagnetic or magnetomechanical ratio. These experiments and many other developments throughout the century formed the basis of advancements in magnetism including torque magnetometry [5].

Basic operation

The principle behind torque magnetometry as illustrated in Fig. 1.1 relies on detecting the deflection of a mechanical structure due to the angular momentum transfer from magnetic torques $\boldsymbol{\tau} = \mathbf{m} \times \mu_0 \mathbf{H}$ where μ_0 is the permeability of free space. This torque $\boldsymbol{\tau}$ is generated when magnetic moments in the material, \mathbf{m} , experience an orthogonally applied magnetic

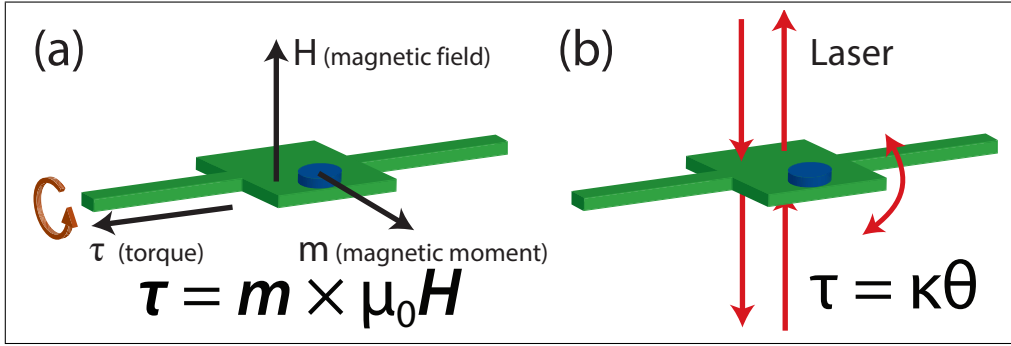


Figure 1.1: Schematic of the basic operation of torque magnetometry. (a) A sample of magnetic material (in blue) attached to a mechanical resonator, represented here by a paddle with torsion rod, is magnetized using an external magnetic field. Its magnetic moment m interacts with the drive field H to impart a torque τ in a direction perpendicular to both. (b) The produced torque bends the mechanical resonator with torsional spring constant k generating a deflection θ on the paddle. In traditional torque magnetometry, its motion can then be detected, for example, via interferometry methods as shown here.

field, H . The moments can be magnetized, for example with the application of an external field from a permanent magnet or a set of Helmholtz coil, such that m aligns with the static magnetic field. The mechanical element is typically assumed to act as a harmonic resonator with natural frequency ω_m and is driven by the driving field $H(\omega)$. The torque transferred to the mechanical resonator will induce an angular deflection or rotation θ around a pivot axis proportional to the torsion spring constant k such that $\tau = k\theta$. This simple working principle gives directional information and insights on intricate magnetic interactions present inside the sample.

Modern magnetism

The field of magnetism has progressed immensely over the past century. Discoveries such as the giant magnetoresistance (GMR) effect made it clear that exploration of the fundamental interactions in magnetism can lead to widespread applications [6, 7]. In the case of GMR, research in nanoscale ferromagnetic multilayers resulted in practical applications such as hard disk drives, magnetic memories, and sensors [8, 9].

Current research interests are pushing to make technologies smaller, faster, and more energy efficient. To this effect, studies of magnetism are now turning towards micrometer and nanometer scale magnetic structures. Studies in micro- or nano-magnetism are now focused on nanoscale interactions within sub-nanosecond time scales [10]. The process of miniaturization is producing precisely engineered novel materials and structures with tailored magnetic properties for a wide variety of commercial and research applications such as magnetic memories, hard drives, and sensors. Rapid growth in the field has been facilitated by at least three factors. First, modern fabrication techniques for thin film deposition and lithographic patterning are allowing production of innovative devices with large scale arrays of magnetic elements and multilayer complexity. Second, in order to characterize these devices, new technologies for detecting signals and imaging samples were developed [11]. And finally, but not exhaustively, memory-intensive micromagnetic simulations were enabled by the exponential rise of the computational power of computers.

The path to progress will require much effort in advancing our basic understanding and control of magnetic interactions along with the aforementioned developments. Many are coining this new field of physics as spintronics [12]. And rightly so, the ultimate challenge would be the ability to fully manipulate properties of magnetic materials at the level of single spins using the least amount of energy on the smallest overall footprint.

Modern torque magnetometry

The power of torque magnetometry resides on the fact that mechanical resonators can directly reveal effects that are otherwise difficult to observe. The detection of the torsional motion has been done historically with the naked eye and a ruler, as in the Coulomb and Cavendish experiments. Advanced torque magnetometry measurements can be made using a laser deflecting on the torsional element on which an attached piece of ferromagnet is magnetized under applied fields. Determining the magnetocrystalline anisotropy of magnetic samples was one of its most useful applications [13]. However, as smaller displacements re-

quired increased sensitivity, new methods have risen to study magnetic mesostructures with torque magnetometry falling out of favor in the middle of the 20th century.

It was not until the evolution to nanomagnetism and the advent of miniaturization that the field saw a resurgence. Modern interpretations of the torsional balance are in the form of nanoscale mechanical devices [14–16]. Their low mass and high mechanical quality factor (Q_m) enhance the response of nanomechanical resonators and have improved their sensitivity greatly. These freestanding devices, often called micro and nano electro-mechanical systems (MEMS and NEMS), can be integrated inside semiconductor device architectures and thus benefit from the latest advanced nanofabrication processes. For magnetometry, the miniaturization of the mechanical system increased detection sensitivity to ever smaller volumes of magnetic material including thin films [17], mesoscale confined geometries that are deposited [16] or epitaxially grown [18], and small aggregates of nanoparticles [19]. The marriage with integrated circuits made studies using torque magnetometry methods versatile for a variety of applications from sensing to memories [20].

The high detection sensitivity of resonant mechanical torsional devices has allowed for minimally-invasive observation of nanoscale magnetostatic interactions and net magnetization hysteresis [16]. Going beyond the static limit, nanomechanical torque magnetometry has been extended to timescales allowing for detection of slow thermally-activated dynamics [21], AC susceptibility [18], and magnetic resonance [22, 23]. As a complementary technique to many others in the field of magnetism, torque magnetometry is unique in its ability to directly measure torque via the net magnetization of individual magnetic elements instead of an ensemble or local array. This method is thus broadband and allows for both DC and AC ranges of magnetic fields of theoretically any strength. Ultimately, torque magnetometers can effectively probe the unique magnetic fingerprint of single thin film elements by measuring the magnetization and susceptibility responses with high sensitivity.

Limitations of torque magnetometry

Current state-of-the-art torque magnetometry measurements employ free-space laser interferometry as a readout technique to detect the mechanical displacement of the torsional device with torsional sensitivities near 10^{-19} Nm/ $\sqrt{\text{Hz}}$ [16, 21, 23]. A side effect of miniaturization is the double roadblock of the optical diffraction limit and reduction in the number of magnetic spins. The first occurs when the dimensions of the device are scaled down below the laser spot size. The latter leads to smaller mechanical deflections which become increasingly difficult to detect. The Fabry-Perot-based interferometric detection scheme then begins to break down and sensitivity suffers [24].

Moreover, the low-finesse Fabry-Perot cavity formed between the nanomechanical resonator and its supporting substrate below provide only a weak enhancement (the optical quality factor Q_o is essentially one). Other issues include laser heating and sample drift due to laser focus spot which increase thermal noise and affect the magnetization. Migration to a more sensitive readout scheme is essential. The integration of a nanoscale optical cavity offers a natural path for improvement.

Cavity optomechanics for sensing

Cavity optomechanics integrates an optical cavity into a mechanical resonator. The simple schematic in Fig. 1.2(a) shows light with wavelength λ_o or resonant frequency ω_o confined inside a cavity coupled to a mechanical resonator with mechanical resonance frequency ω_m . The motion x of the mechanical resonator induces a change in the optical path length in the cavity which shifts ω_o . The amount of deviation in the optical resonance is characterized by the optomechanical coupling rate $g_{om} = \delta\omega_o/\delta x$. The amplitude of light exiting the cavity is modulated at the rate ω_m . The maximum optomechanical signal can be obtained by setting the probe wavelength on the shoulder (point of highest slope) of the optical resonance as

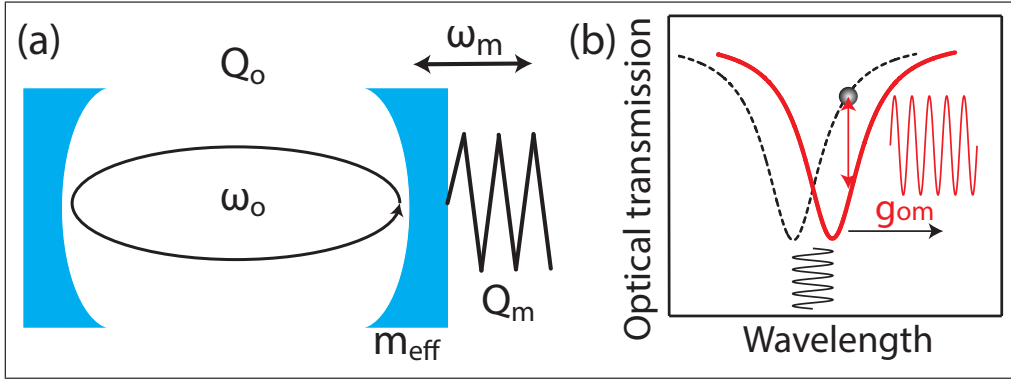


Figure 1.2: (a) Canonical picture for cavity optomechanical transduction. A high optical quality factor Q_o Fabry-Perot cavity resonantly confines light at optical frequency ω_o . One of the mirrors with effective mass m_{eff} is coupled to a mechanical resonator represented by a spring. The mechanical system vibrates at its resonant mechanical frequency ω_m associated with a mechanical quality factor Q_m . (b) Schematic of the optomechanical detection mechanism. The dotted line represents a typical optical resonance dip in the optical transmission versus wavelength with the cavity at rest. When the mirror moves, the resonance shifts to the red line. If a probe (grey ball) is placed at a particular wavelength, it will experience a change in amplitude. The vibration of the mechanical resonator effectively modulates the optical signal shown in the waveform in red.

depicted in Fig. 1.2(b) where the contrast in optical transmission is largest for a given shift in resonance. This optomechanical coupling arises from a dispersive dependence of the cavity resonance frequency on the cavity geometry which is modulated by mechanical excitations.

The strength of the output signal is proportional to g_{om} as well as Q_o which defines the sharpness of the optical resonance. The confinement and recirculation of light inside the cavity thus provide dual enhancement in the mechanical detection sensitivity of nanomechanical resonators which only relies on Q_m .

Note that the light inside the cavity can also push on the mechanical resonator. This radiation pressure can act as a driving force on the mechanics at the same coupling of g_{om} . However, for sensing purposes considered here, this force is not significant, except in extreme cases where backaction noise can limit precision.

Applications of cavity optomechanics

The recent miniaturization and implementation of integrated nanophotonics methods to localize light to sub-wavelength volumes in optomechanical devices has enhanced the coupling between optics (photons) and mechanics (phonons) to unprecedented levels [25–28]. Harnessing this optomechanical interaction has enabled milestone experiments, including ground-state cooling [29, 30] and other quantum mechanical phenomena [29, 31–36]. Understanding the behavior of light-matter interactions beyond the standard quantum limit [37–39] is at the heart of many technological and fundamental advances in physics and engineering including the observation of gravitational waves [40, 41]. The precise optical measurement and fine control of mechanical vibrations enabled by nanophotonic optomechanical devices have been exploited for sensing applications including detection of displacement [28, 42–46], force [47–49], acceleration [50], magnetic fields [51, 52], and torque [53–56].

Cavity optomechanics for torque magnetometry

It is therefore natural to consider enhancing the sensitivity of torque magnetometry by integrating an optical cavity into the nanomechanical system. Optomechanical transduction has many practical advantages over free-space interferometry techniques beyond the dual enhancement afforded by g_{om} and Q_{o} [24]. First, the size of the resonator is not as crucial as the design of the geometry which maximizes g_{om} . The response of the device can be high even with large resonators with large mass [50]. Optomechanical devices are also less affected by laser heating since most coupling mechanisms to an optical cavity involve a nearby waveguide or optical fiber. Finally, without free space laser light, the stability of the sample and interaction with the magnetic elements can be mitigated.

In this thesis, I will show how we designed, fabricated, and used an optomechanical device to sensitively detect torque produced by a nanomagnetic sample. By understanding and exploiting the optomechanical interactions within our device, we optimized the output

signal to push the limits of sensitivity in the field of torque magnetometry. We achieved torque sensitivity down to 10^{-20} Nm/ $\sqrt{\text{Hz}}$ in ambient conditions, surpassing that of free-space-optics nanomechanical implementations in vacuum by one order of magnitude [16]. The high sensitivity achieved by our device was used to observe various magnetic interactions of interest on our sample including the magnetization and susceptibility responses as well as fine Barkhausen steps. Our experiments open up new avenues to explore similar mesoscopic systems [57, 58].

Organization of the thesis

This thesis is organized as follows. Chapter 2 lays down the theoretical framework for sensitivity in cavity optomechanics for a torque sensor. We will then move to the design, fabrication, and characterization of our optomechanical device which is a split-beam nanocavity in chapter 3. Chapters 4 and 5 deal with the development of dissipative optomechanical couplings which play a major role in the operation of our devices. The first discusses the theory behind the interplay between dispersive and dissipative couplings as well as our experimental results. The latter chapter applies the previous knowledge to manipulate the ratio between the couplings using our fiber taper. Lastly, we optimize the optomechanical signal in our device incorporating a magnetic sample to perform torque magnetometry measurements in chapter 6. A short section on the theoretical background in micromagnetism, the fabrication steps with permalloy, and our seminal experimental results round up the chapter.

Contribution of co-authors

My supervisor, Dr. Paul Barclay, conceived and oversaw all the projects discussed in this thesis. While I was the main driving force behind those projects, including design, fabrication, and characterization of devices, laboratory setup, fiber-tapering, and numerical simulations,

much of the results and successes were achieved with the support of my colleagues. Dr. Aaron Hryciw led the project to design the split-beam cavities from nanobeam photonic crystal cavities. Many of his contributions are included in chapter 3 and 5. He also was an integral part in the fabrication and characterization of devices made at the University of Alberta (UofA) and the National Institute for Nanotechnology (NINT). Behzad Khanaliloo helped measuring large arrays of devices especially in the project detailed in chapter 5. Dr. Harishankar Jayakumar, Matthew Mitchell, Christopher Healey, and David Lake were great help in the laboratory especially for their technical assistance and fiber-tapering.

The main efforts of our collaboration with the team led by Dr. Mark Freeman is described in chapter 6. For the magnetometry project, Dr. Nathanael Wu helped in designing and fabricating the devices. Nathanael imaged the devices while I set up the measurement equipment including the fiber taper, coil, and permanent magnet. Nathanael, Tayyaba Firdous, and I took turns to perform measurements on the device. Then, all three of us plus Fatemeh Fani Sani analyzed the data. For the manuscript, Nathanael and I prepared figures. Tayyaba and Fatemeh contributed simulations. Fatemeh helped with the theoretical framework for the quantitative analysis of susceptibility peaks. Dr. Joseph Losby provided guidance and technical assistance with instrumentation and measurements.

Chapter 2

Optomechanical torque sensing

This chapter is designed to give a general theoretical background and practical tools to estimate the sensitivity and signal of a nanoscale optomechanical torque sensor from beginning to end. A noise analysis will be presented assuming a simple measurement setup and the signal-to-noise ratio can be calculated from realistic parameters.

2.1 Concept

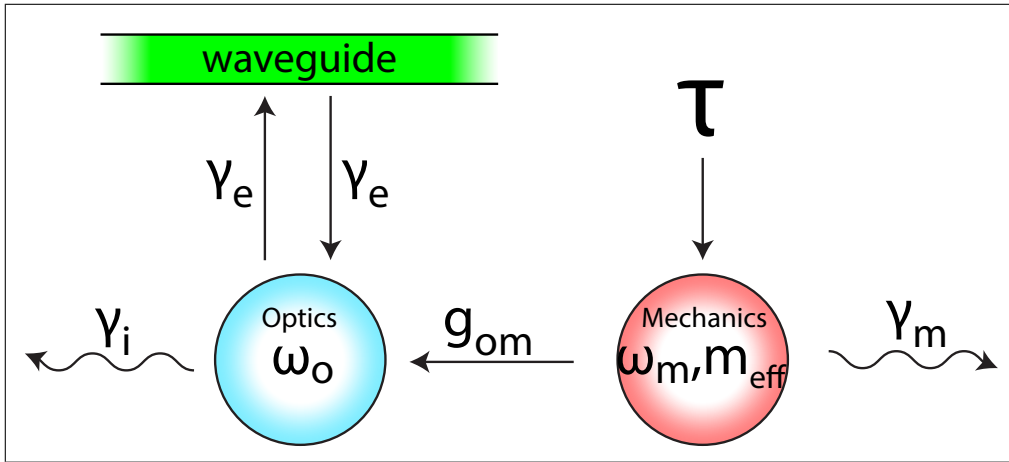


Figure 2.1: Operational schematic of an optomechanical system driven by an external source of torque τ . A torque exerted on an object of mass m_{eff} drives a mechanical resonator at frequency ω_m with a loss rate of γ_m . The mechanical motion is coupled to an optical cavity through the optomechanical coupling rate g_{om} which causes a shift in resonance frequency ω_o of a mode supported by the optical cavity with optical loss rate γ_i . The cavity couples to an external waveguide which provides input and output of light with a coupling rate of γ_e .

The general system for cavity optomechanics is composed of an optical cavity coupled to a mechanical resonator via the optomechanical coupling rate g_{om} (see schematic in Fig. 2.1). This dyad interacts with the external world in numerous ways. Here we focus on an applied

torque $\boldsymbol{\tau}$ that drives the mechanical resonator. Since the dyad exists within an environment, the mechanical resonator will experience losses (ex: thermal, mechanical, material, etc.) which is bundled as γ_m , limiting its mechanical quality factor to Q_m . Similarly, the optical cavity can couple to lossy modes via scattering, material losses, fabrication imperfections, and many other loss channels which limit its optical quality factor to Q_o . Finally, useful information can be gathered by allowing light to couple in and out of the cavity. In our case, we use a waveguide to represent a useful channel for excitation of the optical mode and readout of the optical signal. The optomechanical signal will be encoded within the optical transmission.

2.2 Torque

In the schematic (Fig. 2.1), a source of torque $\boldsymbol{\tau}$ drives the motion of the mechanical resonator. This torque can be driven by various sources such as magnetic torques. In this thesis, the focus will be on torque magnetometry in which the interaction of the magnetic moment \boldsymbol{m} of a magnetic material with an applied magnetic field \boldsymbol{H} produces a torque [16]:

$$\boldsymbol{\tau} = \boldsymbol{m} \times \mu_0 \boldsymbol{H}. \quad (2.1)$$

where μ_0 is the permeability of free space.

This torque will exert an equivalent force \boldsymbol{F} with distance \boldsymbol{r} away from the axis of rotation such that $\boldsymbol{\tau} = \boldsymbol{r} \times \boldsymbol{F}(\boldsymbol{r})$.

2.3 Mechanics

Assuming the source produces a harmonic driving force $\boldsymbol{F}(\boldsymbol{r}, t) = \boldsymbol{F}(\boldsymbol{r})e^{i\omega t}$, the torque will drive the mechanical mode \boldsymbol{u}_n . Here \boldsymbol{u}_n is the displacement field vector of mode n which is an eigenvector solution to the solid mechanics differential equation [59]. The mode generates

a displacement profile $x(\omega)$ of the resonator such that $x(\omega) = \chi_m(\omega)F(\omega)$. We assume that the resonator's motion can be reduced to a one-dimensional displacement function [60]. The mechanical susceptibility $\chi_m(\omega)$ is derived from the equation of motion for a harmonic oscillator and is defined as [25]:

$$\chi_m(\omega) = \frac{1}{m_{\text{eff}}[\omega_m^2 - \omega^2 - i\omega\omega_m/Q_m]} \quad (2.2)$$

where m_{eff} is the effective mass of the mechanical resonance and Q_m is the mechanical quality factor. Its maximum lies at the mechanical resonance where $|\chi_m(\omega = \omega_m)| = Q_m/(m_{\text{eff}}\omega_m^2)$.

The effective mass m_{eff} is a measure of the mass that contributes to the mechanical motion. The concept of mass may be difficult to define in bodies that are not fully freestanding but rather connected to a larger fixed object. In the example of a cantilever in flexural mode, the tip experiences maximum displacement. The motion then reduces progressively closer to the device layer but does not disappear entirely since mechanical “waves” might continue to propagate beyond. Drawing a boundary to define the mass is thus problematic. The effective mass is therefore akin to a “weighted” mass where more mass is attributed in places with larger displacement \mathbf{u} . The result is a volume integral that is normalized to the maximum displacement such that the effective mass can be written as [59]:

$$m_{\text{eff}} = \rho(r) \int \left(\frac{|\mathbf{u}|}{\max(|\mathbf{u}|)} \right)^2 dV \quad (2.3)$$

where ρ is the density of the material. The density is location dependent (r) to account for a mix of materials. The effective mass can be numerically computed via finite element analysis (FEA) using software such as COMSOL. Calculation of m_{eff} using simulations is detailed in appendix B. As an extension, an effective spring constant can be defined as $k_{\text{eff}} = m_{\text{eff}}\omega_m^2$. Since we work with torques, the effective moment of inertia and torsion constant can be given as $I_{\text{eff}} = r^2 m_{\text{eff}}$ and $J = I_{\text{eff}}\omega_m^2$, respectively.

2.4 Optomechanics

The optomechanical coupling can be derived from perturbation theory for Maxwell’s equations with shifting material boundaries [61]. The displacement $x(\omega)$ disturbs the optical cavity, resulting in a measurable change in the cavity optical frequency $\Delta\omega_o = g_{om}x(\omega)$ through the optomechanical coupling coefficient [59]:

$$g_{om} = \frac{\omega_o}{4} \int dA (\mathbf{u}_n \cdot \hat{\mathbf{n}}) \left[\Delta\varepsilon |\mathbf{e}_{\parallel}|^2 - \Delta(\varepsilon^{-1}) |\mathbf{d}_{\perp}|^2 \right] \quad (2.4)$$

where the integral is performed over the surface dA of the cavity and $\hat{\mathbf{n}}$ is the surface normal. The optomechanical coupling strength depends on the overlap of \mathbf{u} with the optical electric and displacement fields, \mathbf{e}_{\parallel} and \mathbf{d}_{\perp} , parallel and perpendicular to the cavity surface, respectively, and on the refractive index contrast of the optical cavity, $\Delta\varepsilon = \varepsilon_1 - \varepsilon_2$ and $\Delta(\varepsilon^{-1}) = \varepsilon_1^{-1} - \varepsilon_2^{-1}$, where $\varepsilon_{1,2}$ are the dielectric constants of the structure and the surrounding medium, respectively. The optomechanical coupling coefficient is often quoted in units of Hz/nm and the resulting shift $\Delta\omega_o$ is typically measured by monitoring the change in optical response of the cavity when it is excited by an external laser at frequency ω_l .

A strong optomechanical coupling rate g_{om} is beneficial for high sensitivity. This is achieved with high spatial overlap between the mechanical and optical fields with the appropriate symmetries [43, 59] as described by Eq. (2.4). High spatial overlap is enhanced when both optical and mechanical resonators are integrated within a single structure [28, 62]. The necessary symmetry conditions are satisfied by mechanical modes which result in a net change in the effective refractive index sensed by the optical field. Two examples of modes satisfying this condition are “breathing modes” (illustrated in Fig. 2.2(a)), which expand and contract the cavity volume [28, 30], and “offset modes” (illustrated in Fig. 2.2(d)) whose equilibrium position is misaligned with high symmetry points of the optical field orthogonal to the mechanical motion [44, 46, 47, 50]. The simplest mechanical modes suitable for optomechanical torques detection are flexural and in-plane “cantilever modes” [63], often

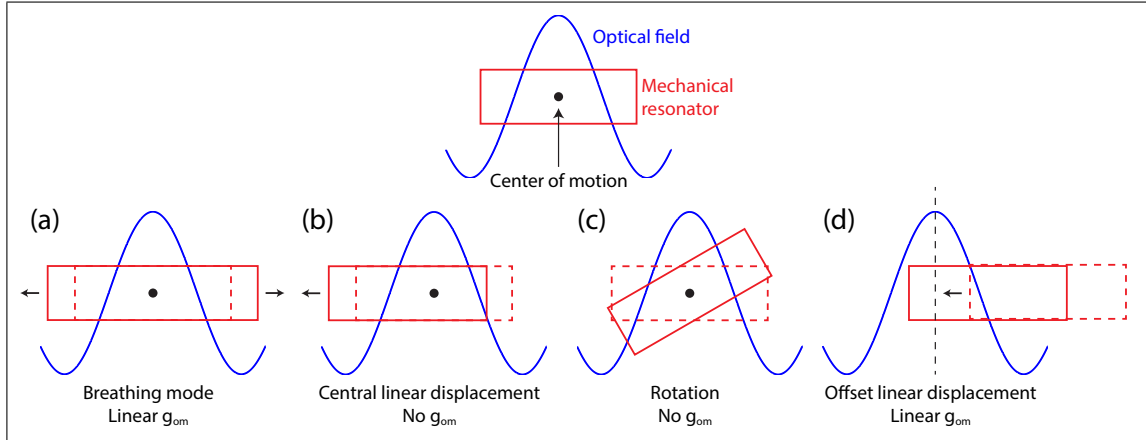


Figure 2.2: Schematic for various schemes for linear dispersive optomechanics. (a) Breathing mode: the mechanical motion deforms the optical cavity. (b) Central linear displacement: the mechanical motion moves away from center of the optical field. (c) Rotation: the mechanical motion rotates the cavity at the central axis. (d) Offset linear displacement: the mechanical motion moves from an offset position to the center of the optical field.

used for magnetometry purposes [15, 64]. Calculation of the optomechanical coupling using numerical simulations can be found in appendix B.

Note that the above treatment of optomechanics only involves moving boundaries. An alternative pathway for mechanics to influence optics is via the photoelastic effect (denoted by g_{pe}) where mechanical stresses can cause birefringence therefore changing the refractive index [62, 65]. This effect is prevalent in breathing modes and might be a potential venue for torsional optomechanics if suitable geometries for devices can be found [56, 66]. In this work, the location of stress in our device is far from the optical mode hence its effect on the total optomechanical coupling is minimal.

2.5 Optics

We now focus on the optical part of the optomechanical system where the cavity couples to an external waveguide such as a fiber or built-in waveguide with rate γ_e . The cavity itself couples to the environment via intrinsic losses at rate γ_i . In Fig. 2.3(a), we assume double-

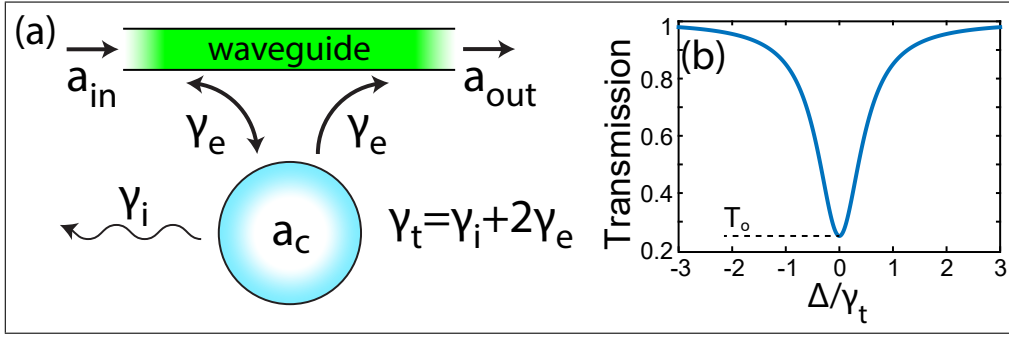


Figure 2.3: (a) Schematics of the cavity-waveguide system with double-sided coupling. (b) Plot of the normalized transmission on the output of a waveguide after coupling to a cavity with $\gamma_e/\gamma_i = 0.5$.

sided coupling where the cavity couples to both the forward and backward propagating directions in the waveguide such that the total loss rate $\gamma_t = \gamma_i + 2\gamma_e$.

To model the behaviour of the optical cavity and the output signal, we start with the boundary equation that relates the output field a_{out} to the input field a_{in} with its interaction with the cavity field a_c [67, 68]:

$$a_{\text{out}} = a_{\text{in}} + \kappa a_c \quad (2.5)$$

where the coefficient $\kappa = -\kappa^* = i\sqrt{\gamma_e}$ characterizes the waveguide-cavity coupling. The field inside the cavity is then defined by the equation of motion for a_c [25]:

$$\frac{da_c}{dt} = -\left(i\Delta + \frac{\gamma_t}{2}\right) a_c + \kappa a_{\text{in}} \quad (2.6)$$

where $\Delta = \omega_1 - \omega_0$ is the frequency detuning of the laser ω_1 with respect to the optical resonance ω_0 . The total optical loss rate γ_t relates to the optical quality factor via $Q_o = \omega_0/\gamma_t$.

The output transmission T can be extracted from the output field normalized to the input field:

$$T = \left| \frac{a_{\text{out}}}{a_{\text{in}}} \right|^2 = \frac{\Delta^2 + \left(\frac{\gamma_i}{2}\right)^2}{\Delta^2 + \left(\frac{\gamma_t}{2}\right)^2} \quad (2.7)$$

and is plotted in Fig. 2.3(b). In the regime of operation of our devices, we will only consider the unresolved sideband regime where the mechanical frequency is lower than the optical

loss rate ($\omega_m < \gamma_t$). In this regime, the transmission will fluctuate according to the motion of the mechanical resonator dx . The change in transmission dT can then be described as:

$$\frac{dT}{dx}(\Delta) = \left| g_{\text{om}} \frac{dT}{d\Delta} \right|. \quad (2.8)$$

The maximum change in transmission at the optimal detuning ($\Delta = \frac{\gamma_t}{2}$) can be written as:

$$\left. \frac{dT}{d\Delta} \right|_{\text{max}} = \frac{dT}{d\Delta}(\Delta = \frac{\gamma_t}{2}) = (1 - T_o) \frac{Q_o}{\omega_o} \quad (2.9)$$

where $T_o = \gamma_i^2/\gamma_t^2$ is the transmission at optical resonance for double-sided coupling. For single-sided coupling, $T_o = (\gamma_i - \gamma_e)^2/\gamma_t^2$ but with $\gamma_t = \gamma_i + \gamma_e$ [69]. In this chapter, only the dispersive optomechanical coupling g_{om} will be considered. Other types of optomechanical coupling will be discussed in chapters 4 and 5.

2.6 Noise & measurement electronics

Noise plays a central role in measures of sensitivity since it is the main limiting factor that must be overcome. Sources of noise in optomechanics are mainly thermomechanical noise from the mechanical resonator, optical shot noise from the laser, detector noise from the measurement, and backaction noise from light pressure on the mechanical resonator. Below, a classical treatment of noise will be expanded.

The standard formalism to analyze noise uses power spectral density $S(\omega)$ [70, 71]. This term describes the power of a signal (including noise) distributed across a frequency spectrum. In simple terms, the power spectral density (PSD) of a time-series signal $x(t)$ is generally defined as $S_{xx}(\omega) = \int e^{-i\omega t} \langle |x(t)|^2 \rangle dt$, that is the Fourier transform of the autocorrelation of $x(t)$ (see details in appendix C). The form for the spectral density varies depending on the signal to be measured. If it is voltage, then the PSD is written as $S_{VV}(\omega)$. For force and torque, the PSD will be $S_{FF}(\omega)$ and $S_{\tau\tau}(\omega)$, respectively.

Here, we first begin with an analysis of sources of noise and their impact on our measurement before providing a practical method to navigate between PSD's. This formalism suits optomechanics naturally since the thermomechanical signal from the mechanical mode can be displayed comparatively to all the sources of noise. The sensitivity can also be easily extracted as demonstrated in the next section.

Thermomechanical noise

Thermal energy is associated with the Brownian motion of particles associated, giving rise to temperature. Particles collide with the mechanical resonator applying a force proportional to the thermal energy, causing it to vibrate. The thermomechanical noise spectrum of a thermally-excited mechanical mode can be derived from the fluctuation-dissipation theorem [72] and is given by the following force PSD,

$$S_{\text{FF}}^{\text{th}}(\omega) = \frac{4k_{\text{B}}T_{\text{e}}\omega_{\text{m}}m_{\text{eff}}}{Q_{\text{m}}}, \quad (2.10)$$

where k_{B} is Boltzmann's constant, T_{e} is the temperature of the environment (which is set to 300 K for all our experiments). Thermomechanical noise is white (frequency-independent) in the force spectrum. However, the displacement response of the mechanical resonator is enhanced around the resonance of the particular mechanical mode ($\omega = \omega_{\text{m}}$) due to the susceptibility $\chi_{\text{m}}(\omega)$ defined in Eq. (2.2). Therefore, the corresponding displacement PSD $S_{\text{xx}}^{\text{th}}(\omega)$ can be calculated from the force PSD, $S_{\text{FF}}^{\text{th}}(\omega)$, by multiplying by $|\chi_{\text{m}}(\omega)|^2$ such that

$$S_{\text{xx}}^{\text{th}}(\omega) = \frac{4k_{\text{B}}T_{\text{e}}\omega_{\text{m}}}{Q_{\text{m}}} \frac{1}{m_{\text{eff}}[(\omega^2 - \omega_{\text{m}}^2)^2 + (\frac{\omega\omega_{\text{m}}}{Q_{\text{m}}})^2]}. \quad (2.11)$$

Shot noise

Optical shot noise arises from the quantum nature and granularity of light as photons hit the photodetector. Spectrally, it appears as white noise spanning all frequencies with amplitude

proportional to the optical power such that the power spectral density can be written as [50]:

$$S_{\text{PP}}^{\text{sn}} = \frac{2\hbar\omega_l}{\eta_{\text{qe}}} P_{\text{det}} \quad (2.12)$$

where \hbar is Planck's constant, ω_l is the wavelength of the laser, η_{qe} is the quantum efficiency of the photodiode, and P_{det} is the power at the detector. The quantum efficiency is defined as $\eta_{\text{qe}} = R\hbar\omega_l/e$ where R is the responsivity of the photodiode (1 A/W for the Newport 1811 detector used in this report) and e is the charge of the electron [50]. Note that the power PSD, S_{PP} , is optical power not electrical power.

Detector noise

The detector itself produces electronic noise through dark current which is quantified by the noise-equivalent-power (NEP) specified by the manufacturer. For the Newport 1811 detector, the NEP is 2.5 pW/ $\sqrt{\text{Hz}}$ so that the power spectral density is [50]:

$$S_{\text{PP}}^{\text{det}} = \text{NEP}^2. \quad (2.13)$$

Backaction noise

Light carries momentum which exerts radiation pressure on the mechanical resonator. Much like photons arriving at a detector, this shot noise acts as a force pushing on the resonator causing backaction noise. The spectral density can be written as [73]:

$$S_{\text{FF}}^{\text{BA}}(\omega, \Delta) = 2(2\hbar g_{\text{om}})^2 \frac{n_c(\Delta)}{\gamma_t}. \quad (2.14)$$

The number of photons n_c inside the cavity can be calculated as:

$$n_c(\Delta) = \frac{\gamma_e}{2} \frac{1}{\Delta^2 + (\frac{\gamma_t}{2})^2} \frac{P_i}{\hbar\omega_l} \quad (2.15)$$

where P_i is the power at the input of the cavity (ie: at the fiber taper). At the optimized detuning ($\Delta = \frac{\gamma_t}{2}$) and using Eq. (2.15), backaction noise becomes:

$$S_{\text{FF}}^{\text{BA}}(\omega) = \frac{8\hbar g_{\text{om}}^2 Q_o^2 (1 - \sqrt{T_o}) P_i}{\omega_o^2 \omega_l}. \quad (2.16)$$

Power spectral density and conversions

The transduction of the resonator mechanical motion to a photodetected electronic signal, the subsequent analysis of the electronic power spectral density, and the relationship between this power spectral density and the optomechanical coupling coefficients of the device, will be discussed here.

In the setup used in our experiments (see chapter 3), a real-time electronic spectrum analyzer (RSA) samples the time-varying voltage, $V(t) = V_{\text{om}}(t) + V_{\text{n}}(t)$, generated by a photoreceiver input with the optical field received from the optomechanical signal $V_{\text{om}}(t)$ (via a fiber taper in our case). Technical fluctuations, $V_{\text{n}}(t)$, arise from optical and detector measurement noise and will be bundled together as technical noise $S^{\text{n}} = S^{\text{sn}} + S^{\text{det}}$. In general, the fiber taper transmission, T , varies depending on the general displacement x of the nanocavity mechanical resonator and the effect of x on the optical response of the fiber coupled nanocavity. Here, $x(t)$ describes the amplitude of the driven fluctuations of the nanocavity mechanical resonator as well fluctuations caused by optical backaction. The devices fabricated in this thesis are operating in the sideband unresolved regime ($\omega_{\text{m}} \ll \gamma_{\text{t}}$), where the nanocavity field follows the mechanical oscillations (ie. the optical cavity responds instantaneously to the motion of the mechanical resonator). For a given power measured at the detector, P_{det} , and operating wavelength, λ , the optomechanical contribution, $V_{\text{om}}(t)$, to this signal is then given by

$$V_{\text{om}}(t) = \eta_{\text{qe}} g_{\text{ti}} P_{\text{det}} \frac{dT}{dx}(\lambda) x(t) \quad (2.17)$$

where $\eta_{\text{qe}} = R\hbar\omega_1/e$ is the quantum efficiency of the diode, g_{ti} is the photoreceiver transimpedance gain (40,000 V/W assuming a 50 Ω load on the photodetector), and $P_{\text{det}} = \eta P_{\text{i}}$, where η accounts for loss between the detector and fiber taper output P_{i} . A complete derivation of Eq. (2.17) can be found in appendix C. In the RSA, the power spectral density of the optomechanical contribution to the output signal is given by $S_{\text{VV}}(\omega) = |V(\omega)|^2/\text{RBW}$, where $V(\omega)$ is the Fourier-transformed signal of $V(t)$ and RBW is the resolution bandwidth

(explanation in appendix C). Note that the electronic power over a resistance Z would be given by $P_e = V_{\text{om}}^2/Z$. From here on, we will assume all power spectral densities are correctly normalized by the factor $1/\text{RBW}$.

Switching to the frequency domain, the total single-sided power spectral density at the detector is,

$$S_{\text{VV}}(\lambda, \omega) = G^2(\lambda)(S_{\text{xx}}^{\text{th}}(\omega) + S_{\text{xx}}^{\text{BA}}(\lambda, \omega)) + S_{\text{VV}}^{\text{n}}(\lambda, \omega), \quad (2.18)$$

where the optomechanical gain $G(\lambda) = \eta_{\text{qe}} g_{\text{ti}} P_{\text{det}} dT/dx$ describes the detector and optomechanical response [74].

On mechanical resonance, $\omega = \omega_{\text{m}}$, and at optimal wavelength detuning ($\Delta = \frac{\gamma_{\text{t}}}{2}$), which we will call “opt” for “optimal” conditions, the power spectral density becomes:

$$S_{\text{VV}}|_{\text{opt}} = \left(g_{\text{ti}} P_{\text{det}} (1 - T_o) \frac{Q_o}{\omega_o} g_{\text{om}} \right)^2 \left(\frac{4k_{\text{B}} T_e Q_{\text{m}}}{m_{\text{eff}} \omega_{\text{m}}^3} + \frac{8\hbar g_{\text{om}}^2 Q_o^2 (1 - \sqrt{T_o}) P_i}{\omega_o^2 \omega_{\text{t}}} \left(\frac{Q_{\text{m}}}{m_{\text{eff}} \omega_{\text{m}}^2} \right)^2 \right) + S_{\text{VV}}^{\text{n}}. \quad (2.19)$$

Note that $x_{\text{rms}} = \langle x^2 \rangle^{\frac{1}{2}} = \sqrt{k_{\text{B}} T_e / m \omega_{\text{m}}^2}$ is the mean thermal displacement. In our experiments, the mechanical parameters of the device, Q_{m} and ω_{m} , are independent of λ and P_i . These parameters can be extracted by fitting Eq. (2.18) to the measured spectrum for a given λ (usually chosen to maximize $S_{\text{VV}}/S_{\text{VV}}^{\text{n}}$). A method to calibrate the thermomechanical signal of our devices will be presented in chapter 3.

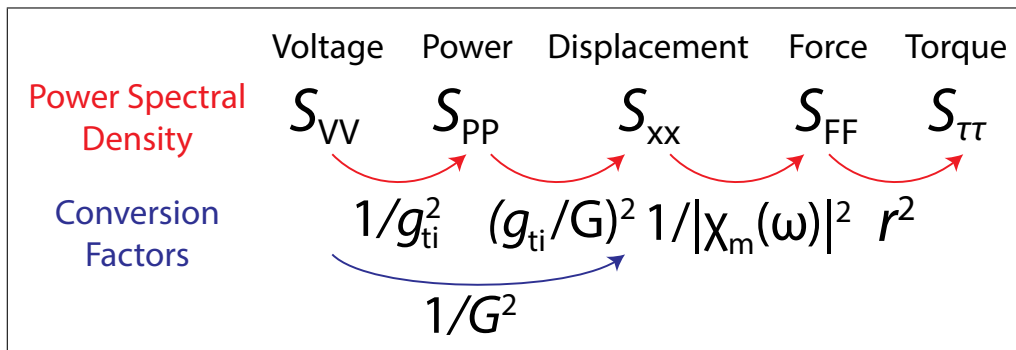


Figure 2.4: Converting between various PSD’s. The conversion factor is the term to multiply to obtain the next PSD.

As observed in eq. (2.18), the power spectral density S_{VV} can be converted to displacement noise S_{xx} by dividing by G^2 . For shot noise and detector noise, S_{PP} can be also be converted to displacement noise by multiplying by g_{ti}^2 . We can then obtain the force resolution using $S_{FF} = S_{xx}/|\chi_m(\omega)|^2$. Finally, the torque resolution is converted via the equation $S_\tau = r^2 S_{FF}$ (via $\tau = r \times F$) as long as the two terms on the right hand side are perpendicular to each other. A summary to help navigate between PSD's can be found in Fig. 2.4.

2.7 Sensitivity

With sources of noise under our belt and the ability to navigate between power spectral densities, an assessment of sensitivity can be performed. To carry forward our analysis, we will write down the displacement and torque PSDs following from Eq. (2.18):

$$S_{xx}(\lambda, \omega) = S_{xx}^{\text{th}}(\omega) + S_{xx}^{\text{BA}}(\lambda, \omega) + S_{VV}^{\text{n}}(\lambda, \omega)/G^2, \quad (2.20)$$

$$S_{\tau\tau}(\lambda, \omega) = r^2(S_{xx}^{\text{th}}(\omega) + S_{xx}^{\text{BA}}(\lambda, \omega)) + r^2 S_{VV}^{\text{n}}(\lambda, \omega)/G^2. \quad (2.21)$$

Next, we can visualize displacement and torque PSDs in Fig. 2.5 using realistic parameters for a typical optomechanical device at room and cryogenic temperatures ($T_e = 300$ K and 4 K, respectively). Here, we assume modest Q_o achievable in most optical cavities, typical Q_m in silicon mechanical resonators, average effective mass m_{eff} , moderate optomechanical coupling g_{om} , common powers of operation P_{det} and P_i , and low fiber-cavity coupling T_o which occurs quite often in our current setup.

The displacement S_{xx} and torque $S_{\tau\tau}$ spectral densities have similar frequency dependence as S_{VV} and S_{FF} , respectively, only scaled by constant factors. In Figs. 2.5(a) and (c), we also define the noise floor as the level of technical noise near resonance. This noise floor is usually used to quote displacement sensitivity [48, 50]. In Figs. 2.5(b) and (d), the minimum total noise at resonance is indicated by the arrows and will be defined further below.

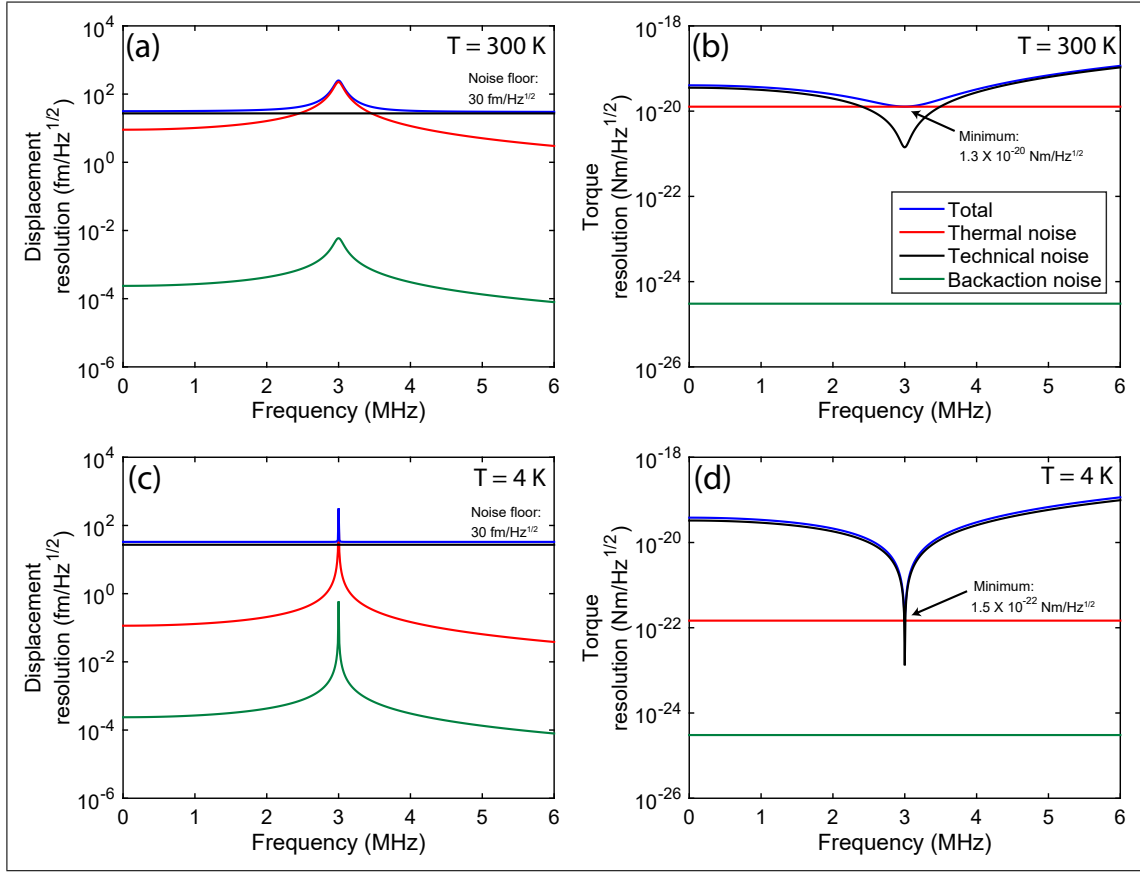


Figure 2.5: Displacement $\sqrt{S_{xx}}$ (a, c) and torque $\sqrt{S_{\tau\tau}}$ (b, d) resolution at room temperature (a, b) and at low temperature of $T_e = 4\text{K}$ (c, d). Parameters used are: $Q_o = 5,000$; $\lambda_o = 1,550\text{ nm}$; $\omega_m/2\pi = 3\text{ MHz}$; $Q_m(T_e = 300\text{K}; 4\text{K}) = (25; 2,500)$; $m_{\text{eff}} = 1\text{ pg}$; $g_{\text{om}}/2\pi = 1\text{ GHz/nm}$; $P_{\text{det}} = 100\text{ }\mu\text{W}$; $P_i = 300\text{ }\mu\text{W}$; $T_o = 0.9$; $r = 3.5\text{ }\mu\text{m}$.

At room temperature, thermal fluctuations noticeably dominate all other noise near the mechanical resonance (Fig. 2.5(a)). The minimum detectable torque shown in Fig. 2.5(b) is predicted to be $1.3 \times 10^{-20}\text{ Nm}/\sqrt{\text{Hz}}$ limited by thermal noise at the signal dip. Assuming a moderate optomechanical response and optical properties of the optical cavity input to determine G , improvements to a thermally-limited torque sensitivity will rely on better engineering of the mechanical properties by maximizing Q_m and reducing m_{eff} . For our devices, backaction noise does not contribute significantly to the total noise since it lays at least 4 orders of magnitude below all other noise sources.

At cryogenic temperatures, we assume the device will also be under vacuum conditions

and thus Q_m would increase by two orders of magnitudes [74]. With every other parameter held constant, the mechanical resonance becomes sharper and the thermal noise decreases such that technical noise is now more prominent and problematic. However, torque sensitivity improves by two orders of magnitudes to 1.5×10^{-22} Nm/ $\sqrt{\text{Hz}}$. At $T_e = 4$ K, backaction noise is still not a limiting factor, at least for modest optical power, optical quality factor, optomechanical coupling, and fiber-cavity coupling. With smaller mass m_{eff} and reaching even lower temperatures of $T_e = 0.25$ mK, a torque sensitivity in the $\times 10^{-24}$ Nm/ $\sqrt{\text{Hz}}$ range is just one order of magnitude above the quantum limit of backaction noise [54].

To continue our analysis, we write out the explicit equation for the PSD's at the "optimal" conditions, ie: at mechanical resonance $\omega = \omega_m$ and optimal detuning $\Delta = \gamma_t/2$. Therefore the displacement and torque PSDs will be:

$$S_{\text{xx}}|_{\text{opt}} = \left(\frac{4k_B T_e Q_m}{m_{\text{eff}} \omega_m^3} + \frac{8\hbar g_{\text{om}}^2 Q_o^2 (1 - \sqrt{T_o}) P_i}{\omega_o^2 \omega_l} \left(\frac{Q_m}{m_{\text{eff}} \omega_m^2} \right)^2 \right) + \frac{S_{\text{VV}}^{\text{n}}}{G^2}, \quad (2.22)$$

$$S_{\tau\tau}|_{\text{opt}} = r^2 \left(\frac{4k_B T_e m_{\text{eff}} \omega_m}{Q_m} + \frac{8\hbar g_{\text{om}}^2 Q_o^2 (1 - \sqrt{T_o}) P_i}{\omega_o^2 \omega_l} \right) + r^2 \frac{S_{\text{VV}}^{\text{n}} m_{\text{eff}}^2 \omega_m^4}{G^2 Q_m^2}. \quad (2.23)$$

To fully convert to torque terminology, the effective mass m_{eff} can be converted to the effective moment of inertia (via $I_{\text{eff}} = m_{\text{eff}} r^2$) such that the torque PSD is:

$$S_{\tau\tau}|_{\text{opt}} = \frac{4k_B T_e I_{\text{eff}} \omega_m}{Q_m} + \frac{8\hbar g_{\text{om}}^2 Q_o^2 (1 - \sqrt{T_o}) P_i}{\omega_o^2 \omega_l} + \frac{S_{\text{VV}}^{\text{n}} I_{\text{eff}}^2 \omega_m^4}{r^2 G^2 Q_m^2}. \quad (2.24)$$

From Eq. (2.22), we can see that the noise floor $S_{\text{VV}}^{\text{n}}/G^2$ can be improved by increasing the optomechanical gain $G = g_{\text{ti}} P_{\text{det}} (1 - T_o) \frac{Q_o}{\omega_o} g_{\text{om}}$. This would amount to improving the optical properties of the cavity (Q_o) as well as the optomechanical coupling g_{om} and the fiber-cavity coupling (related to T_o). The performance of the optical cavity would be paramount in cryogenic conditions. Increasing the optical power P_{det} would also lower the noise floor. However, shot noise is also proportional to the optical power ($S_{\text{VV}}^{\text{sn}} \sim P_{\text{det}}$) therefore would limit the noise floor improvement to just one factor of P_{det} since $G^2 \sim P_{\text{det}}^2$.

Next, we turn toward the torque PSD in Eq. (2.24) and follow a similar analysis to Ref. [75]. We can define the minimum detectable torque to be $\tau_{\min} = \sqrt{S_{\tau\tau}|_{\text{opt}}}$ such that:

$$\tau_{\min} = \sqrt{\frac{4k_{\text{B}}T_{\text{e}}I_{\text{eff}}\omega_{\text{m}}}{Q_{\text{m}}} + \frac{8\hbar g_{\text{om}}^2 Q_{\text{o}}^2 (1 - \sqrt{T_{\text{o}}}) P_{\text{i}}}{\omega_{\text{o}}^2 \omega_{\text{l}}} + \frac{S_{\text{VV}}^{\text{n}} I_{\text{eff}}^2 \omega_{\text{m}}^4}{r^2 G^2 Q_{\text{m}}^2}}. \quad (2.25)$$

This term is the minimum indicated in Figs. 2.5(b) and (d). The lower bound on τ_{\min} is fixed by thermal fluctuations of the mechanical resonator, given by the first term in Eq. (2.25), backaction noise in the second term, and technical noise in the third term. In many cavity optomechanical systems, including the devices studied in this thesis, τ_{\min} is thermally limited at room temperature, where the thermal phonon population exceeds 10^6 for MHz frequency mechanical resonators. In such systems, further reducing the effects of technical noise is advantageous to allow sensitive off-resonance detection, to improve the measurement resolution, and to enhance the ultimate device sensitivity in the case of low- T_{e} operation. Overcoming technical noise, S_{n} , requires not only large optomechanical gain, $G(\lambda)$, as mentioned earlier but also a good quality mechanical resonator (large Q_{m}), small devices (I_{eff}), and driving the system at resonance. Therefore, it is more desirable for a device to be only thermally-limited as only the mechanical properties of the device needs to be addressed. Moreover, technical noise scales with $I_{\text{eff}}^2/Q_{\text{m}}^2$ compared to $I_{\text{eff}}/Q_{\text{m}}$ for thermal noise. Consequently, from a mechanical resonator point of view, technical noise has a lower incident of becoming a limiting factor compared to thermal noise.

For magnetometry purposes, the magnetic sensitivity is often quoted as the minimum magnetic moment μ_{\min} with units of Bohr magneton μ_{B} (magnetic field of a single electron spin). Using $\boldsymbol{\tau} = \mathbf{m} \times \mu_0 \mathbf{H}$, the minimum magnetic moment can be calculated as

$$\mu_{\min} = \frac{\tau_{\min}}{\mu_0 H} \quad (2.26)$$

where μ_0 is the magnetic permeability. At room temperature and given an achievable applied field of $H = 35$ A/m, the minimum magnetic moment is estimated to be $\mu_{\min} \sim 3 \times 10^7 \mu_{\text{B}}$.

2.8 Torque actuation

Beyond sensitivity, an estimation of the applied torque can help us determine if the signal can rise above the noise (ie: the signal-to-noise ratio). In magnetometry, the applied torque τ_{ap} due to the magnetic excitation \mathbf{M} of a volume of magnetic material V_{mgn} under applied field \mathbf{H} can be expanded from Eq. (2.1) and calculated as [16]:

$$\tau_{\text{ap}} = \mathbf{M}V_{\text{mgn}} \times \mu_0\mathbf{H}. \quad (2.27)$$

Assuming a volume of magnetic material around $1 \mu\text{m}$ by $1 \mu\text{m}$ by 40 nm (similar to the devices studied in chapter 6) with magnetization saturated at $\mathbf{M} = 740 \text{ kA/m}$ and a driving field of $\mathbf{H} = 35 \text{ A/m}$ at the mechanical resonance, the applied torque is estimated to be $\tau_{\text{ap}} = 1.3 \times 10^{-18} \text{ Nm}/\sqrt{\text{Hz}}$ using the realistic system discussed above. The signal is two orders of magnitude above noise leading to a signal-to-noise ratio of about 20 dB. The driven torque can be plotted as a delta function above the noise, shown in Fig. 2.6.

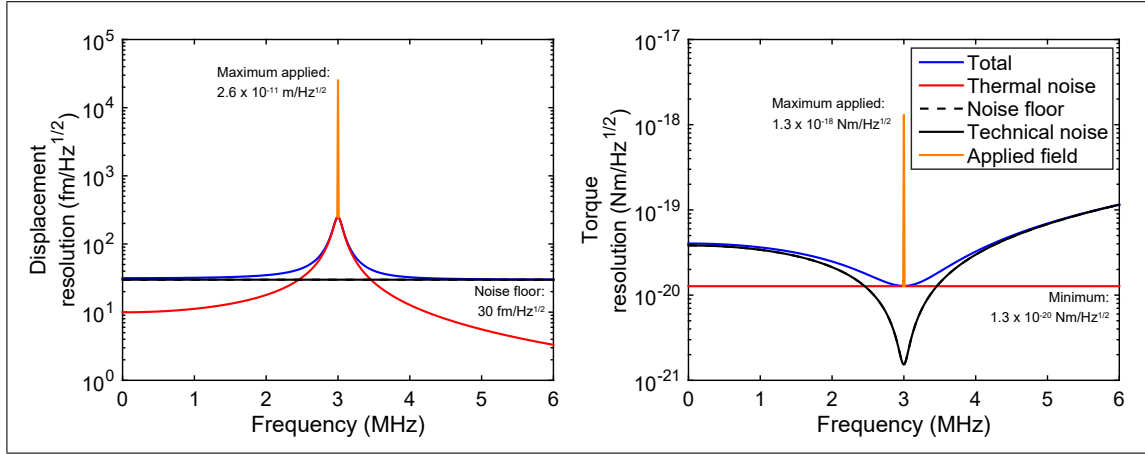


Figure 2.6: (a) Displacement and (b) torque resolution including a driving torque signal ($\omega = \omega_m$) in orange. The parameters used for the signal are $V_{\text{mgn}} = 1 \mu\text{m} \times 1 \mu\text{m} \times 40 \text{ nm}$, $\mathbf{M} = 740 \text{ kA/m}$ and $\mathbf{H} = 35 \text{ A/m}$.

2.9 Challenges of higher frequency operation

A number of magnetic phenomena occur at fast time scales with high-frequency applications requiring RF rates in the hundreds of MHz and even GHz range [76–79]. Higher frequency of operation can pose a challenge for future device design (unexplored in this work). To quantify the problem, a useful metric is the proportion of noise between thermal and technical noises. As discussed above, a thermally-limited device is more desirable and generally leads to better torque sensitivity. Therefore $S_{\text{FF}}^{\text{th}}$ should be greater than S_{FF}^{n} . We define ϕ as the ratio of $S_{\text{FF}}^{\text{th}}/S_{\text{FF}}^{\text{n}}$ such that

$$\phi = S_{\text{FF}}^{\text{th}}/S_{\text{FF}}^{\text{n}} = \frac{4k_{\text{B}}TQ_{\text{m}}G^2}{S_{\text{VV}}^{\text{n}}m_{\text{eff}}\omega_{\text{m}}^3}. \quad (2.28)$$

The aim is for $\phi > 1$ such that the device sensitivity is thermally-limited.

From Eq. (2.28), we observe that technical noise grows with ω_{m}^3 over thermal noise. Thus, at higher frequencies, the imperative to improve optical and mechanical properties of the device becomes considerable.

The importance of these properties at high frequencies can be visualized over a parameter space illustrated in Fig. 2.7. Plotted on the left column is the ratio ϕ . Red regions corresponds to thermally-limited noise ($\phi > 1$) while blue regions corresponds to technically-limited noise ($\phi < 1$). The right column shows respectively the torque sensitivity. Evidently, at higher frequencies, technical noise becomes more dominant and torque sensitivity suffers concurrently. The prescription is simple albeit not always an easy task: improve Q_{m} (or decrease m_{eff}) and increase G . For example, for a device operating near 100 MHz to possess the same level of torque sensitivity as a device at 3 MHz, the mechanical quality factor Q_{m} must be enhanced by more than two orders of magnitude. Q_{m} does generally increase slightly at higher frequencies due to the decreasing displacement and subsequent air drag of small mechanical resonators. Increasing G does not affect torque sensitivity at low frequencies but

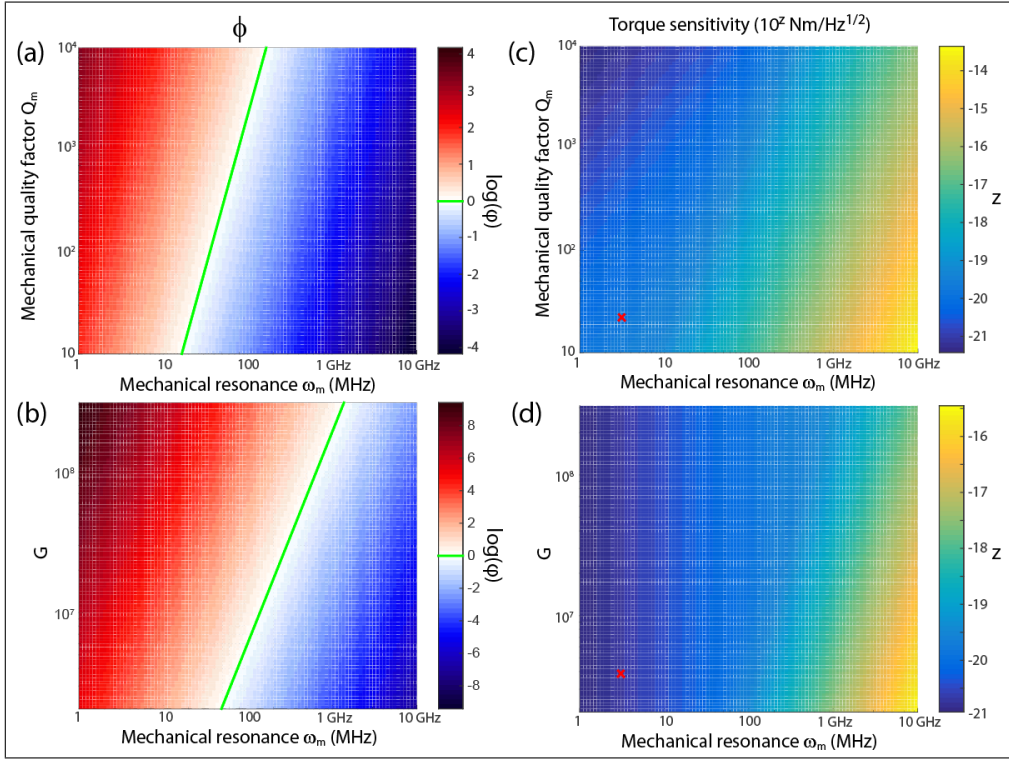


Figure 2.7: (a) Ratio $\log(\phi)$ with varying mechanical quality factor Q_m and frequency ω_m . (b) Ratio $\log(\phi)$ with varying optomechanical response G and ω_m . The red color corresponds to thermally-limited regime while the blue color indicates region where technical noise is dominant. The green line delimits the two such that $S_{FF}^{\text{th}} = S_{FF}^{\text{n}}$. (c) and (d) Same for torque sensitivity. The darker blue correspond to better torque sensitivity while the yellow parts mark regions of worse sensitivity. The red mark points to our device described in chapter 3 with low frequency ($\omega_m = 3$ MHz).

might marginally enhance it at higher frequencies.

These stringent requirements pose a challenge for torsional optomechanical devices at higher frequencies. One that will require creative design and engineering.

2.10 Summary

In this chapter, a practical overview of optomechanical torque sensitivity has been presented. Using the theoretical tools demonstrated here, the sensitivity of optomechanical torque sensors can be comparatively studied. Not only that, the methodology laid out here can inform

the design of devices according to the target application and imposed constraints.

The rest of this thesis will focus on the implementation of optomechanics for torque magnetometry. However, the work here can also be directed toward other applications such as sensing light with orbital angular momentum [80–82] and many other interesting rotational phenomena.

Chapter 3

Split-beam cavities: design, fabrication, characterization

In this chapter, details of the design, fabrication, and basic characterization of split-beam cavities will be expounded. We will start with a brief historical development of our optomechanical device which follows our first steps to build a chip-based nanoscale torque sensor. We will then delve into the design philosophy of split-beam cavities which was developed in large part by Dr. Hryciw. Next the fabrication process and the measurement setup will be discussed. At the end of the chapter, the characterization of the optical and mechanical properties our devices will be demonstrated.

3.1 Nanobeam photonic crystal cavity

From Eq. (2.25), at room temperature and ignoring radiation pressure in the second term, the knobs for torque sensitivity are: effective mass m_{eff} (via I_{eff}), the optical quality factor Q_o , and the optomechanical coupling g_{om} (the latter two via the optomechanical gain G). The mechanical frequency ω_m and quality factor Q_m are related to the frequency of operation and dissipation which is dependent largely on the material and the environment, though improvements can be made with extensive anchor geometry optimization and phononic shielding [83–86]. Generally, targeting a low τ_{min} will require a low-mass high- Q_o optomechanical cavity that effectively allows efficient transduction between mechanical and optical modes.

A photonic crystal cavity (PCC) is a prime candidate to fulfill these specifications. PCC's take advantage of bandgap engineering by fashioning the material geometry to confine light within wavelength-scale volumes [87]. The periodicity of a photonic crystal structure creates

a photonic band structure where certain photon energies are forbidden inside bandgaps akin to electrons in a semiconductor [88]. An optical cavity can then be built by creating a defect within the periodicity. Optomechanical devices based on PCC architecture ensure that the optical field can interact and strongly overlap with the mechanical resonances [26–28, 89]. Nanobeam versions of PCC also have the added benefit of small mass and potential coupling to large-scale displacement [31, 50, 90, 91].

Nanobeam PCC’s is a section of an optical waveguide in which a series of holes act as Bragg gratings. The waveguide confines light laterally via total internal reflection while the gratings limit light propagation within the waveguide at wavelengths that fall into the bandgap of the grating. A defect in the Bragg gratings create a localized volume in which an optical mode can be confined. The defect can assume various geometries depending on the type of cavity [92, 93].

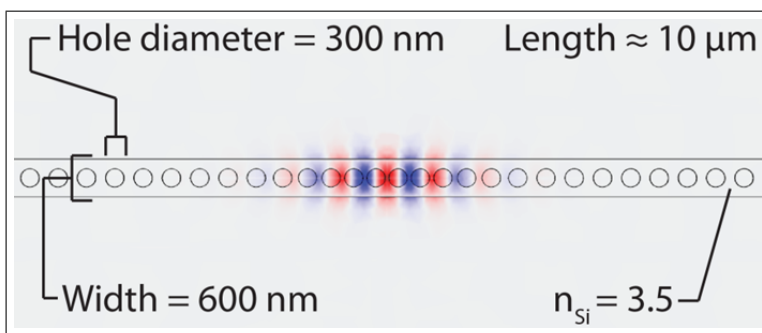


Figure 3.1: A typical silicon (with refractive index n_{Si}) nanobeam photonic crystal cavity with device dimensions tailored for telecommunication wavelengths. Here, the cavity is formed by reducing the periodicity of the inner air holes. A numerical simulation of the optical mode is overlaid on top.

Fig. 3.1 shows the top view of the design of a nanobeam PCC in silicon with dimensions set for wavelengths near $\lambda_o \sim 1,550$ nm. The Bragg gratings on the outer holes form a set of mirrors while the inner holes create an optical cavity supporting an optical mode. In the example shown here, the cavity is formed by reducing the lattice constant of the grating towards the centre of the nanobeam. The majority of the optical mode lives in the dielectric

ribs of the nanobeam with the defect formed by a decrease in dielectric material per unit volume, therefore it is called a “dielectric mode”. Conversely, if the defect is created by increasing the dielectric material (ie. less volume occupied by air holes), then it is called an “air mode”. Typical Q_o can reach 10^7 in theory and range from $10^5 - 10^6$ in practice [92,93].

Preliminary optomechanical design

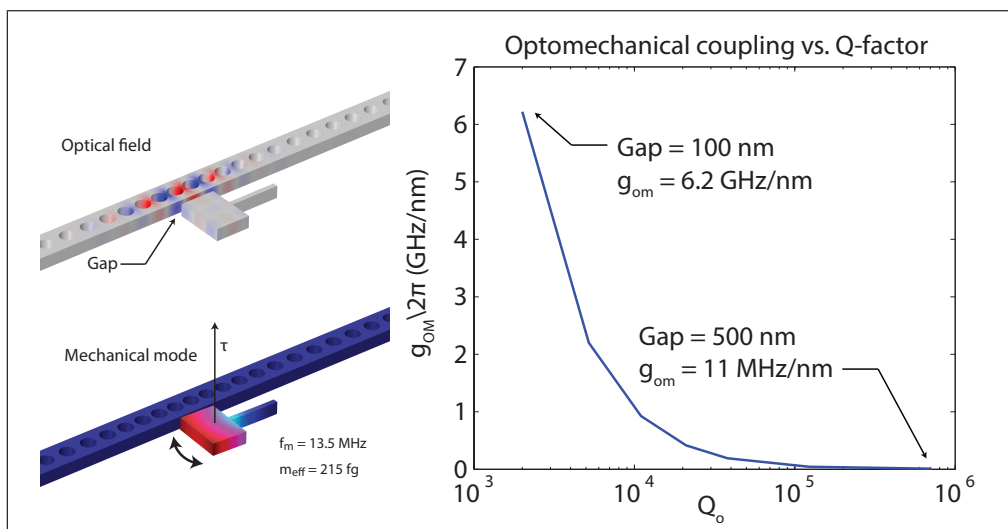


Figure 3.2: Left: a small torsional paddle in the near field of an optical mode supported inside a photonic crystal nanobeam cavity. Right: g_{om} vs Q_o which is proportional to the gap distance.

In order to create an optomechanical device, a mechanism to modulate the resonance wavelength is required. Starting with the nanobeam PCC, one could straightforwardly bring a little piece of dielectric in the near field of the cavity. The vibration of this paddle, potentially coupled to a source of torque as illustrated on the left in Fig. 3.2, would shift the resonance wavelength.

Our numerical simulations using COMSOL can estimate g_{om} for the geometrically perfect device modeled in Fig. 3.2 (see appendix B). The graph on the right shows g_{om} in relation to the Q_o of this first iteration of an optomechanical device. The critical parameter in this particular device is the gap distance between the nanobeam and the paddle. The closer the

paddle to the optical cavity, the more Q_o would suffer as indicated by the curve. Concurrently, g_{om} increases with smaller gap, reaching close to 6 GHz/nm at 100 nm. However, the theoretical value for Q_o , here limited by radiation loss, is as low as 2,000 which in fabricated devices could be at least an order of magnitude less. There is therefore a trade-off between g_{om} and Q_o in this geometry. Coincidentally, we observed that the presence of the paddle was able to induce g_{om} . This relation will be further explored in subsequent chapters.

Beyond the g_{om} vs Q_o trade-off, there might be another drawback. The potential location of the deposited magnetic material will be in the near field of the optical mode which will degrade Q_o further due to absorption. This can be countered by making the paddle larger at the expense of increasing the effective mass m_{eff} . A novel design that incorporates the mechanical element into the nanobeam PCC might help alleviate this trade-off.

3.2 Design philosophy for split-beam cavities

Optomechanical devices whereby mechanical resonances seamlessly arise from the optical cavity offer large optomechanical transduction. Such designs capitalize on the material deformation at the maximum of the optical field in order to generate optomechanical coupling. An example is the natural breathing mode from the lateral expansion in the center of a nanobeam PCC or the radial expansion of a microdisk cavity [62, 94, 95].

However, as discussed in chapter 2, rotational motion does not lend itself well to a strong optomechanical response due to unfavorable symmetries and the requirement of large scale displacement such as in Ref. [50]. The challenge is to design a moving platform with large g_{om} without adding too much mass.

Our proposed design uses the nanobeam PCC itself and “splits” it into two separate elements by a gap as illustrated in Fig. 3.3(a). This photonic crystal “split-beam” cavity (SBC) is essentially two cantilever nanomechanical resonators (similar to Ref. [43]) which are patterned to also serve as optical mirrors. The mirrors (or half-nanobeams) can move inde-

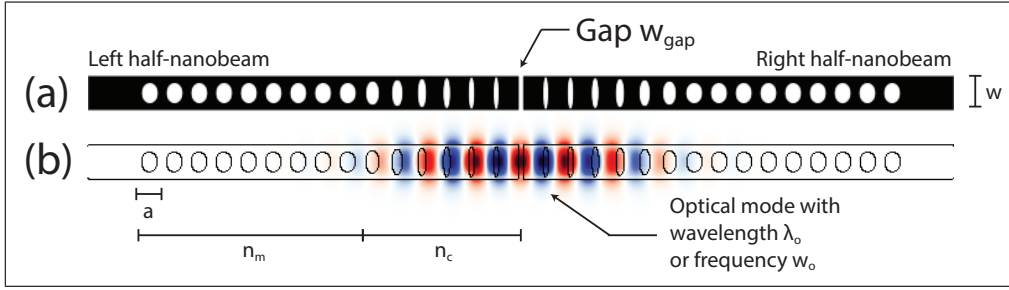


Figure 3.3: (a) Schematic of the SBC design with gap distance w_{gap} and nanobeam width w . (b) Numerical simulation of SBC with optical mode overlaid. The optical mode is confined between the two half-nanobeams with a cavity created by n_m mirror holes and n_c cavity holes on each side. The periodicity a is the distance between the holes. With permission from Aaron Hryciw.

pendently and support mechanical resonances whose properties can be customized through design of their mechanical supporting structure.

With careful design, the SBC device can still support a high- Q_o optical mode localized between the two mirrors (see Fig. 3.3(b)). This is achieved by the mirror pattern which consists of a periodic array of holes with dimensions tapered from circles to elliptical shapes with a profile similar to the gap [96]. Crucially, the band edge of the photonic crystal air mode associated with the gap unit cell is phase-matched with the band-edge of the neighboring elliptical hole unit cell air mode, minimizing radiation loss in the gap region, and creating a smooth “optical potential” for localized modes [59,92,96]. The air mode also allows the peak of the optical mode residing in the gap to overlap strongly with movement of one or both mirrors enabling for potentially large g_{om} . By splitting the nanobeam into two, the design supports mechanical resonances with effective masses $m_{\text{eff}} < 1$ pg (see section 3.5 below).

More details on the design of SBC devices can be found in Ref. [96]. Here, a summary of practical steps to build a SBC device will be presented.

1. Pick target optical frequency w_o .
2. Pick nanobeam thickness t .

3. Choose periodicity a .
4. Set the nanobeam width w .
5. Find central hole dimension such that the band-edge is at the target frequency.
6. Find mirror hole dimensions that maximize mirror strength γ to form the cavity .
7. Pick the number of cavity holes n_c .
8. Taper the cavity hole dimensions quadratically from the central hole to the mirror.
9. Pick the number of outer mirror holes n_m .
10. Replace central hole with a gap w_{gap} then optimize for Q_o .

Each step will be described further below:

1. The target frequency is the frequency of operation for the application of choice. We chose the well-known telecommunication band near wavelength $\lambda_o \approx 1,550$ nm or resonance frequency $w_o/2\pi = 193$ THz for our cavity.
2. The target thickness t of the nanobeam should be determined such that the optical mode in the cavity remains single mode. This requires features in fabricated devices to be close to half the effective wavelength ($\lambda_{\text{eff}} = \lambda_o/n$). In silicon, the refractive index $n_{\text{Si}} = 3.5$. Justifiably, the thickness of our commercially-bought silicon-on-insulator (SOI) wafers is $t = 220$ nm.

3. The periodicity a of the holes should approximately match the effective wavelength. With the refractive index of silicon, $a \sim 400$ nm.

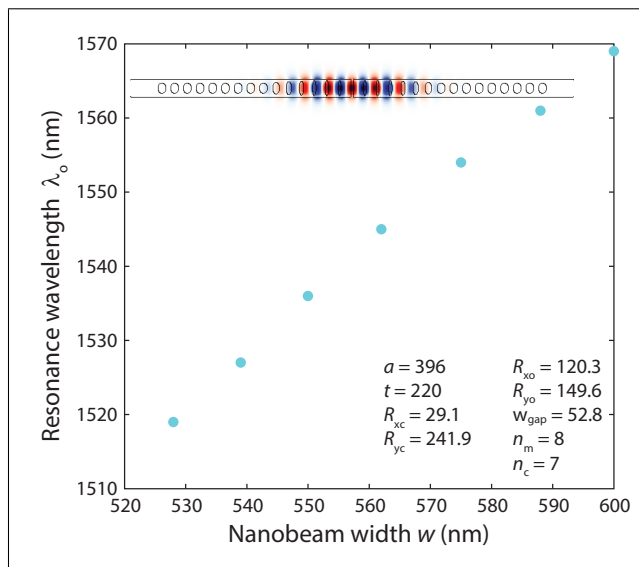


Figure 3.4: Numerical simulation of the resonance wavelength λ_0 of a split-beam cavity (top of graph) with various widths w . All quoted dimensions are in nanometers except for the number of mirror holes n_m and number of cavity holes n_c . With permission from Aaron Hryciw.

4. The nanobeam width w should be set such that it is not too large to allow multi-modes but not too small such that Q_0 degrades due to diffraction or the device becomes difficult to fabricate due to proximity effects during the lithography step. We set $w \sim 600$ nm. The width w will also dictate λ_0 as shown in Fig. 3.4 and therefore can be used as a parameter to tune the cavity.

5. The dimension of the gap w_{gap} is determined from band-edge frequency of the central hole which it seeks to replace in order to create the split. Band structure analysis is performed using numerical simulations of a periodic waveguide. Three possibilities for central holes near the frequency of operation are shown in Fig. 3.5. The band-edge frequencies of the

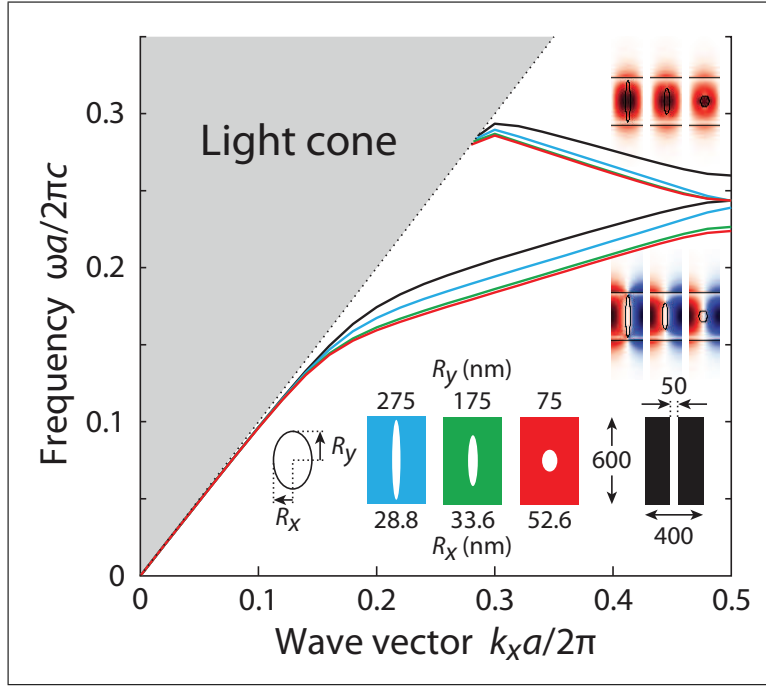


Figure 3.5: Dispersion diagram for SBC design with three candidate hole dimensions matching with the gap (black). With permission from Aaron Hryciw [96].

gap must match with that of the central holes. Counterintuitively, the dielectric mode of the gap (lower black branch) must match with the air mode of the hole (upper branch) [96]. Although all three designs for the central hole are viable, higher Q_o can be achieved when the shape of the hole correlates with the gap. Therefore, the elliptical hole (in blue) has the greatest potential to form a high- Q_o optical cavity. However, this comes at the expense of decreased fabricability as one dimension (here the semi-minor axis R_x of the ellipse) becomes increasingly difficult to define lithographically. In this design, we chose a gap of $w_{\text{gap}} = 50$ nm which matches with an elliptical hole in the center.

6. Once the central hole is determined, the dimensions of the outer mirror holes comes next. The outer mirrors serve as reflectors and thus should possess large reflection. This is

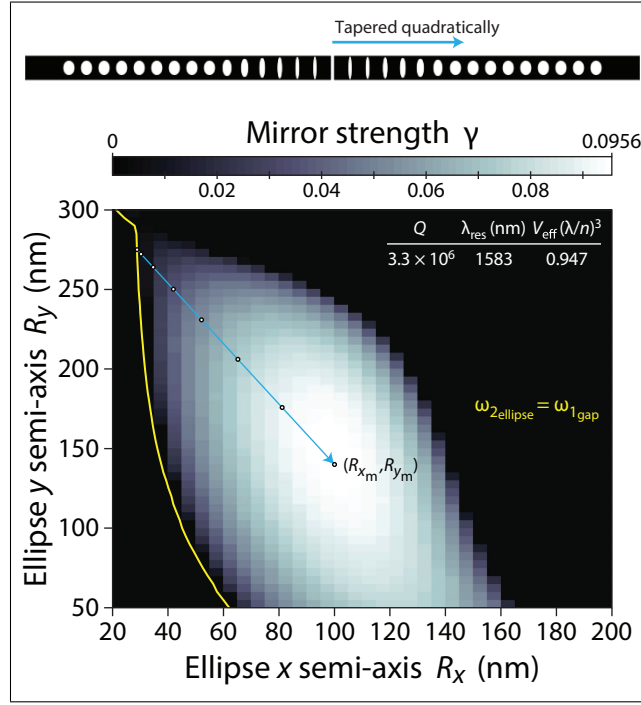


Figure 3.6: Mirror strength γ as a function of ellipse dimensions R_x and R_y . The yellow line represents the band-edge frequency matching between the central elliptical hole and gap dimensions. The blue line is the path taken to quadratically taper the ellipse dimension from the center toward the outer holes for the cavity holes. With permission from Aaron Hryciw, modified from Ref. [96].

quantified by the mirror strength γ given by [93]:

$$\gamma^2 = \left(\frac{\omega_2 - \omega_1}{\omega_2 + \omega_1} \right)^2 - \left(\frac{\omega_{\text{res}} - \omega_0}{\omega_0} \right)^2, \quad (3.1)$$

where ω_1 and ω_2 are the lower and upper band-edge frequencies, respectively, ω_0 is the midgap frequency, and ω_{res} is the target cavity resonance frequency. The mirror strength γ is strongest when the band gap is large ($\omega_2 - \omega_1$) and the central frequency matches the target resonance frequency ($\omega_{\text{res}} - \omega_0$).

The mirror strength is plotted in Fig. 3.6 as a function of ellipse dimensions R_x and R_y . The central elliptical hole is represented by the yellow line and lies in a region of low mirror strength. The dimensions of the mirror holes are given by $R_{x,m}$ and $R_{y,m}$ where γ is the strongest (whitest region).

7. The cavity holes are located between the central elliptical hole and the mirror holes. Their dimensions must be gradually tapered between the elliptical shape in the center to the rounder shape for the mirror holes. A low number of cavity holes n_c will result in poor optical properties such as confinement and Q_o . A large number of cavity holes will lead to poor confinement of the optical mode. Here we pick the number of cavity holes to be $n_c = 6$.

8. The dimensions of the cavity holes are tapered from the central ellipse to the mirror holes as pointed by the blue arrow in Fig. 3.6. Mirror hole dimensions (circles on the blue line) are found by tracing a path from the yellow curve to the maximum mirror strength γ while following a quadratic equation. This creates a quadratically-shaped optical potential in which the optical field is trapped.

9. We select the number of mirror holes n_m based on mirror strength and practical dimensions. More mirror holes will result in less optical field leakage. However, it will add to the nanobeam length. Here we choose $n_m = 9$ with maximum strength to maintain small nanobeam cavity footprint.

10. Finally, we introduce the gap w_{gap} to replace the central elliptical hole. Then using the full structure in numerical simulations using Finite Difference Time Domain (FDTD) methods, the total Q_o is optimized by small correction in dimensions. In the particular design shown in Fig. 3.6, the SBC device supports an optical mode with $Q_o \sim 10^6$ at resonance wavelength at 1,583 nm, and mode volume slightly less than a wavelength.

3.3 Nanofabrication of split-beam cavities

The fabrication of all our devices was performed at two main cleanrooms in Edmonton: the UofA nanofabrication facility located in the ECERF building in the department of electrical and computer engineering, and the NINT nanofabrication facility.

Process development

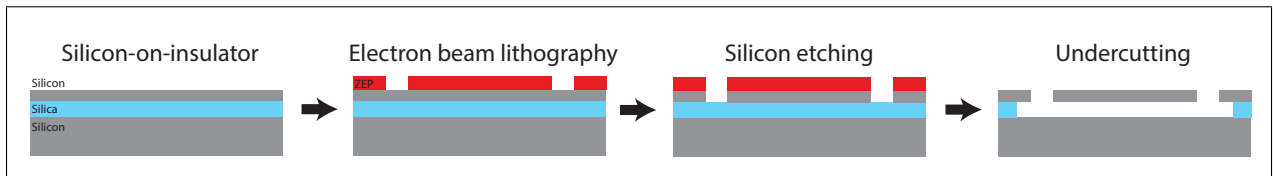


Figure 3.7: First cycle of fabrication to define SBC devices on SOI chips.

The SBC devices studied in this thesis were fabricated from 1 cm² silicon-on-insulator (SOI) chips. They were diced from a 6-inch diameter wafer made by Soitec with a 3- μ m-thick silicon dioxide (SiO₂ or silica) layer and a 220-nm-thick silicon (Si) top layer. The purpose of this first cycle of fabrication is to define the pattern of our devices on the silicon chip. A standard semiconductor fabrication process for silicon is followed and is summarized in Fig. 3.7 and the list below.

1. Cleaning: Piranha
2. Resist coating (ZEP 520A)
3. Electron beam lithography for first (Si) layer
4. Cold development
5. Silicon etching: transfer of pattern into the Si layer
6. Cleaning: heated Remover-PG

7. Undercutting: SiO₂ etching using HF to release devices

The first step is a standard cleaning procedure called “piranha” which uses sulfuric acid and hydrogen peroxide in a reaction to clean all organic compounds on the chip. A 300–400 nm-thick positive tone resist (ZEP 520A) was spun on the chip and then heated to set. Electron beam lithography was used to write the device pattern on the resist. This was immediately followed by a cold development process to carefully remove the exposed resist. To transfer the pattern from resist to the Si device layer, a reactive ion etching step using fluorine chemistry was executed. Performance at this stage was evaluated by the straightness of the sidewalls of the silicon ridge and the clearance of small features such as the ellipses and the 60 nm gap. Finally, after a cleaning of leftover resist using heated Remover-PG, a wet chemistry undercut process using hydrofluoric acid (HF) etched the exposed silica and released the Si devices.

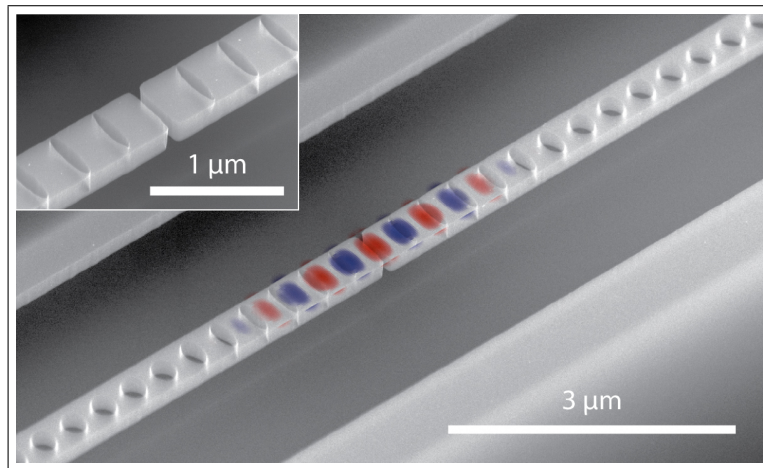


Figure 3.8: SEM images of fabricated SBC devices with elliptical holes. Optical mode is overlaid. Inset: close view of the gap between the two mirrors.

Details on the function, operation, and procedure of each tool or process can be found in appendix D. A second cycle of fabrication will be required to add magnetometry functionality and is presented in chapter 6.

Stiction

Fabricating freestanding mechanical resonators comes with some practical challenges. One of them is stiction which causes long suspended pieces to droop and stick to the substrate below during the undercutting step. This is a well-known problem especially in MEMS and is caused by the competitive forces of adhesion between two solid surfaces and the elastic restoring strain of a deformed structure [97, 98].

A Peel number N_p was devised to quantify the ratio between those two forces. If $N_p > 1$, the structure will not stick to the substrate. If $N_p < 1$, the structure will stick to the substrate. The equation to calculate Peel number depends on the shape of the structure and the stiction configuration. In the simplest case and for comparison with our SBC devices, let's take a cantilever beam of thickness t and length L that is a distance h from the substrate. For the configuration, we assume that the tip of the cantilever touching the substrate constitutes stiction. The equation for the Peel number N_p is then given by [99]:

$$N_p = \frac{3Et^3h^2}{8L^4W_a}, \quad (3.2)$$

where E is the Young modulus (170 GPa for silicon) and $W_a = \gamma_1 + \gamma_2 + \gamma_{12}$ is the Dupré adhesion between the cantilever and the substrate. γ_1 and γ_2 are the surface energies of the cantilever and the substrate, respectively. In our case, they are both made of silicon therefore $\gamma_1 = \gamma_2 = 2.4 \text{ J/m}^2$ [100]. γ_{12} is the interface energy between two materials (0.4 J/m² for silicon [101]). These numbers are experimental approximations.

By plotting the Peel number against the length L of the cantilever (Fig. 3.9), one can quickly estimate the length at which the cantilever will start sticking to the substrate. In our case, that length falls around 6 μm . In consequence, extra tethers are required to support our half-nanobeam since they can be as long as 7.5 μm . The stiction limit also correlates with our experience of devices supported by long and thin tethers of between than 5–10 μm in length. During undercutting of our devices, the liquid used (mostly water and HF) increases stiction due to extra capillary forces. This can be mitigated by using critical point

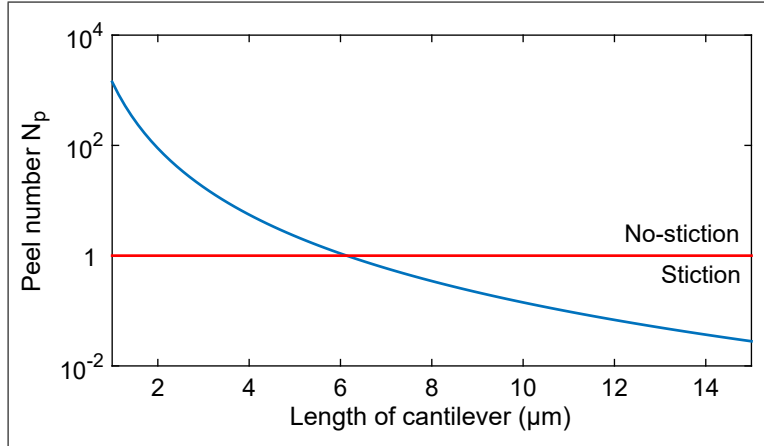


Figure 3.9: Peel number of a silicon cantilever of thickness t and length L suspended at height h above a silicon substrate.

drying. A potential alternative material will be to fabricate silicon nitride devices which has higher tensile strength and, when deposited under stress, can produce higher Q_m mechanical resonators [102]. In chapter 6, we will describe how stiction was reduced in our second fabrication cycle by using a lift-off technique to deposit magnetic material on top of our devices.

3.4 Fiber taper measurement setup

Following fabrication, the optical and mechanical performance of the device was characterized. Since our devices are distinct and not integrated within a larger system or network, a fiber taper measurement setup is used to optically access individual nanocavities (see Fig. 3.10). This allows for rapid prototyping by testing each device then moving on to the next with ease.

A fiber taper is an optical fiber for which the waist diameter on a small section is reduced down to a size between a wavelength to half a wavelength of light (around $1.5 \mu\text{m}$ for telecommunication range). This allows the transmitted light to evanescently couple light to another optical channel in the near-field. A dimple (or a small depression) in the taper is

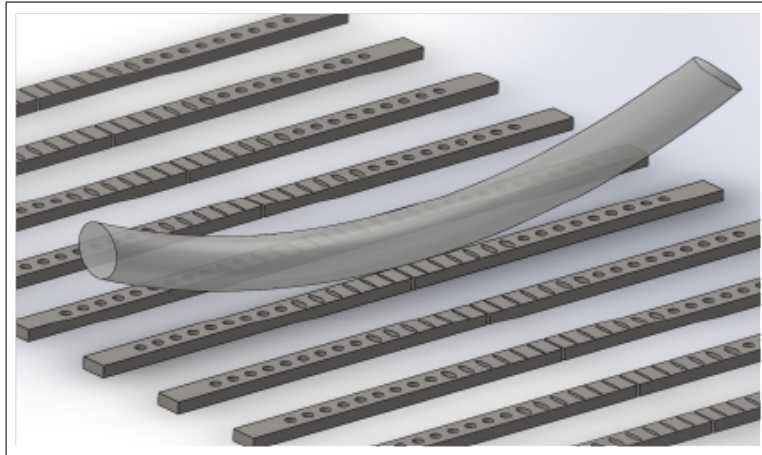


Figure 3.10: Fiber taper with a dimple probing individual devices within an array. Image courtesy of Chris Healey.

added to allow contact of the fiber with only one device at a time [103]. This technique has been developed by the Painter group at Caltech since 2003 and is now widespread among many research groups [104]. The fiber taper was central in the Ph.D. work of my supervisor where he demonstrated efficient evanescent coupling to photonic crystal waveguides [105,106] and cavities [107]. Experiments with nanoscale optical devices were made accessible with use of the fiber taper by leaving the rest of the chip unimpeded for other functions. An example is the demonstration of laser cooling and trapping of atoms with silicon nitride microdisks [108]. The fiber itself can be a tool to manipulate nanoscale objects such as a diamond crystal deposited on top of a silica microdisk for experiments in cavity QED [109].

Fabrication of dimpled fiber taper

The fabrication of fiber taper with dimple was done in our laboratory at the UofC in the Institute for Quantum Science and Technology (IQST) and the Department of Physics & Astronomy. The original material comes from a spool of fiber for telecommunication wavelengths (near 1,550 nm) with cladding of 125 μm and a buffer of 250 μm . The buffer is stripped to expose the cladding over a couple of centimeters. After a quick IPA cleaning, the

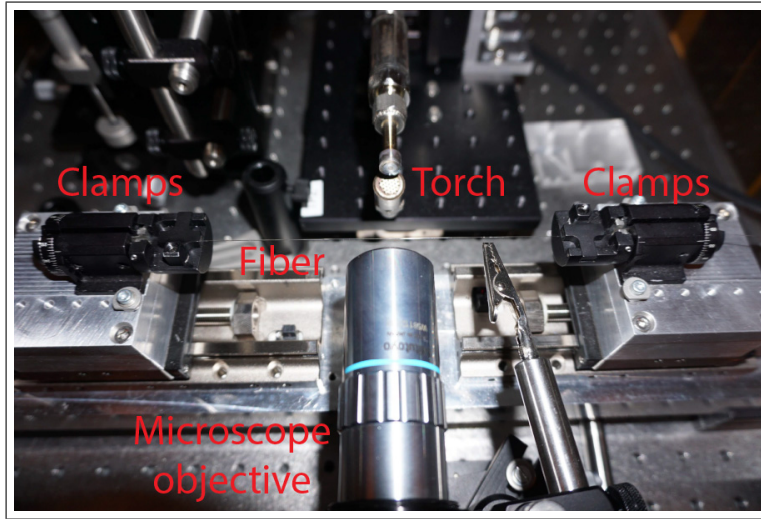


Figure 3.11: Fiber pulling station consisting of a horizontally positioned fiber clamped on both ends. A flame from a nearby torch melts the fiber while the fiber diameter is monitored via the microscope objective.

fiber is then securely positioned between two motorized clamps. The transmission through the fiber can be monitored at this point by connecting one end of the spool of fiber to a laser and the other (shorter) end to a photodetector. The fiber tapering operation starts when a torch flame fueled by hydrogen slowly advances toward the center of the exposed cladding. Immediately after the flame touches the flame and is in position, both clamps are programmed to move away from each other. This stretches the fiber as the central region becomes thinner via heating from the flame. The output optical signal oscillates rapidly in time when the optical mode inside the fiber becomes multimode. Oscillations cease once single-mode operation is reached. The fiber pulling is stopped while the torch retreats. At this point the central region of the fiber has been tapered down to less than $1.5 \mu\text{m}$ in diameter but gained some length.

In order to facilitate testing of individual devices among a large array, a dimple was added to the fiber by modifying the process in Ref. [103]. To add a dimple to the otherwise straight fiber taper, an external force must act on a local region of the fiber. There are various methods to do this including another fiber or a ceramic blade (made in-house by Mr.

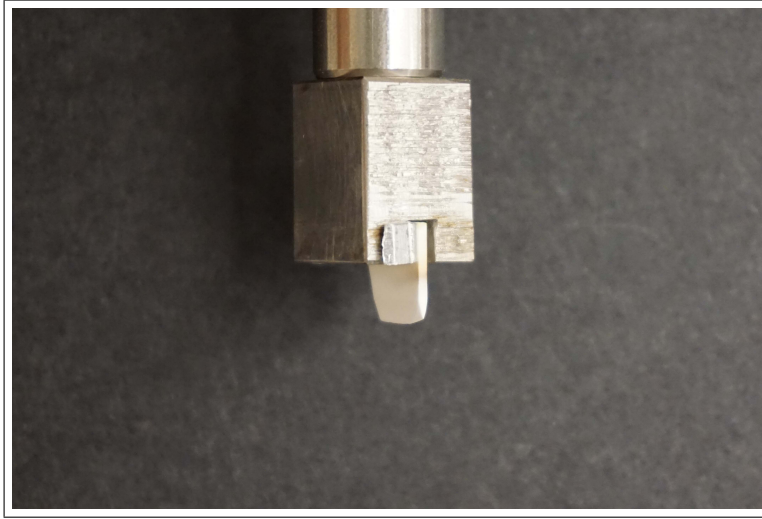


Figure 3.12: Photo of the ceramic blade used to imprint a dimple on the fiber taper.

Healey with the help of the science workshop). The latter is more stable and is easier to get the fiber taper unstuck after contact. As implied, the sharp edge of a ceramic blade is forced down on the thinnest spot on the fiber taper where the dimple will be. As the blade is lowered, the fiber is de-tensioned using the clamps. This creates a V-shape feature into the fiber taper. The torch flame is then brought rapidly into the fiber taper to reconfigure it and mold the shape. Then the blade is slowly removed to reveal a dimple in the fiber taper as shown in Fig. 3.13.

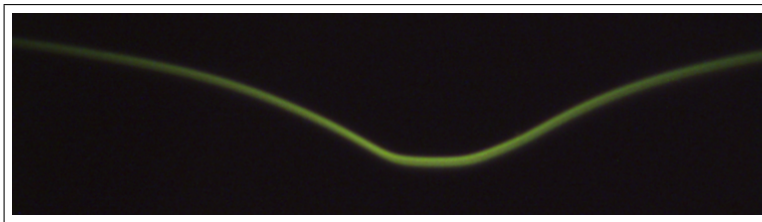


Figure 3.13: A $1\mu\text{m}$ -diameter fiber taper with a dimple viewed under the optical microscope. The nominal radius of curvature is about $25\mu\text{m}$.

The following operation is the shortest but hardest: removing the fiber from the clamp while attaching it to the fiber mount. This step has the highest potential for the fiber to

break. First, the fiber mount is positioned in place close to the fiber taper. Carefully, the fiber is secured on the mount using tape or epoxy glue with UV curing. Then the clamps are slowly opened to free the fiber. Depending on the type of mount (one design is shown in 3.14), an additional step to turn the mount around to form a U-shape with the fiber taper is required. Moreover, the tilt of the dimple must be considered. This will add an extra step to rotate the fiber via the clamps until it is pointing in the correct direction (down when mounted on the measurement setup). The original procedure consisted of removing the fiber taper with our own shaky hands which greatly reduced the yield of fiber taper production.

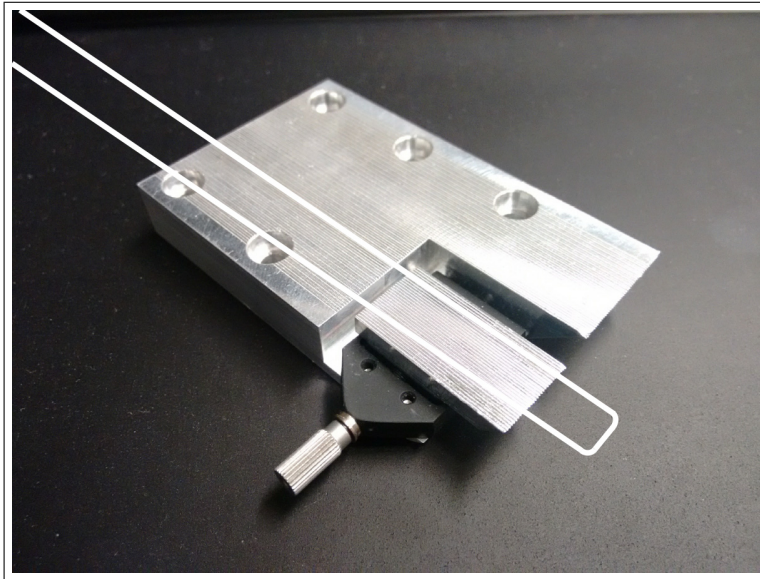


Figure 3.14: Picture of a fiber taper mount used to hold the fiber taper in a U-shape. The placement of the fiber is designated by the white line. The dimple would be located in the middle of the U-shape.

Once the fiber taper is dimpled and mounted, its performance must be tested. The most important parameter is the transmission and is quoted in percentage over the original transmission before tapering. Other parameters include the taper diameter, the taper length, and the dimple radius of curvature. The fiber is also inspected for any debris and defects. The mount is then installed into the measurement setup which will be discussed below. A detailed procedure and analysis of a similar fiber taper setup can be found in Ref. [104].

Measurement setup

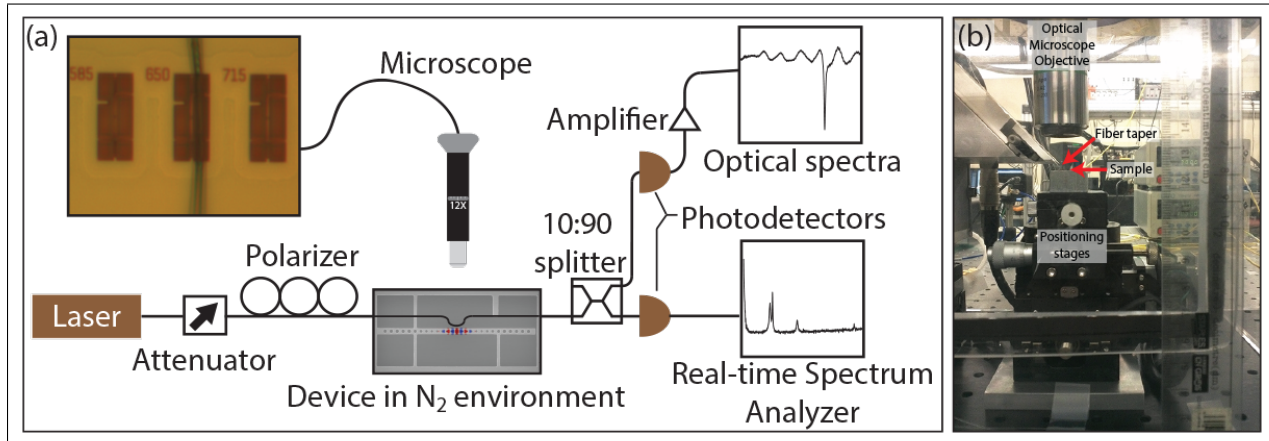


Figure 3.15: (a) Fiber taper measurement setup. (b) Front view through the nitrogen box showing the sample on top of the positioning stages and a fiber taper hovering on top.

The chip under study is manually placed on top of a 2-axis stage (50 nm step size) controlled by a computer program. The fiber is mounted on a z-axis stage such that the dimple can be accurately positioned above individual devices on the chip. The stages, the chip, and the fiber are contained inside a acrylic box where nitrogen gas is continuously flowed. This reduces the amount of water vapor inside the chamber which affects the fiber taper. All measurements are done in ambient conditions (room pressure and temperature) unless mentioned otherwise. A microscope objective positioned above allows visualization of the chip and the fiber for precise alignment (see inset in Fig. 3.15). The fiber can optically address an individual device then be swiftly moved up, shifted laterally, and moved down to address the next device. As described in chapter 2, the dimpled optical fiber taper (1 μm -diameter, $\sim 25 \mu\text{m}$ nominal radius of curvature) evanescently injects light into the nanocavity from a tunable laser source and extracts it back out. The optical power transmitted through the fiber is then split into two channels. The optical transmission, $T(\lambda)$, through the fiber taper was measured using a high-speed photodetector. The optical resonance across the laser wavelengths and the optical power can be monitored. Most of the optical signal is sent to a

real-time spectrum analyzer (RSA) to measure the RF noise spectrum $S_{VV}(f, \lambda)$.

3.5 Split-beam cavity device characterization

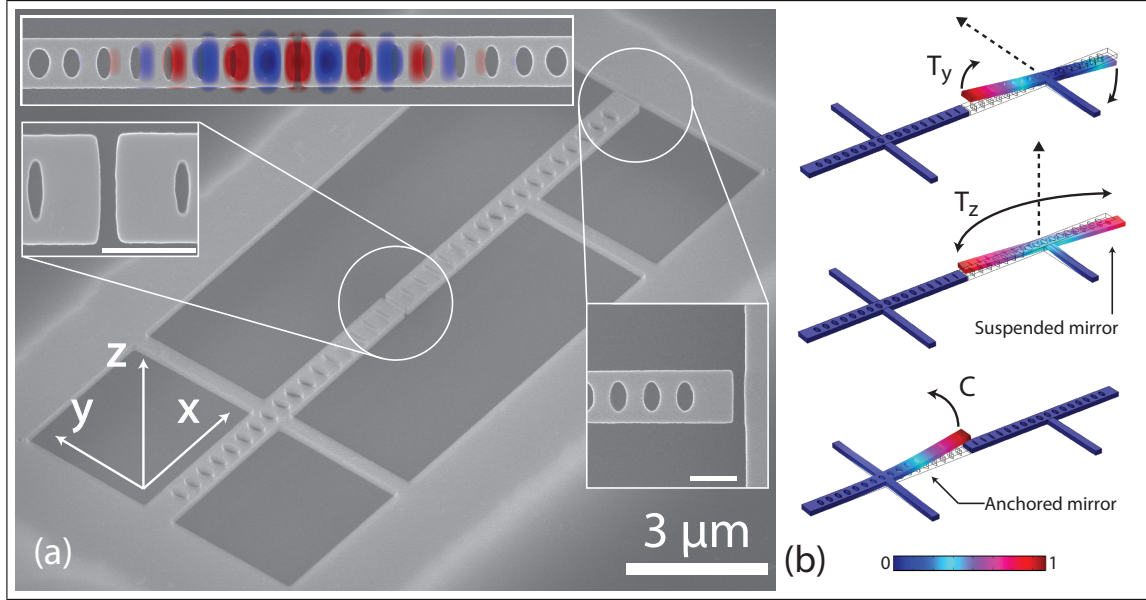


Figure 3.16: (a) Scanning electron micrograph (SEM) of a split-beam nanocavity. Top left inset: top view of the nanocavity overlaid with field distribution (E_y) of optical mode. Left inset: 60-nm-wide nanocavity central gap. Right inset: gap separating the suspended nanobeam from the device layer. Inset scale-bars: 500 nm. (b) Displacement fields of split-beam nanocavity mechanical modes of interest. Dotted arrows indicate position and direction of torque for efficient actuation.

The split-beam nanocavity studied at this stage of device development, with results published in Physical Review X [74], provides a unique platform for studying optomechanics and its impact on torque sensing and measurement. This SBC device support high- Q_o optical modes with designed resonance $\omega_o/2\pi \sim 200$ THz ($\lambda_o \sim 1,550$ nm). The high- Q_o optical mode supported in the gap region has field distribution shown in Fig. 3.16(a) and is characterized by effective mode volume $V_o \sim 0.3 (\lambda_o/n_{Si})^3$ (see appendix B) and radiation loss limited $Q_o \sim 10^4 - 10^6$ depending on the minimum realizable feature size of the elliptical holes. The design of the full structure utilized here is predicted from finite

Mechanical mode		T_y	T_z	C
$\omega_m/2\pi$	(MHz)	4.9	6.4	7.7
m_{eff}	(fg)	427	805	348
Q_m (ambient)		21	83	42
Q_m (vacuum)		1.800	4.400	2.400
$ z, x _{\text{nf}}$ (ambient)	(fm/ $\sqrt{\text{Hz}}$)	6.3	6.9	-
$ \tau _{\text{min}}$ (ambient)	(Nm/ $\sqrt{\text{Hz}}$)	1.2×10^{-20}	1.2×10^{-20}	-
$ \tau _{\text{min}}$ (vacuum)	(Nm/ $\sqrt{\text{Hz}}$)	1.3×10^{-21}	1.7×10^{-21}	-

Table 3.1: Mechanical and sensitivity properties of the split-beam nanocavity mechanical modes. All values are measured experimentally except for the effective mass m_{eff} where numerical simulations were used.

element simulations (COMSOL) to support a mode with $Q_o \sim 3.5 \times 10^4$.

Strategic placement of anchors (also called supports) allow the split-beam nanocavity to support several torsional mechanical resonances suitable for torque detection. The displacement profiles, calculated from simulations and illustrated in Fig. 3.16(b), are characterized by effective mass $m \sim 350 - 800$ fg and frequency $\omega_m/2\pi \sim 5 - 8$ MHz (see Table 3.1). The two lowest-frequency modes involve pivoting of the suspended mirror about its single support. Mechanical resonances of this mirror can be efficiently actuated by coupled sources of torque. They are torsional in the \hat{y} and \hat{z} directions and are thus labeled T_y and T_z , respectively. The third mode, C, is an out-of-plane cantilever-like mode of the triply anchored mirror.

The fabricated nanocavity supports an optical mode at slightly lower resonance wavelength $\lambda_o \sim 1,530$ nm, with unloaded $Q_o \sim 12,000$ due to fabrication imperfections, resulting in a dip in $T(\lambda)$ near λ_o as shown in the white horizontal trace in Fig. 3.17(a). The slight Fano shape (asymmetric lineshape) of the optical resonance is caused by indirect coupling to the fiber taper (see Appendix E for detailed analysis).

A typical measurement of S_{VV} with the fiber hovering above the nanocavity and $\Delta\lambda \sim -\delta\lambda_o/2$, is shown on the right of Fig. 3.17(a). The taper was hovering $\sim 300 - 500$ nm above the nanocavity. Three distinct resonances are visible, indicative of optomechanical transduc-

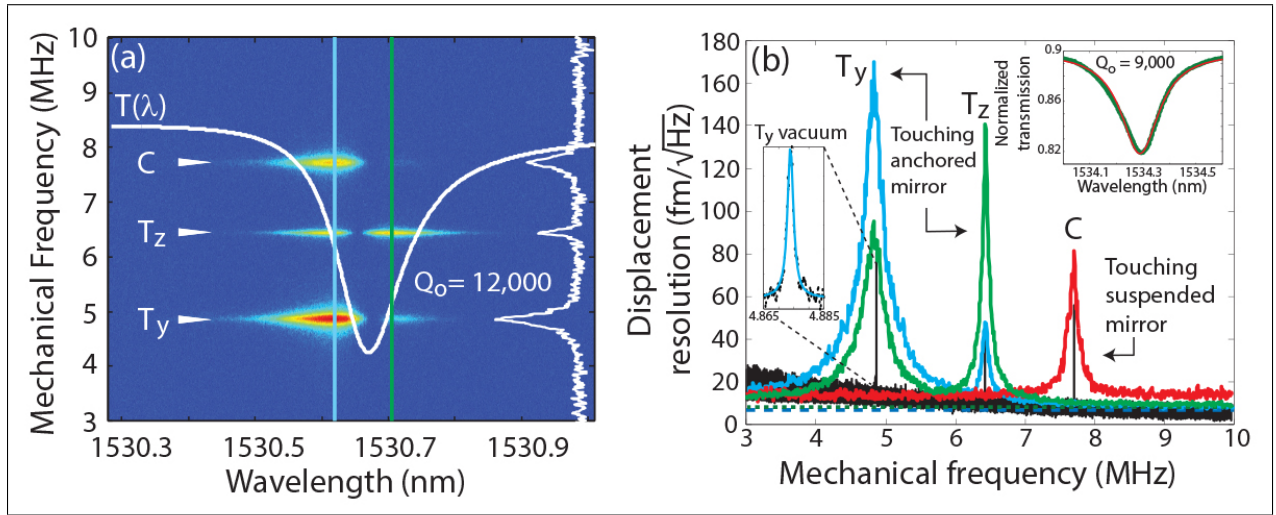


Figure 3.17: (a) $\bar{S}_{VV}(\lambda, \omega)$ in ambient conditions, with fiber taper hovering ~ 300 nm above the nanocavity. $T(\lambda)$ superimposed in white. Right side in white: $\bar{S}_{VV}(\lambda_b, \omega)$ at λ_b indicated by the blue line. (b) Blue (green) data: Calibrated displacement spectrum, $S_{xx}^{1/2}$, of T_y (T_z), when the fiber taper is touching the anchored mirror, with λ set at the blue (green) line in (a). Dotted lines indicate noise floor. Red data: uncalibrated displacement spectrum of C with taper touching the suspended mirror. Black data: vacuum measurement of displacement spectrum, uncalibrated. Left inset: highlight of T_y ($Q_m = 1,800$) in vacuum. Top right inset: $T(\lambda)$ with fiber touching device.

tion of the thermal motion of the T_y , T_z , and C modes. The resonances were identified with mechanical modes through comparison of measured and simulated ω_m , and by observing the effect of touching the fiber taper on each of the mirrors. As shown in Fig. 3.17(b), when the fiber contacts the anchored (suspended) mirror, the C (T_y and T_z) resonance is suppressed, as it is a resonance of the anchored (suspended) mirror. The optomechanical coupling is estimated to be $g_{om} = 1.5$ GHz/nm (details in chapter 4).

Thermomechanical calibration and sensitivity

The mechanical displacement sensitivity of these measurements can be calibrated from $S_{VV}(\omega = \omega_m)$ which is determined by the thermal amplitude of the mechanical resonance [48, 50]. From the measured and calculated mechanical mode properties listed in Table 3.1, noise-floor displacement resolutions, $|z, x|_{nf}$, for the T_y and T_z modes of ~ 6 and 7 fm/ $\sqrt{\text{Hz}}$,

respectively, were measured for $P_i \sim 25 \mu\text{W}$. The minimum detectable torque τ_{\min} associated with the angular motion θ of each mechanical mode can be calculated from Eq. (2.25). From the mirror length of $7.5 \mu\text{m}$ and support length of $3 \mu\text{m}$ and using Eq. (2.25), a thermally limited torque sensitivity of the T_y and T_z modes, in ambient conditions, of $\tau_{\min} \sim 1.2 \times 10^{-20} \text{ Nm}/\sqrt{\text{Hz}}$ were extracted. These values fall within our expected minimum detectable torque predicted in chapter 2. The on-resonance technical noise floors of $4 - 7 \times 10^{-22} \text{ Nm}/\sqrt{\text{Hz}}$ is limited by laser noise and photon shot noise. This technical noise floor, corresponding to the third term in Eq. (2.25), has an effective temperature in the mK range. Using an alternative method for thermomechanical calibration turned similar values for sensitivity [60].

Measurements were also performed in low vacuum where the effect of air damping is reduced. The limit imposed by thermal noise, determined by the first term in Eq. (2.25), can be reduced by decreasing the mechanical damping of the device. An increase in Q_m of the T_y and T_z modes, from $Q_m^{\text{atm}} = 21$ and 83 in ambient, to $Q_m^{\text{vac}} = 1,800$ and $4,400$ at a relatively low vacuum pressure of 2 Torr , was observed as shown in Fig. 3.17(b) and summarized in Table 3.1. For a given set of operating conditions, Eq. (2.25) indicates that this two orders of magnitude improvement of Q_m will enhance sensitivity by an order of magnitude, resulting in thermally limited $\tau_{\min} \sim 1.3 \times 10^{-21}$ and $\sim 1.7 \times 10^{-21} \text{ Nm}/\sqrt{\text{Hz}}$ at 2 Torr for the T_y and T_z modes, respectively. Note that higher Q_m results in a reduced bandwidth of the mechanical response $\chi_m(\omega)$ and is not always preferred for practical applications.

3.6 Summary and implications

This chapter demonstrated the design, fabrication, and characterization of split-beam nanocavities for torsional sensing. The elliptical design of the holes forming the photonic crystal cavity mitigate optical losses resulting from the gap. Our fiber measurement setup is able to individually probe each fabricated SBC device. The fiber taper was also able to actively dif-

ferentiate between certain mechanical modes. Our best devices exhibit high Q_o up to 12,000 and torque sensitivities down to 10^{-20} Nm/ $\sqrt{\text{Hz}}$ in ambient conditions and 10^{-21} Nm/ $\sqrt{\text{Hz}}$ in low vacuum.

The observed torque sensitivity in ambient conditions is better, and wider in bandwidth, than previously demonstrated optomechanical torque sensors in vacuum [53]. Our device compares favorably to the performance of magnetic tweezer torque sensors ($\sim 10^{-21}$ Nm in Ref. [110]). Further improvements in detection sensitivity can be realized through optimization in optical and mechanical properties of the devices [75]. Increasing the fiber-cavity coupling efficiency from the relatively weak coupling demonstrated here ($T_o \sim 0.92 - 0.98$), using single-sided coupling via an integrated waveguide [111], for example, would increase G by an order of magnitude. Similarly, increasing Q_o to 4×10^5 by more accurately fabricating the split-beam nanocavity designs [96] will also enhance G . Moreover, $Q_m > 10^4$ [31] and $g_{om} > 10$ GHz/nm [59] are potentially within experimental reach. Combining these improvements [75], torsional sensitivity could reach $10^{-23} - 10^{-22}$ Nm/ $\sqrt{\text{Hz}}$ or even 10^{-24} Nm/ $\sqrt{\text{Hz}}$ at cryogenic temperatures [54].

The gap between the two mirrors of the SBC nanocavity holds the strongest field in the optical mode. This air space can house other nanoscale systems (such as atoms, nanocrystals, nanoparticles, etc.) and can be of potential use for cavity QED, biochemical sensing, microfluidics, and a myriad of applications.

Our design approach for the split-beam cavities focused on the photonic crystal cavity to perfect its optical properties. On the other side of the globe, a group of mechanical engineers in Singapore used their expertise in MEMS to fabricate advanced mechanical systems to externally adjust the optical properties of the split-beam-like nanocavities [112–114]. This scheme provides new and creative avenues for tuning optomechanical devices.

Chapter 4

Dissipative and dispersive optomechanics

4.1 Origin of dissipative optomechanical coupling

In cavity optomechanical systems, mechanical excitations perturb the local dielectric environment, modifying the dynamical properties of the optical resonances [25]. So far in our formalism for optomechanical coupling (see chapter 2), we have primarily dealt with dispersive coupling g_{om} from moving boundaries which is the most prevalent form in the current literature along with the photo-elastic effect g_{pe} . In most nanophotonic cavity optomechanics, this modulation is therefore typically dispersive. In fact, g_{om} is strongest in our split-beam cavities (SBC) when the mechanical motion of the mirror modifies the gap distance in the center as described in chapter 3. In our experiments with our devices, we have further discovered other mechanisms that also affect the optical transmission and are likewise dependent on the mechanical mode. This chapter follows results of my paper published in Physical Review X in 2014 [74]¹.

The schematic in Fig. 4.1 (slightly modified from the concept in chapter 2) illustrates the various couplings possible between the systems in play: a waveguide, an optical cavity, a mechanical resonator, and the environment (also called the “bath”, for both optical and mechanical channels). In our particular setup, an external applied torque τ acts on the mechanical resonator with mechanical frequency ω_m and mechanical quality factor Q_m . The motion of the resonator typically modifies the optical cavity via the dispersive optomechanical coupling g_{om} which modulates its optical frequency ω_o . The schematic points to two other possible pathways in which the mechanical motion can influence the optical transmission. First, vibrations can also modify its coupling to the environment via the dissipative-

¹Copyright 2014 American Physical Society.

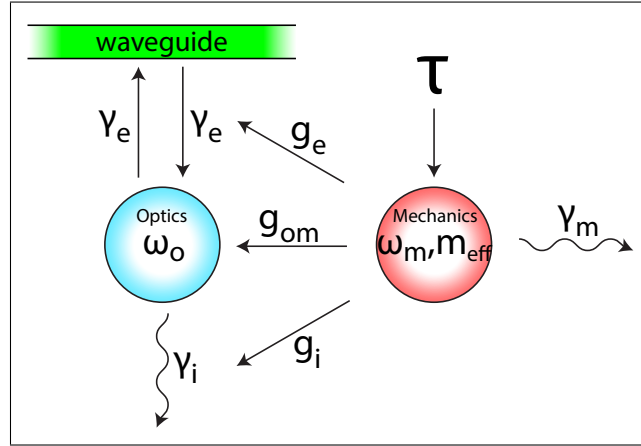


Figure 4.1: Schematic illustrating various couplings between a waveguide, an optical cavity, a mechanical resonator, and the environment.

intrinsic optomechanical coupling g_i (by modulating γ_i , ie. Q_o) and to the waveguide via the dissipative-external optomechanical coupling g_e (by modulating γ_e).

The strength of g_i and g_e , much like g_{om} , depend on the geometry of the device and the setup. Dissipative-intrinsic coupling g_i requires the motion of the resonator to drastically affect the internal photon decay rate γ_i . This is usually the case when a shift in the resonator physically degrades the optical cavity, leading to an increase in γ_i and a reduction of Q_o . The change in transmission is therefore caused by more photons being lost to the environment. In our SBC devices, this effect arises due to the momentary misalignment of the two half-nanobeams disturbing the optical mode supported within the gap. It would be expected that g_i will be small for devices such as microdisks since mechanical stretching (eg. breathing mode) of the mechanical resonator does not affect Q_o . Dissipative-external coupling g_e , on the other hand, requires a setup in which an external waveguide couples to the optical cavity via the external photon decay rate γ_e while the mechanical motion alters γ_e . Physically, this can be achieved when the displacement modulates the distance between waveguide and cavity or, alternatively, the amount of light in the waveguide-cavity coupling.

Note that the mechanical resonator can also directly affect the transmission of light in

the waveguide (or fiber). However, this cavity-less method, though broadband in optical frequencies, is slightly less sensitive with displacement sensitivity near the range of 100 fm to 1 pm/ $\sqrt{\text{Hz}}$ [115–117]. In our experiments, we have found this effect to be much smaller than the coupling via the optical cavity.

4.2 Theory of dissipative and dispersive optomechanical coupling

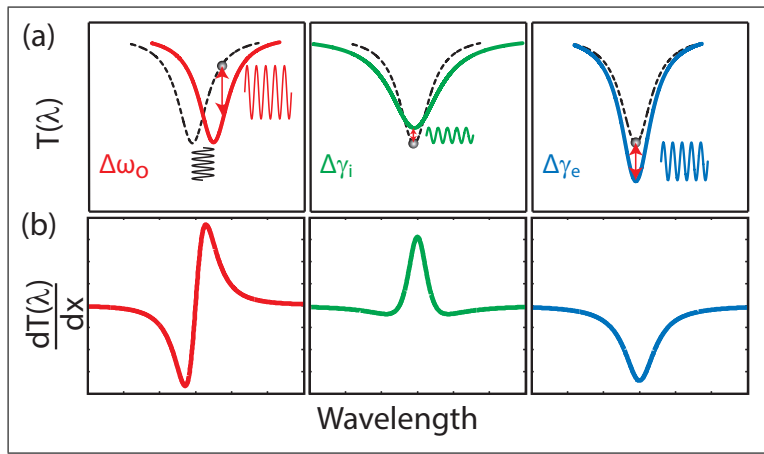


Figure 4.2: Illustration of the effect of mechanical displacement on the optical response of a cavity with (left) dispersive, (center) dissipative-intrinsic, and (right) dissipative-external optomechanical coupling. (a) Change in resonance lineshape. (b) Amplitude of the optomechanically actuated signal which is the derivative of (a) with respect to displacement dx .

Here, we present equations describing the wavelength dependence of the split-beam photonic crystal nanocavity optomechanical response. This model takes into account dispersive and both dissipative optomechanical couplings. The three optomechanical interactions can be probed by monitoring fluctuations in the transmission, $T(\lambda)$ (refer to Eq. (2.7)), of a waveguide or fiber coupling light into and out of the nanocavity, as illustrated in Fig. 4.2(a). In the unresolved sideband regime, where the mechanical frequency is small compared to the optical linewidth, $\omega_m \ll \gamma_t$, the transmission adiabatically follows the mechanical oscillations. The amplitude of the optical oscillations for a given mechanical displacement

amplitude dx would contain additional terms compared to Eq. (2.8) such that

$$\frac{dT}{dx}(\Delta) = \left| g_{\text{om}} \frac{\partial T}{\partial \Delta} + g_i \frac{\partial T}{\partial \gamma_i} + g_e \frac{\partial T}{\partial \gamma_e} \right| \quad (4.1)$$

where $g_{\text{om}} = d\omega_o/dx$ is the dispersive optomechanical coupling coefficient, $g_i = d\gamma_i/dx$ is the dissipative-intrinsic coupling coefficient, $g_e = d\gamma_e/dx$ is the dissipative-external coupling coefficient, and $\Delta\lambda = \lambda - \lambda_o$ is the detuning from resonance.

In our experiment, the optical cavity can couple to additional high-order modes inside the fiber leading to a Fano-shaped optical resonance. The equation for transmission was thus adjusted to include Fano modifications to the cavity response (details in appendix E). The definitions for the derivatives of the modified transmission in Eq. E.7 are

$$\frac{\partial T}{\partial \Delta} = \frac{2\Delta(1-T) + \gamma_e C_f}{\Delta^2 + (\gamma_t/2)^2} \quad (4.2)$$

$$\frac{\partial T}{\partial \gamma_i} = \frac{\gamma_{i+p} - T(\gamma_{i+p} + 2\gamma_e)}{\Delta^2 + (\gamma_t/2)^2} \quad (4.3)$$

$$\frac{\partial T}{\partial \gamma_e} = \frac{-2\gamma_t T + \Delta C_f}{\Delta^2 + (\gamma_t/2)^2}. \quad (4.4)$$

The overall shapes of the three derivatives are plotted in Fig. 4.2(b) (Fano modification omitted, $C_f = 0$). A key feature is that $|\partial T/\partial \gamma_{i,e}|$ are unipolar (single peak at resonance), whereas $|\partial T/\partial \omega_o|$ is bipolar (two peaks at shoulders of the resonance). This will become an important and practical issue as interference between these terms can result in an asymmetric optomechanical wavelength response, $dT(\lambda)/dx$ with respect to detuning $\Delta\lambda$.

To continue our analysis of the optomechanical couplings, the relative ($g_{\text{om}} = g_i = g_e$) and scaled strength of their contributions to δT are plotted in Fig. 4.3(a) and (b), respectively. One striking feature arises: dissipative-external optomechanical coupling is much larger than the other two.

We can quantitatively compare this by evaluating the peak amplitude of the derivatives

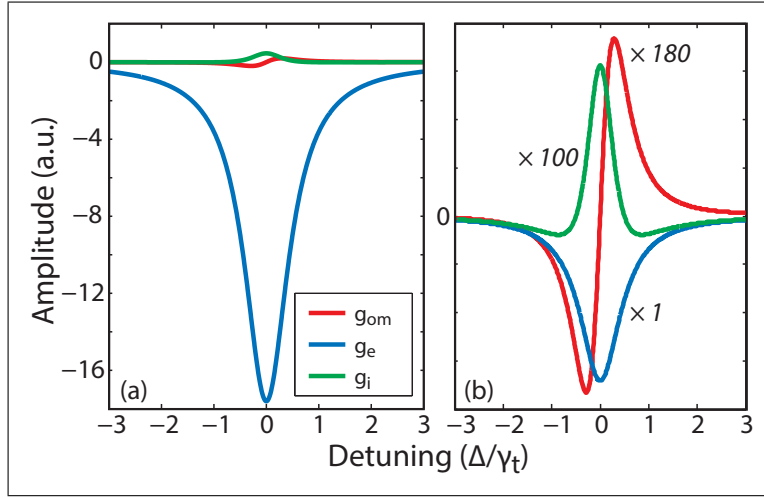


Figure 4.3: (a) Relative strength of the three contributions: $\frac{\partial T}{\partial \Delta}$ (dispersive in red), $\frac{\partial T}{\partial \gamma_i}$ (dissipative-intrinsic in green), and $\frac{\partial T}{\partial \gamma_e}$ (dissipative-external in blue). (b) Comparative strength when contributions are brought to similar amplitudes. Fano modification omitted for display purposes.

(again with $C_f = 0$) [50]:

$$\left. \frac{\partial T}{\partial \Delta} \right|_{\max} = \frac{dT}{d\Delta}(\Delta = \frac{\gamma_t}{2}) = (1 - T_o) \frac{Q_o}{\omega_o} \quad (4.5)$$

$$\left. \frac{\partial T}{\partial \gamma_i} \right|_{\max} = \frac{dT}{d\gamma_i}(\Delta = 0) = 4(1 - T_o) \frac{Q_o}{\omega_o} \quad (4.6)$$

$$\left. \frac{\partial T}{\partial \gamma_e} \right|_{\max} = \frac{dT}{d\gamma_e}(\Delta = 0) = -8T_o \frac{Q_o}{\omega_o} \quad (4.7)$$

where $T_o = \gamma_{i+p}^2/\gamma_t^2$ is the transmission at optical resonance ω_o and $Q_o = \omega_o/\gamma_t$ is the optical quality factor. Combined with Eq. (4.1), maximum contributions to dT from dispersive, dissipative-intrinsic, and dissipative-external optomechanical coupling mechanisms then scale with $Q_o/\omega_o\{(1 - T_o)g_{om}, 4(1 - T_o)g_i, 8T_o g_e\}$, and occur when $\Delta\lambda = \{\delta\lambda/2, 0, 0\}$, respectively, where $T_o = T(\lambda_o)$ and $\delta\lambda = \lambda_o/Q_o$.

A few observations can be made. First, in the under-coupled regime, $\gamma_e \ll \gamma_i$. Thus, g_e has a larger influence on the lineshape due to the fact that the decay rate into the fiber is much smaller ($\gamma_e \approx 1$ GHz) compared to the cavity linewidth ($\gamma_i \approx 30$ GHz). Second, due to small fiber-cavity coupling ($T_o \approx 1$), a change in the fiber coupling has larger influence

on the transmission near resonance such that $\frac{\partial T}{\partial \gamma_e}$ dominates over the other terms as seen in Fig. 4.3(a). Hence, a small value of g_e can have greater effect on the change in transmission than large values of g_i and g_{om} . And lastly, transduction via g_e does not vanish when $T_o \rightarrow 1$, i.e., for under-coupled nanocavities ($\gamma_e \ll \gamma_i$). However, g_e itself does vanish as the fiber taper moves further away from the cavity resulting in degradation of the transduction signal.

In our SBC device measured in this chapter, all three optomechanical couplings play a role in the output signal measured via the power spectral density $S_{VV}(\lambda, \omega)$ in Eq. (2.18). The superposition of the three terms from Eq. (4.1) will create unique wavelength responses in $dT/dx(\lambda)$ for each geometry of the mechanical mode. In particular, a good mix of $g_{om,i,e}$ at the optimal detuning combined with high Q_o and input power P_i can be used to maximize optomechanical gain $G(\lambda)$. However, dissipative coupling is often small compared to dispersive contributions and to date has only been reported experimentally in hybrid cavity-nanomechanical systems where $g_e \sim 10 - 20$ MHz/nm [118, 119]. In our experiments below, measurements indicate that $g_{om} \sim 2$ GHz/nm, $g_i \sim 300 - 500$ MHz/nm and $g_e \sim 2 - 3$ MHz/nm.

4.3 Experimental observation of dissipative coupling

In this chapter, the device under study is the split-beam cavity designed and characterized at the end of chapter 3. Two torsional mechanical modes T_y and T_z are located on the suspended mirror while the cantilever mode C is on the anchored mirror.

The role of dissipative optomechanical coupling and its effect on torque detection sensitivity was studied by measuring the wavelength response of the RF spectrum. Examining $\bar{S}_{VV}(\lambda, \omega)$ and $T(\lambda)$ in Fig. 3.17(a), it is evident that the optomechanical transduction of each of the three mechanical resonances exhibits a unique λ dependence. This stems from differing relative contributions of dissipative and dispersive coupling. $S_{VV}(\lambda, \omega_m)$ of a purely dispersive cavity-optomechanical system, operating in the unresolved sideband regime, should follow

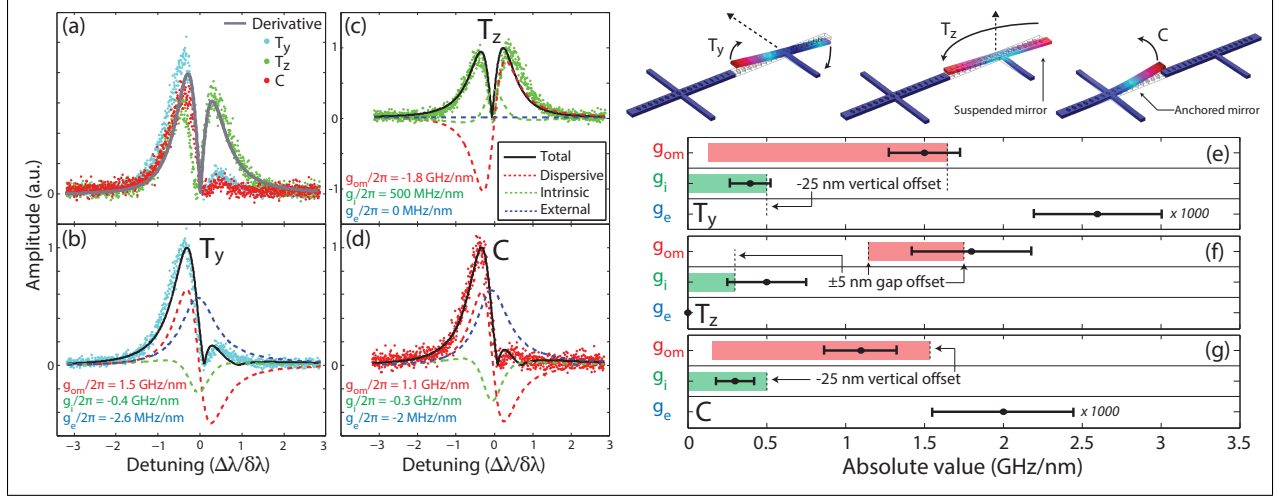


Figure 4.4: (a) $\bar{S}_{VV}^{-1/2}(\lambda, \omega = \omega_m)$ of C , $T_{y,z}$ modes. Grey line is scaled $dT(\lambda)/d\lambda$. (b) – (d) Fit (black line) of optomechanical coupling model to $\bar{S}_{VV}^{-1/2}(\lambda, \omega = \omega_m)$ of (b) T_y , (c) T_z , and (d) C modes. Dashed colored lines indicate relative contributions from dispersive, external dissipative, and intrinsic dissipative coupling. (e) – (g) Comparison between fit values (black points) and numerically simulated values (shaded regions) of g_{om} , g_i , and g_e . Width of color boxes represent numerically simulated range due to fabrication imperfections.

the slope $|dT/d\lambda|^2$ (grey line shown in Fig. 4.4(a)). However, $\bar{S}_{VV}(\lambda, \omega_m)$ of T_y , T_z , and C do not follow $|dT/d\lambda|^2$, and are asymmetric with respect to $\pm\Delta\lambda$. This asymmetry can be characterized by $\zeta^2 = \bar{S}_{VV}^+/\bar{S}_{VV}^-$, where \bar{S}_{VV}^\pm is the maximum RF sideband signal for $\Delta\lambda \gtrless 0$. The slight Fano profile of $T(\lambda)$, due to nanocavity coupling to higher-order waveguide modes discussed in the previous section, would result in an $\zeta \sim 0.8$ for purely dispersive optomechanical coupling, and does not explain the observed results. In comparison, $\bar{S}_{VV}(\lambda, \omega_m)$ of the out-of-plane T_y and C modes, shown in Figs. 4.4(b) and (d), are characterized by $\zeta \sim 0.24$ and 0.19 , respectively. The in-plane mode T_z is characterized by $\zeta \sim 1.1$, as shown in Fig. 4.4(c).

The relative contribution of each optomechanical coupling process can be estimated by fitting $\bar{S}_{VV}(\lambda, \omega_m)$ with a model described by Eqns. (4.4) which includes dispersive, intrinsic dissipative, and external dissipative optomechanical coupling, and takes into account the slight Fano shape of $T(\lambda)$. The resulting fits, estimates for g_{om} , g_i , and g_e , and relative contributions to the optomechanical response, are displayed in Figs. 4.4(b) – (d). The large

asymmetry in T_y and C is attributed primarily to external dissipative coupling, resulting from a variation in fiber–nanocavity gap caused by the motion of the mirror, and is quantified by $g_e \sim -2.6$ MHz/nm. The T_z mode is predominantly dispersive, and good agreement with theory is realized with $g_e = 0$. In order to realize best fits in all of the modes, significant intrinsic dissipative coupling must be included, with $g_i \sim 300 - 500$ MHz/nm. Note that in the case of the out-of-plane C and T_y modes, contributions from g_e effectively double the displacement sensitivity of the optomechanical measurement. Furthermore, even for modest g_e , the relative contribution to the optomechanical gain G is significant, despite the weak waveguide–nanocavity coupling used here, owing to $G|_{\max} \propto T_o$ for external dissipative coupling.

The fit values for g_{om} , g_i , and g_e were compared with values predicted from numerical simulations, as summarized in Figs. 4.4(e-g) and analyzed in the next section. A range of values for g_i and g_{om} , accounting for uncertainties in device fabrication, were calculated by directly simulating the optical properties of the nanocavity resonance as a function of mirror displacement. For T_z , the in-plane motion of the suspended mirror contributes to g_{om} and g_i . An uncertainty of ± 5 nm in the gap size results in the predicted range of g_{om} and g_i shown in Fig. 4.4(f). Due to fabrication imperfections unaccounted for in simulations, experimental values can be slightly higher; error bars from the fitting routine, however, fall within the predicted range. For the out-of-plane T_y and C modes, broken vertical symmetry can give rise to significant g_{om} [43]. Notably, a vertical sagging of the suspended mirror by a plausible offset of 25 nm, as indicated in Fig. 4.4(e) and (g), can give rise to g_{om} and g_i values comparable to fit value for T_z . Note that renormalization of the nanocavity near field by the waveguide can also contribute to g_{om} . Finally, the values for g_e extracted from the fits are comparable to experimentally observed dependence of γ_e on waveguide–nanocavity gap [120].

The contribution of dissipative coupling strongly affects torque sensitivity in our device.

In its absence, T_z would dominate the optomechanical response in Fig. 3.17(a). However, the addition of dissipative coupling into the mix of optomechanical interactions allowed the signal from T_y to be stronger at one sideband. As such, the peak signal in Fig. 4.4(b) corresponds to the peak at 4.9 MHz in blue in Fig. 3.17(b) giving T_y comparable sensitivity of $1.2 \times 10^{-20} \text{ Nm}/\sqrt{\text{Hz}}$ as T_z .

4.4 Numerical simulations of optomechanical couplings

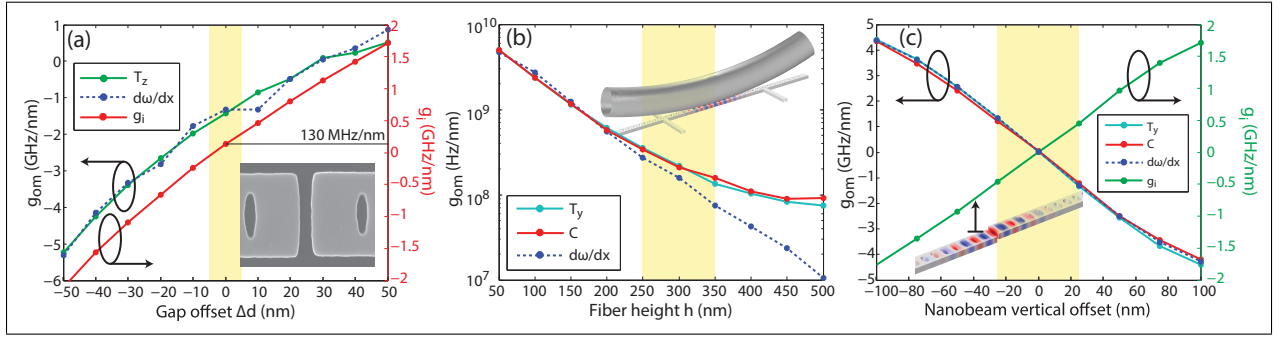


Figure 4.5: Numerical simulation of the coefficients g_{om} and g_i from finite element simulations (COMSOL). Dashed line g_{om} data calculated directly from $\omega(x)$. g_i calculated from $\gamma_i(x)$. All other data points calculated perturbatively. (a) Dependence of g_{om} (left axis) and g_i (right axis) of torsional mode T_z on the variation in the gap size d . The shaded area corresponds to uncertainty in gap (± 5 nm) due to fabrication tolerances and SEM image resolution. (b) Fiber-induced dispersive optomechanical coupling coefficient g_{om} of the out-of-plane modes T_y and C . Shaded area indicates the uncertainty of the fiber height h . Larger g_{om} values at higher h are due to limited finite-element resolution. (c) Dependence of g_{om} (left axis) and g_i (right axis) for out-of-plane modes on vertical offset of the suspended mirror. Shaded area corresponds to a region of uncertainty (± 25 nm) in the vertical position of the suspended mirror due to post-fabrication stresses and substrate effects.

Numerical simulations were performed to predict the dispersive, g_{om} , and dissipative-internal, g_i , optomechanical coupling coefficients for each of the mechanical modes of the split-beam nanocavity. In addition to predicting g_{om} of the torsionally actuated T_z mechanical mode of the split-beam nanocavity, these simulations assess the effect on the optomechanical coupling of fabrication imperfections and the presence of the optical fiber taper

in the nanocavity near field. All simulations in this chapter were performed using COMSOL finite element software to calculate the mechanical and optical mode field distributions and properties ω_o , ω_m , m , and γ_i . Dispersive optomechanical coupling coefficients g_{om} were calculated using COMSOL (see Appendix B), and also directly from $g_{om} = d\omega_o/dx$ where $\omega_o(x)$ is the optical mode frequency as a function of mechanical displacement x . Dissipative g_i were calculated directly from $d\gamma_i/dx$. Simulations were performed for a range of device dimensions consistent with our observed fabrication tolerances.

The in-plane motion of the T_z mode modulates the split-beam gap width d , resulting in a large dispersive optomechanical coupling. Figure 4.5(a) shows g_{om} for this mode as a function of an offset Δd away from the nominal value of $d = 60$ nm. For $\Delta d = 0$, $g_{om} = -1.5$ GHz/nm is predicted, using both perturbation and direct $d\omega/dx$ calculation techniques. If d is not optimized, small displacements of T_z will also modify γ_i . For our best estimate of the gap size, simulations predict $g_i = 130$ MHz/nm, however within the uncertainty in position this value can vary.

Due to the different vertical symmetry of the nanocavity optical mode, and the displacement fields of out-of-plane modes T_y and C, their optomechanical coupling coefficients g_{om} and g_i are expected to be zero. However, the vertical symmetry of the optical mode is broken in two ways in the device studied here. Interactions between the nanocavity evanescent field and the optical fiber taper, for small fiber taper height h above the nanocavity surface, modify the effective refractive index of the nanocavity. This effect is described by an h -dependent $g_{om}(h)$ which can reach the GHz/nm range, as shown in Fig. 4.5(b). Fabrication imperfections in the device and the fabrication process can also break vertical symmetry. Notably, offset bending between the two mirrors can arise due to differential internal stresses in each beam and stiction forces due to the proximity of the substrate. This is referred to as “sagging” in the discussion below. Figure 4.5(c) illustrates the effect of sagging in the suspended mirror, resulting an offset in the z -direction with respect to the anchored mirror.

Broken vertical symmetry also manifests in non-zero intrinsic dissipative optomechanical coupling for the out-of-plane modes. Sagging of the suspended mirror shifts the nanocavity cavity mode away from the minimum intrinsic loss γ_i , resulting in $g_i = d\gamma_i/dx < 0$, as shown in Fig. 4.5(c).

Numerical simulations for the fiber–cavity external coupling coefficient g_e were inconclusive at this point. For typical values of $g_e \sim 2$ MHz/nm [118–120], the change in Q_o for our cavity ($Q_o \sim 12,000$) due to a change h of 100 nm would be in the order of $\Delta Q \sim 100$, which is below the uncertainty of our numerical simulations for this specific device. In close proximity of the fiber to the nanocavity, calculations of Q_o from numerical simulations become increasingly unstable.

4.5 Applications of dissipative optomechanics

Dissipative interactions in nanophotonic systems is not a novel concept. Many optical micro- and nanocavities exploit dissipation to detect the presence of an external material such as nanoparticles and biological molecules [121–123]. Similarly, nanomechanical resonators have been used as biochemical sensors often via shift in ω_m or dissipation [124].

At the publication of our paper [74], dissipative optomechanical coupling was reported only sporadically. Dissipative-intrinsic optomechanical coupling has been theoretically studied since 2009 [125–131] while dissipative-external optomechanical coupling was observed by a few groups [118, 119, 132].

Since then, growing interest in exploiting dissipative optomechanical coupling for applications in the quantum regime [133–136] has culminated with the first experimental observation of cooling using dissipative optomechanics down to millikelvin temperatures [137]. With a single peak at zero detuning for dissipative-intrinsic ($\frac{\partial T}{\partial \gamma_i}$) and dissipative-external ($\frac{\partial T}{\partial \gamma_e}$), it is possible to exploit optomechanics at resonance provided dissipative coupling is stronger than dispersive. By careful mixing of the coupling rates, optomechanical cooling can arise

through quantum noise interference between dispersive and dissipative couplings with best results occurring when operating with external dissipative coupling. Cavity cooling using dissipative coupling can bypass the requirement of sideband-resolved regime so that the mechanical frequency can be lower than the cavity bandwidth. As a side effect, the dissipative scheme can allow macroscopic and low frequency mechanical resonators (such as those used for detecting gravitational waves) to be cooled to down to the quantum regime [138].

4.6 Summary and implications

In this chapter, we demonstrated that dissipative optomechanical coupling, where mechanical excitations modulate the nanocavity photon lifetime or the waveguide-cavity coupling, can also play a crucial role in optical transduction of nanomechanical motion. The interaction of dissipative and dispersive optomechanical coupling is experimentally observed in a photonic crystal split-beam nanocavity optimized for detecting nanoscale sources of torque. Dissipative coupling of up to ~ 500 MHz/nm and dispersive coupling of 2 GHz/nm enabled measurement of a sub-pg out-of-plane torsional mechanical resonance with improved thermally-limited torque detection sensitivity down to 1.2×10^{-20} Nm/ $\sqrt{\text{Hz}}$ in ambient conditions. Interference between optomechanical coupling mechanisms is observed to enhance detection sensitivity and generate mechanical-mode-dependent optomechanical wavelength response.

For proposals of dissipative optomechanics in the quantum regime, it is desirable to reduce dispersive coupling and maximize dissipative coupling. This can potentially be achieved in split-beam nanocavities. Simulations indicate that internal dissipative coupling of the T_z mode can become dominant if the mirror gap is increased by 50 nm, where $\{g_{\text{om}}, g_i\} \rightarrow \{0, 1.5 \text{ GHz/nm}\}$. In the case of the T_y and C modes, g_e/g_{om} may be increased by reducing the single mirror “sag” believed to be largely responsible for the appreciable g_{om} measured for these modes. This was achieved in devices with symmetrically supported mirrors. The

results are reported in the next chapter.

Chapter 5

Tuning of dissipative and dispersive optomechanical coupling

The material presented in this chapter follows results of our paper published in *Optica* in 2015 [139]. My contributions to this particular project include extensive device measurements at different fiber heights and axial positions, FEA numerical simulations for the optical and mechanical modes including the fiber, and quantitative analysis and fits of optomechanical couplings.

5.1 Optical field renormalization using near-field fiber probe

This chapter showcases results which build upon the previous chapter by demonstrating externally tuned dispersive coupling g_{om} and dissipative-external coupling g_e . We illustrate that these parameters can be controlled with the fiber taper and used to spatially resolve nanomechanical resonances. Since the fiber does not affect dissipative-intrinsic optomechanical coupling and to simplify the number of parameters during tuning, the device was designed to reduce or eliminate g_i . Therefore, in this chapter, dissipative coupling will only refer to dissipative-external coupling g_e .

As discussed in the previous chapter, the optomechanical coupling strength central to the performance these devices is geometry dependent. In particular, the coupling may vanish if the spatial symmetry of the optical and mechanical resonances of interest differ. In an ideal planar structure, small displacements of a cantilever mode would not be transduced by a centered optical field, as the average refractive index sampled by the optical field varies quadratically as one of the mirrors is displaced vertically. This can be seen from the

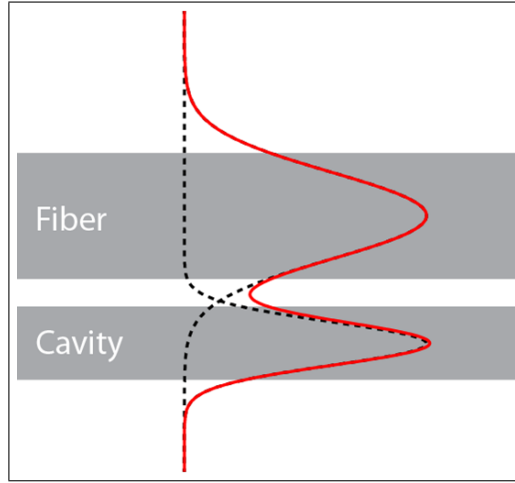


Figure 5.1: Schematic of the optical fields confined inside the fiber and cavity separately (black dotted lines) or when brought in close proximity (red line). Image courtesy of Aaron Hryciw.

expression for g_{om} in Eq. (2.4) where the fundamental TE-like mode intensity varies as $|E|^2$ and possesses even vertical symmetry (see black line in the cavity in Fig. 5.1). In contrast, the vertical symmetry of the mechanical mode profile $\mathbf{u}(r)$ is odd in a cantilever resonance: motion with respect to the top and bottom surface normals of the cantilever is equal and opposite. This combination of optical and mechanical geometries cause g_{om} to vanish for cantilever modes.

Non-zero optomechanical coupling can be introduced by breaking the vertical symmetry of the structure. While fabrication imperfections or the presence of a substrate can break this symmetry [53, 140], the resulting g_{om} is typically small. The fiber taper waveguide provides an effective method for symmetry breaking via position-dependent dissipation into the fiber and a renormalization of the nanocavity field.

Here we demonstrate that a near-field probe can be used to reconfigure the optomechanical properties of a nanocavity, enhancing readout of mechanical resonances. An optical fiber taper positioned in the nanocavity near field can renormalize the nanocavity optical mode. This distortion of the vertical profile of the cavity field as shown by the red line in Fig.

5.1 can modify both its sensitivity to individual mechanical resonances and the balance of dissipative and dispersive nanocavity optomechanical coupling processes. In consequence, the optical fiber taper waveguide placed in the near field of the nanocavity can induce both large dispersive and dissipative optomechanical coupling, whose magnitude can be tuned by adjusting the fiber position.

5.2 Quarter-wave shifted photonic crystal cavities

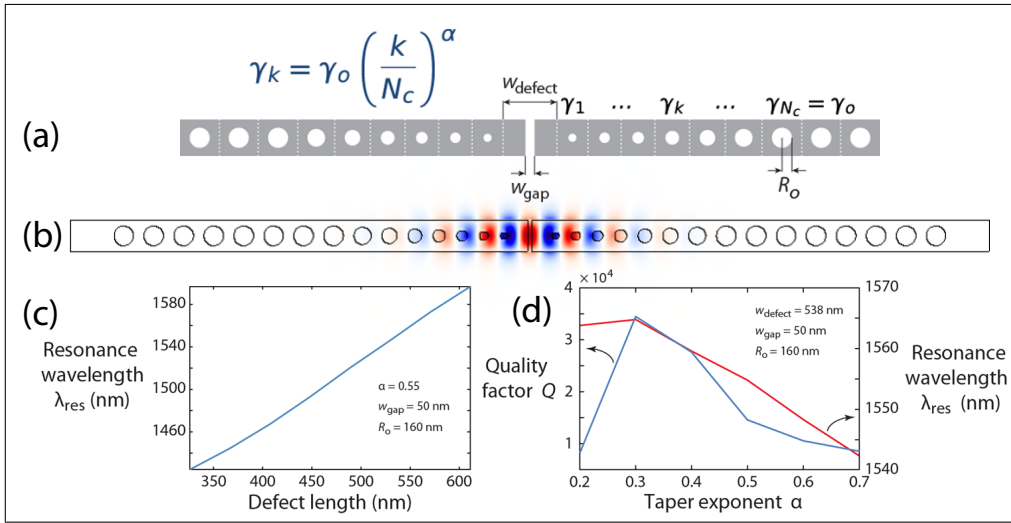


Figure 5.2: Design of quarter-wave shifted (QWS) nanobeam photonic crystal cavities. (a) Schematic of the QWS device with holes tapering according to the equation γ_k for mirror strength. (b) FDTD numerical simulations of the optical mode. (c) Shift in resonance wavelength λ_{res} as a function of defect length w_{defect} . (d) Q_o and λ_{res} for various taper exponents.

The effects introduced above were studied using a quarter-wave shifted (QWS) photonic crystal nanocavity with circular holes as shown in Fig. 5.2(a). This is an alternative to the SBC design approach to the device with elliptical holes which requires more stringent control on hole dimensions [96]. This design is therefore relatively robust against fabrication imperfections. This QWS device starts with the grating-defect resonator design paradigm of Liu and Yariv [141] then loosely follows the design paradigm described in chapter 3.

End-to-end tapered Bragg gratings are sandwiched around a central defect which imparts a quarter-wave phase shift to the grating coupling coefficient. The total defect length is chosen to minimize radiative loss, as determined from finite-difference time-domain (FDTD) simulations [142].

Unfortunately, the maximum theoretical Q_o of this type of optical cavity only reaches 3×10^4 (see Fig. 5.2(d)). This low finesse is a price to pay to render the fabricated device insensitive to small fluctuations in hole sizes. Moreover, our limited knowledge of this design reduces potential improvements. The QWS design was therefore abandoned (after completion of the project described in this chapter) to give preference to the SBC design.

5.3 Characterization of QWS optomechanical devices

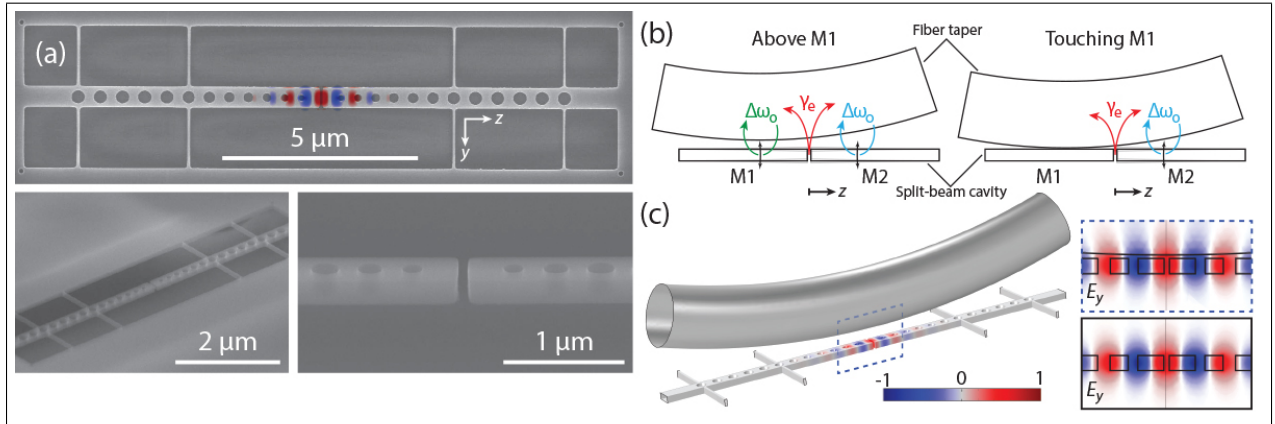


Figure 5.3: (a) Scanning-electron micrographs of a quarter-wave shifted photonic crystal nanocavity with circular holes. The nanocavity optical mode (E_y) is superimposed on the device in the upper image. (b) Schematic of experimental geometry when fiber is hovering above (left) and touching (right) one of the mirrors. (c) Renormalization of the optical mode by the optical fiber taper. The field plots show E_y in the center of the cavity with (upper) and without (lower) the fiber taper. The red-blue scale bar indicates the normalized electric field amplitude for all figures.

The fabricated device supports an optical mode whose field profile with small mode volume overlapping strongly with the central gap region (~ 80 nm), as shown in Fig. 5.3(a).

Each mirror was anchored in five locations such that only the out-of-plane cantilever motion is preferred, allowing for study of g_e as well as reducing the number of natural mechanical vibrations. The device was designed to be symmetric across the gap defect in order to reduce or eliminate g_i . Ideally, the lack of vertical offset between the two mirrors (or half-nanobeam) would result in $g_{\text{om},i} = 0$ according to our simulations in Fig. 4.5(c).

In the following experiments, the fiber taper was positioned such that it hovered above the nanocavity or placed in contact with either of the nanocavity mirrors. When hovering above the left mirror (M1 in Fig. 5.3(b)), the fiber taper should be able to detect the motion of both mirrors via dissipative-external optomechanical coupling g_e (modulation of γ_e) from the optical cavity. It is expected that the optomechanical signal originating from M1 would be stronger since the fiber taper is closer to it. However, when the fiber taper physically touches upon M1, its mechanical motion is damped such that only signal from M2 should be received as shown on the right in Fig. 5.3(b). Fig. 5.3(c) depicts the renormalization effect of the fiber taper on the optical mode showing a modified optical field in the presence of the fiber.

Figure 5.4(a) shows $T(\lambda)$ when the fiber taper is hovering ~ 500 nm above the nanocavity. The sharp dip in transmission at $\lambda_o \sim 1,522$ nm results from evanescent coupling between the fiber taper and the optical mode of the nanocavity. From the linewidth, $\delta\lambda$, and minimum transmission, T_d , of this resonance, the loaded and unloaded quality factors of the device are measured to be $Q_o \sim 5,200$ and $Q_i \sim 5,500$, respectively.

Figure 5.4(b) shows the power spectral density (PSD), $S_{\text{VV}}^{1/2}(f)$, of the measured fiber taper transmission signal when the input laser is red detuned at $\lambda - \lambda_o \sim \delta\lambda/2$ and the fiber taper is in contact with one of the nanocavity mirrors, labeled M1. Several sharp resonances are visible, each corresponding to optomechanical transduction of the thermal motion from mechanical resonances of the mirror not in contact with the fiber, labeled M2. The large peak in $S_{\text{VV}}^{1/2}(f)$ at $f_m \sim 10.5$ MHz shown in Fig. 5.4(b) is from thermal motion and subsequent

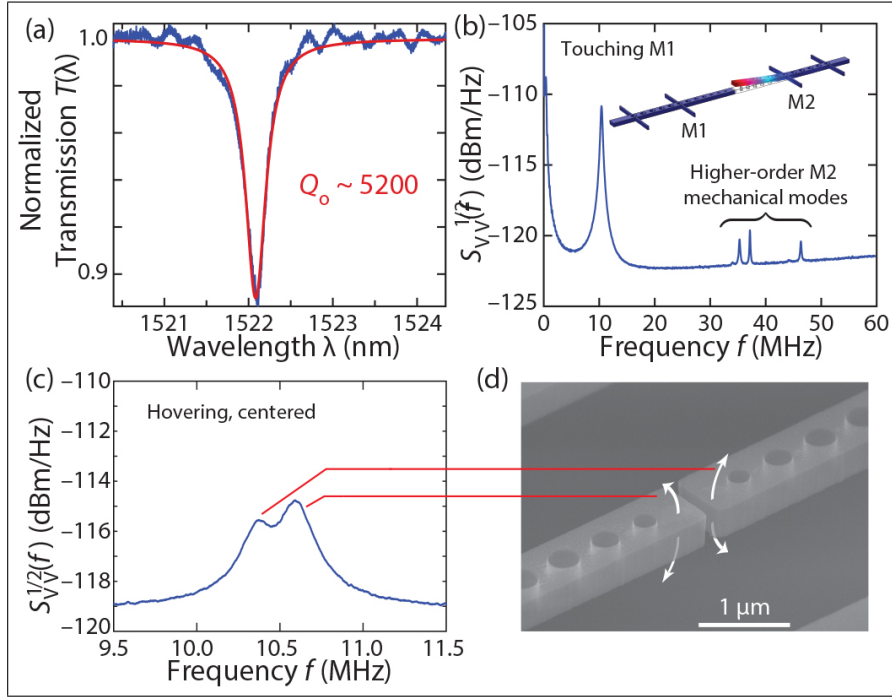


Figure 5.4: (a) Fiber taper transmission under weak coupling (taper height $h \sim 500$ nm). (b) Mechanical mode spectrum when the fiber is in contact with M1. The displacement profile of the fundamental cantilever mode of M2 is shown next to the corresponding peak (amplitude greatly exaggerated). (c) Mechanical mode spectrum with the fiber hovering above the cavity center ($z_f \sim 0$), as close as possible without touching the cantilevers ($h < 150$ nm); the laser detuning was chosen to maximize the peak magnitude. Fabrication imperfections impart a ~ 200 kHz splitting between these resonances. (d) Scanning-electron micrograph of the split-beam cavity center.

optomechanical coupling from the fundamental cantilever (C) mode of M2.

When the fiber taper is positioned in a hovering configuration over the center of the cavity such that it is very close to (although not in contact with) M1 or M2, optomechanical coupling is still present, as shown in Fig. 5.4(c). In the hovering configuration, the peak in $S_{VV}^{1/2}(f)$ has a lower amplitude and a double-peaked structure. Each of these local maxima can be ascribed to optomechanical coupling between the nanocavity and the C mode of M1 and M2, whose mechanical frequencies, $f_1 = 10.4$ MHz and $f_2 = 10.6$ MHz, respectively, differ slightly due to fabrication variations.

5.4 Experimental tuning of optomechanical couplings using near-field fiber probe

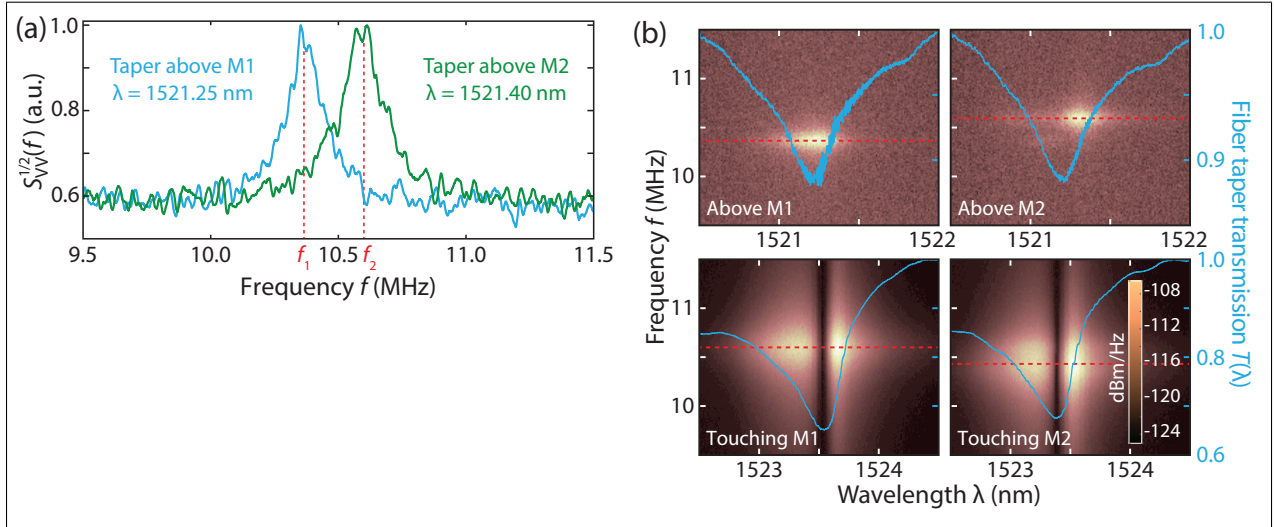


Figure 5.5: (a) Mechanical spectrum $S_{VV}^{1/2}(f)$ of cantilever modes with fiber hovering ~ 250 nm above M1 (blue) and M2 (green). In each case, the wavelength was tuned to maximize the mechanical resonance. (b) $S_{VV}^{1/2}(f, \lambda)$ for the fiber hovering above/touching M1/M2, with the maxima with respect to f marked by the red dotted lines. The DC fiber transmission for each configuration is shown in blue.

To gain insight into the optomechanical coupling processes responsible for the observed behavior, the nanocavity optomechanical response was measured as a function of axial fiber position z_f (in the direction of the nanobeam length). When the fiber dimple is offset from the center of the nanocavity such that it is hovering above M1 ($z_f \approx -2 \mu\text{m}$), a single peak at f_1 was observed, as shown in Fig. 5.5(a). Similarly, when the fiber hovers above M2 ($z_f \approx 2 \mu\text{m}$), a single peak at f_2 appears. These measurements indicate that the observed optomechanical coupling is not intrinsic to the optical and mechanical modes of the nanocavity alone: the fiber position influences the optomechanical coupling processes.

The mechanism responsible for these observations can be revealed from the λ depen-

dence of $S_{VV}^{1/2}(f, \lambda)$. Figure 5.5(b) shows $S_{VV}^{1/2}(f, \lambda)$ for four different fiber taper configurations: hovering above or touching M1 or M2. In all of the measurements, the maxima in $S_{VV}^{1/2}(f)$, marked by the red dotted lines, were observed at either f_1 or f_2 . In Fig. 5.6(a), fitting $S_{VV}^{1/2}(f_{1,2}, \lambda)$ following the procedure in the previous chapter yields the dispersive and dissipative contributions to the total optomechanical signal.

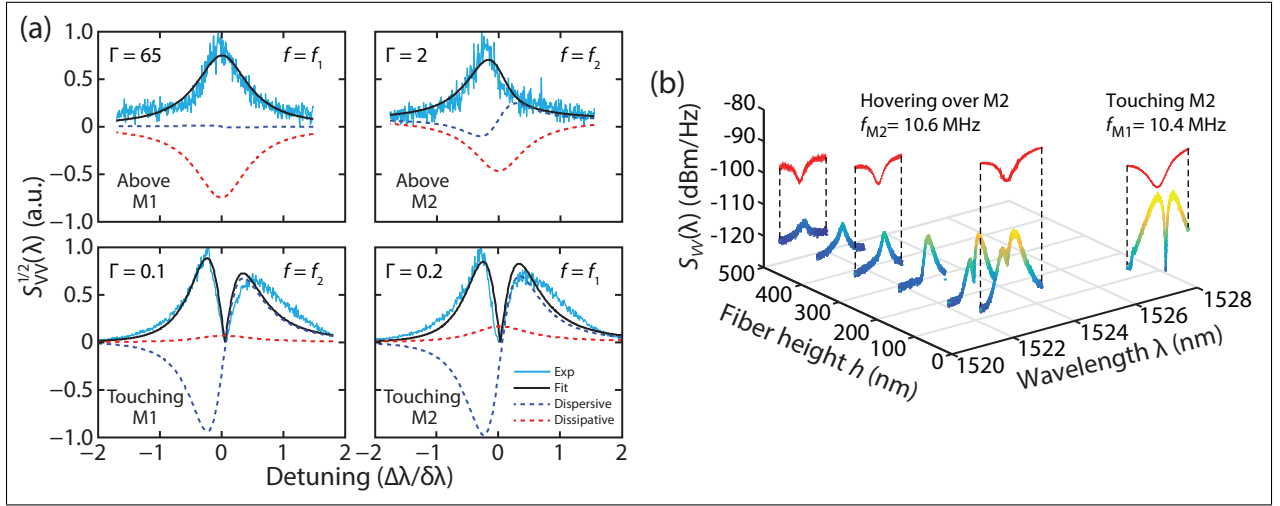


Figure 5.6: (a) $S_{VV}^{1/2}$ vs. detuning, $\Delta\lambda = \lambda - \lambda_o$, for the fiber hovering (upper) and touching (lower) the cantilevers, corresponding to the dotted-line slices in Fig. 5.5(b). The fits use the model in [74]; Γ is given by Eq. (5.2). (b) S_{VV} vs. λ for varying h hovering over M2 ($z_f \approx 2\mu m$) until touchdown ($h=0$); $T(\lambda)$ is shown in red for selected heights.

For the hovering measurements, as λ is tuned toward the optical resonance, optomechanical coupling is observed at f_1 and f_2 when the fiber is positioned above M1 and M2, respectively, as in the fixed- λ measurements in Fig. 5.5(a). The maxima in $S_{VV}^{1/2}(f_{1,2}, \lambda)$ are near $\lambda \sim \lambda_o$, indicating that the optomechanical transduction mechanism is dominantly dissipative [74, 129]. This is in contrast to the more commonly encountered dispersive coupling scenario observed in many nanophotonic cavity optomechanical systems, for which the optomechanical actuation vanishes at resonance ($\lambda = \lambda_o$). This dissipative optomechanical coupling is a result of the fiber–nanocavity coupling rate being modulated by the oscillating vertical displacement of each mirror’s C mode. A full transition from dissipatively to

dispersively dominated spectra is shown in Fig. 5.6(b), where the optomechanical signal as a function of fiber height above M2 is shown. Note that for $h < 200$ nm, fluctuations in fiber position modify λ_o , as discussed below in section 5.7, blurring out the zero in the optomechanical spectrum.

When the dimpled fiber taper is in contact with mirror M1 (M2), the resonance at f_2 (f_1) is observed to dominate $S_{VV}^{1/2}(f, \lambda)$; an asymmetry in $T(\lambda)$ is also introduced due to the coupling to non-localized nanobeam modes which heralds the breakdown of the ideal-coupler regime [74, 143]. In this geometry, the fiber taper interacts with the optical near field and mechanical motion of the non-contacted mirror, with a separation determined by the specific shape of the fiber taper dimple, and damps the mechanical motion of the contacted mirror. In contrast to the hovering fiber taper geometry, the λ dependence of $S_{VV}^{1/2}(f, \lambda)$ in this configuration, shown in the bottom of Fig. 5.6(a), is observed to follow $dT(\lambda)/d\lambda$: it vanishes near resonance, indicating that dispersive coupling is the dominant optomechanical transduction mechanism. For small gaps between the fiber taper and the free nanocavity mirror, the presence of the fiber taper creates a vertically asymmetric dielectric environment (Fig. 5.3(c)), renormalizing the nanocavity optical mode profile and creating non-zero dispersive optomechanical coupling as discussed at the start of this chapter. Note that this renormalization manifests in a static red-shift of λ_o by ~ 2 nm, as seen in Fig. 5.5(b).

5.5 Analysis of dissipative and dispersive optomechanical couplings

To quantitatively estimate the amount of tuning between dispersive and dissipative, we next turn to coupled mode theory combined with our numerical simulations. The system under study is a fiber–nanocavity system in which the distance h changes the coupling rate $\gamma_e(h)$ between the cavity and both the forward- and backward-propagating waves of the fiber as illustrated in Fig. 5.3(b). Here h is defined as the distance between the nanocavity and the

outer boundary of the fiber. The presence of the fiber may also create other loss channels by scattering light away from the fiber or by coupling to higher-order waveguide modes. These are bundled together as parasitic loss rate $\gamma_p(h)$ [144]. The nanocavity itself has a radiation loss rate of γ_{rad} , which can be computed via numerical simulations (FDTD, FEA), and a scattering loss rate γ_s due to fabrication imperfections. Together, they form the intrinsic loss of the nanocavity: $\gamma_i = \gamma_{\text{rad}} + \gamma_s$. The total loss rate γ_t is then given by

$$\gamma_t(h) = \gamma_i + \gamma_p(h) + 2\gamma_e(h). \quad (5.1)$$

To generate the theoretical values for $g_e(h)$, $\gamma_e(h)$ was estimated from FEA (COMSOL) simulations of $\gamma_t(h)$. This was done by extracting $Q_o(h)$ while translating the fiber vertically above the (stationary) nanobeam. Since this method does not exactly model the mechanical mode displacement, the values extracted are only an approximation. Precisely determining $\gamma_e(h)$ given $\gamma_t(h)$ requires knowledge of $\gamma_p(h)$. Here, we assess γ_p based on experimentally observed $T_d(h = 0)$ and $\gamma_i = \gamma_t(h \rightarrow \infty)$, from which the ratio $\gamma_e(0)/(\gamma_e(0) + \gamma_p(0)) = 0.4$ was extracted. Making the simplifying assumption that $\gamma_e/(\gamma_e + \gamma_p)$ is constant for all h allows an estimate of $\gamma_e(h)$ to be determined from the simulated values of $\gamma_t(h)$.

This procedure likely overestimates γ_p for $h > 0$, as γ_p typically decays with h quickly compared to γ_e , i.e. the coupling becomes more ideal as h increases [144]. As a result, this procedure may underestimate γ_e for large h , and underestimate the decay constant Λ_e of g_e .

Figures 5.7(a) and (b) show experimental and FEA-simulated values for the optical quality factor Q_o and the shift in wavelength $\Delta\lambda/\lambda$, respectively, of the cavity resonance. The good agreement in Q_o gives confidence in our approximation of g_e . The smaller shift in wavelength observed in our experiments compared to simulations indicate that the g_{om} values might be smaller than expected. This is confirmed below in Fig. 5.8(a).

In principle, $\gamma_p(h)$ could be measured experimentally; however, this was difficult in the system under study due to the relatively small $h < 500$ nm at which coupling was observed (resulting in significant fiber taper insertion loss) and the poor contrast of the measured

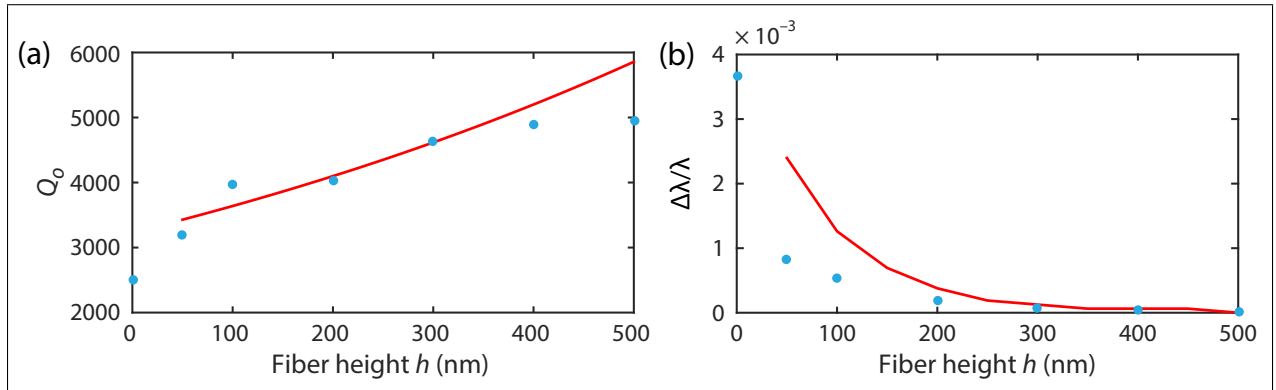


Figure 5.7: Comparison between simulated (red line) and experimental (blue circles) values of (a) optical quality factor Q_o and (b) shift in wavelength $\Delta\lambda/\lambda$ at various fiber heights when hovering above M2 ($z_f = 2 \mu\text{m}$).

nanocavity resonance. In the future, fabrication of nanocavities with higher Q_o may address this difficulty.

Next, we can plot the transition between predominantly dissipative or dispersive optomechanical coupling as a function of vertical fiber taper position, for $z_f = 2 \mu\text{m}$ (above M2). Figure 5.8(a) compares the predicted and measured g_e and g_{om} as a function of taper height, h , above the nanocavity. These simulations predict that for M2, the dispersive $g_{om}(h)$ decays exponentially with h from a maximum absolute value of $\sim 3 \text{ GHz/nm}$, following $g_{om} \sim g_{om}^o e^{-h/\Lambda_{om}}$ with $\Lambda_{om} \sim 75 \text{ nm}$. The dissipative g_e decreases from a maximum value $\sim 10 \text{ MHz/nm}$ with decay length $\Lambda_e \sim 212 \text{ nm}$. As the dispersive g_{om} decays more quickly than g_e , for small h , contributions to the optomechanical coupling from g_{om} dominate the optomechanical signal, while for large h , contributions from g_e may dominate.

The drastically different h dependence of g_{om} and g_e can be understood intuitively from perturbation theory which will be analyzed in the next section. In brief, the fiber perturbs the resonance frequency of the cavity ω_o via a modification of the nanocavity's effective index. The resulting red-shift scales with the overlap of the nanocavity evanescent field intensity and the fiber dielectric [61]; g_{om} consequently shares the exponential decay length of the

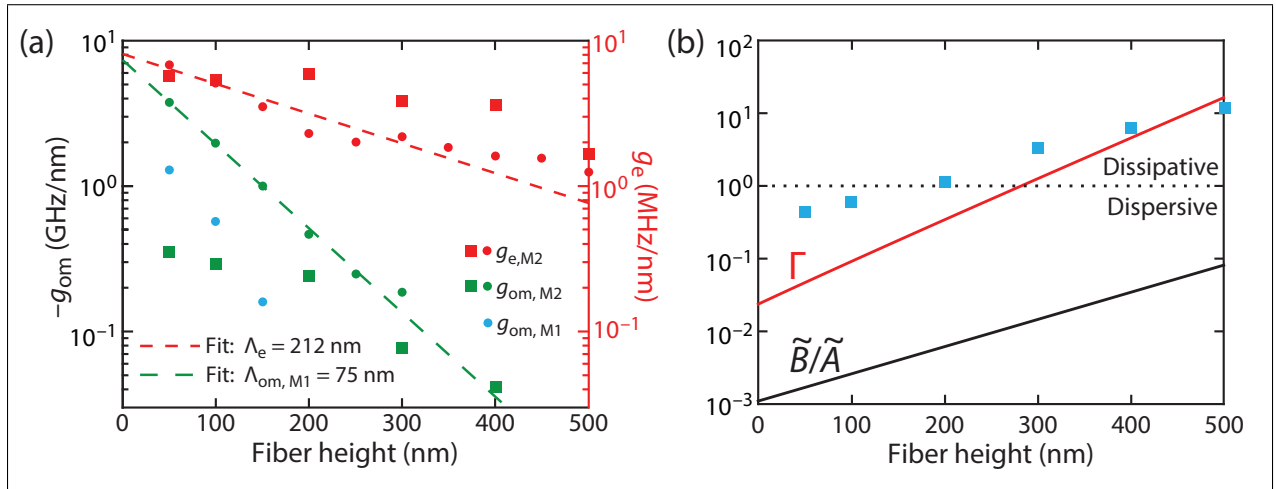


Figure 5.8: (a) Simulated (circles) and experimental (squares) dispersive (g_{om}) and dissipative (g_e) coupling coefficients for the fiber dimple hovering above M2 ($z_f = 2 \mu\text{m}$). Dotted lines indicate fits to numerical simulations. Experimental values are extracted from Fig. 5.6(b). Simulations assume that $g_{e,M1}$ is negligible (i.e., $g_e = g_{e,M2}$) due to relatively large separation between the fiber taper dimple and M1. (b) Simulated $\Gamma(h)$ (red line) and \tilde{B}/\tilde{A} (black line) predicted from the g_e and g_{om} values in (a). Simulated $\Gamma(h)$ also uses an approximation of the experimentally observed $T_d(h)$. Blue squares indicate experimental $\Gamma(h)$ values taken from coefficients in (a).

nanocavity evanescent field intensity. In contrast, γ_e follows from mode coupling between the fiber and nanocavity field amplitudes [145], and therefore contains interference effects inherent to phase matching in addition to depending on the overlap of the evanescent tail of the fiber mode with the cavity. As such, the exponential decay of g_e depends critically on the effective coupling length between the dimpled fiber and the cavity, and is generally slow compared to the decay of g_{om} .

Fits to the optomechanical spectra for varying h in Fig. 5.6(b) provide experimental estimates of g_{om} and g_e . These values are shown in Fig. 5.8(a), and have good correlation with behavior from simulations for $h > 200$ nm. For small $h < 200$ nm, accuracy of the estimates of g_{om} and g_e is reduced due to instability in λ_o resulting from fluctuations in fiber position (see section 5.7 below). These fluctuations reduce the visibility of the dispersive features in $S_{VV}^{1/2}(\lambda)$, and are in part driven by optical attraction or repulsion from the cavity [146].

Disagreement in observed and simulated values can also be caused by geometrical variations of the fiber. For example, if the radius of curvature of the fiber would be twice as small, simulations predict that g_{om} would be roughly halved. In addition, for small h the validity of the standard two-port fiber–nanocavity coupled mode theory used to predict $T(h, \lambda)$ becomes less accurate, and parasitic effects such as insertion loss become appreciable.

The effect on the overall character of the optomechanical transduction is analyzed theoretically and experimentally in Fig. 5.8(b). In the sideband-unresolved regime applicable here ($\omega_{\text{m}} \ll \gamma_{\text{t}}$, where γ_{t} is the total nanocavity optical mode energy decay rate), the maximum dispersive and dissipative contributions to the change in optical transmission are $\left. \frac{dT}{d\omega_{\text{o}}} \right|_{\text{max}} = (1 - T_{\text{d}})Q_{\text{o}}/\omega_{\text{o}}$ and $\left. \frac{dT}{d\gamma_{\text{e}}} \right|_{\text{max}} = -8T_{\text{d}}Q_{\text{o}}/\omega_{\text{o}}$, respectively (see section 4.2).

For weak fiber–nanocavity coupling ($1 - T_{\text{d}} \ll 1$) and for the mechanical modes with minimal intrinsic dissipative optomechanical coupling ($d\gamma_{\text{i}}/dx \ll d\gamma_{\text{e}}/dx$), as in the system studied here, the dissipative contribution to the measured optomechanical signal is dominated by γ_{e} [74]. As such, we express the relative balance of experimentally observed dissipative and dispersive signal by the ratio Γ given below:

$$\Gamma = \left| \frac{g_{\text{e}} \left. \frac{dT}{d\gamma_{\text{e}}} \right|_{\text{max}}}{g_{\text{om}} \left. \frac{dT}{d\omega_{\text{o}}} \right|_{\text{max}}} \right| = \frac{8g_{\text{e}}(h)T_{\text{d}}(h)}{g_{\text{om}}(h)(1 - T_{\text{d}}(h))}, \quad (5.2)$$

where $\Gamma > 1$ ($\Gamma < 1$) corresponds to a predominantly dissipative (dispersive) contribution to the $S_{\text{VV}}^{1/2}(\lambda)$ lineshape. Note that in this regime contributions to the optomechanical signal from $d\gamma_{\text{p}}(x)/dx$ will be small compared to $d\gamma_{\text{e}}(x)/dx$ if $|d\gamma_{\text{p}}/dx| \leq |d\gamma_{\text{e}}/dx|$. The expression in Eq. (5.2) is plotted in Fig. 5.8(b), using the simulated values for $g_{\text{e}}(h)$ and $g_{\text{om}}(h)$ (Fig. 5.8(a)), for given T_{d} . Note that in the limit of weak coupling ($1 - T_{\text{d}} \ll 1$), $\Gamma \gg 1$ is possible even when $g_{\text{e}} < g_{\text{om}}$. The experimentally observed Γ for the device under study approximately follows the red line in Fig. 5.8(b); both theoretical and experimental Γ cross from the dispersive to the dissipative regime ($\Gamma = 1$) for $h \sim 200\text{--}300$ nm. This is generally consistent with the transition observed in Fig. 5.6(b) as well as experimental observations in Figs. 5.5(b) and 5.6(a), in which measurements show the prominence of dispersive coupling

when the fiber is touching and dissipative when hovering. The respective values of Γ for the hovering configurations (upper plots in Fig. 5.6) indicate that h was larger for the M1 measurement than for M2: when the taper is not stabilized through contact with the device, a slow drift in h of $\sim \pm 50$ nm can occur despite the stage positions being fixed. Disagreement between simulated and measured $\Gamma(h)$ for $h < 200$ nm is ascribed to the non-idealities described above, including fluctuating taper position and λ_o , resulting in poor estimates of g_e and g_{om} . However, the key features in Fig. 5.8, notably that $\Lambda_e > \Lambda_{om}$, and that $\Gamma = 1$ when $h \sim 300$ nm, are not found to be significantly affected by these uncertainties.

The dramatic increase in Γ with h is promising from an optomechanical cooling standpoint, especially for systems in the sideband-unresolved regime [125, 127, 128, 130, 131]. Discussions of optomechanical cooling in systems exhibiting both dispersive and dissipative coupling [125, 128] are typically expressed in terms of the normalized coupling coefficients $\tilde{A} = \frac{-1}{\gamma_t} \frac{d\omega_o}{dx} x_{zpf}$ and $\tilde{B} = \frac{1}{\gamma_t} \frac{d\gamma_e}{dx} x_{zpf}$, where x_{zpf} is the amplitude of the zero-point fluctuations of the mechanical oscillator. The ratio $\tilde{B}/\tilde{A} = -g_e/g_{om}$ determines the optimal detuning required to minimize phonon occupation. For a given \tilde{B}/\tilde{A} and detuning, the maximum achievable optomechanical cooling rate $\gamma_{BA,opt}$, which in turn determines the minimum achievable phonon number, scales with $n\tilde{B}^2$, where n is the intracavity photon number [125], indicating that operating in a regime of large \tilde{B} is desirable in order to minimize phonon number in a dissipatively cooled system. In contrast to Γ , $\tilde{B}/\tilde{A} < 1$ for the h range considered here (inset to Fig. 5.8(b)), limiting the effectiveness of dissipative cooling. However, further enhancement of the dissipative coupling strength without introducing additional parasitic loss, for example through stronger fiber–nanocavity coupling γ_e via phase-matching considerations [105], would improve the tunability of the optomechanical coupling behavior described in this paper and help achieve dissipative cooling ($\gamma_{BA,opt} \propto n\tilde{B}^2$) of the C modes of this device. Given that $\tilde{B} \propto \frac{d\gamma_e}{dx} \frac{1}{\gamma_t}$, and assuming that the dissipative coupling scales as $d\gamma_e/dx \propto \gamma_e$, increasing \tilde{B} by enhancing γ_e is limited by the necessary condition that $\gamma_t \geq \gamma_e$.

For the device demonstrated here, $\gamma_e/\gamma_t \sim 1/40$, indicating that increasing \tilde{B} by over an order of magnitude through enhancement to γ_e is possible.

5.6 Perturbative approximations for dispersive and dissipative-external couplings

Note: this section is the result of efforts from my colleague, Dr. Hryciw.

To gain insight into the physical mechanisms governing the effect of the fiber taper on g_{om} and g_e , we evaluate the shift in cavity resonance frequency, ω_o , and coupling rate between the fiber and cavity, γ_e , using first-order perturbation theory.

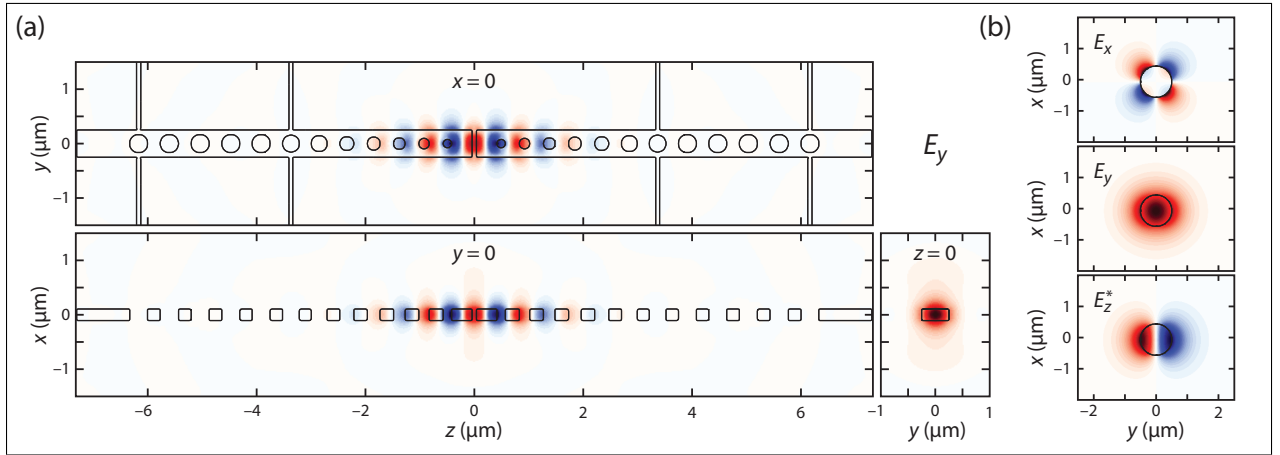


Figure 5.9: Unperturbed electric field profiles of the fundamental TE-like mode of (a) the split-beam cavity (E_y only) and (b) a 1- μm -diameter fiber

The unperturbed cavity field \mathbf{E}_c , the dominant y -component of which is shown in Fig. 5.9(a), was calculated using FDTD simulations [142] of the cavity geometry as determined from SEM images of the device. The dielectric profile of the cavity, $\epsilon_c(\mathbf{r})$, is assumed to have inversion symmetry; in particular, the circular hole radii and positions are specified to be symmetric with respect to the $z = 0$ plane. The fundamental TE-like cavity mode (E -field even in x , odd in y) has a resonance wavelength of $\sim 1,612$ nm, a quality factor of

1.2×10^4 (limited by scattering in the x and y directions), and an effective mode volume of $\sim 0.35 (\lambda/n)^3$.

The unperturbed fiber taper fields were calculated using a frequency-domain eigenmode solver [147], assuming a SiO_2 ($n_f = 1.44$) fiber with a diameter of $1 \mu\text{m}$ in air. This fiber supports a single TE-like mode at a wavelength of $1,612 \text{ nm}$, with a propagation constant $\beta = 4.5 \mu\text{m}^{-1}$.

Next, we calculate the change in cavity resonance frequency with fiber height h to estimate g_{om} using perturbation theory. The first-order correction to the resonant frequency of an electromagnetic cavity due to a change in permittivity may be calculated using [61]:

$$\Delta\omega_o = -\frac{\omega_o}{2} \frac{\langle \mathbf{E}_c | \Delta\epsilon_f | \mathbf{E}_c \rangle}{\langle \mathbf{E}_c | \epsilon_c | \mathbf{E}_c \rangle}, \quad (5.3)$$

where \mathbf{E}_c and ω_o are the unperturbed cavity electric field and resonant frequency, respectively, $\Delta\epsilon_f$ is the perturbation of the local dielectric environment due to the fiber, and $\langle \rangle$ represents integration over all space. For the geometry considered in this paper, $\Delta\epsilon_f = \epsilon_f - 1$, with the integral restricted to the region inside the fiber taper. As in the finite-element calculations in Fig. 5.8(a), we model a dimpled fiber with a $25 \mu\text{m}$ radius of curvature (see inset to Fig. 5.10).

From this expression, we see that the change in the cavity resonant frequency with h scales with the intensity of the evanescent cavity field overlapping with the fiber. For a cantilever mode, $dx \equiv -dh$, such that $g_{\text{om}} \sim -\frac{d\Delta\omega_o}{dh}$ decays with the same quasi-exponential dependence. Fig. 5.10 plots g_{om} using this approach for the dimple centered on the cavity ($z_f = 0 \mu\text{m}$) and offset axially over one of the mirrors ($z_f = -2 \mu\text{m}$); the latter agrees well with g_{om} calculated using FEA for the full fiber-cavity system, as shown in Fig. 5.8(a).

An approximation for the cavity loss rate into the fiber, γ_e , can be obtained from coupling-mode analysis for a generalized waveguide-resonator system [145]. Neglecting dispersion, the loss rate into either the forward- or backward-propagating fiber mode is

$$\gamma_e = \left| \frac{\omega\epsilon_0}{4} \int_{z_1}^{z_2} dz \iint dx dy (\epsilon_c - 1) \mathbf{E}_c^* \cdot \mathbf{E}_f e^{-i\beta z} \right|^2, \quad (5.4)$$

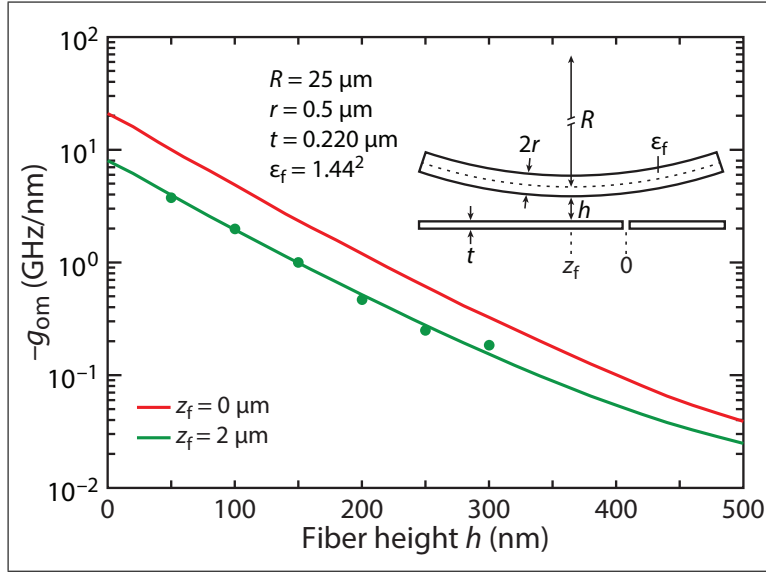


Figure 5.10: Dispersive coupling coefficient g_{om} calculated using first-order perturbation theory; the simulation geometry is shown in the inset. The red (green) line corresponds to an axial fiber offset z_f of 0 (-2) μm from the cavity center. The green circles are the $g_{\text{om},\text{M1}}$ values from Fig. 5.8(a), calculated using FEA.

where ϵ_c is the relative permittivity of the cavity, $\mathbf{E}_c(x, y, z)$ is the unperturbed cavity electric field distribution (normalized to unit energy), $\mathbf{E}_f(x, y)$ is the unperturbed fiber electric field mode profile (normalized to unit power), β is the fiber mode propagation constant, and the integrals in x and y are restricted to the region inside the cavity dielectric. As a simple approximation for the effect of the dimple curvature, we assume a straight fiber at a distance h above the cavity and integrate over an effective coupling length Δz centered at z_f (i.e., $z_1 = z_f - \frac{\Delta z}{2}$, $z_2 = z_f + \frac{\Delta z}{2}$). Assuming $dx > 0$ corresponds to deflection of the cantilever toward the fiber, then for a fiber-cavity separation h , we then have $g_e \sim -\frac{d\gamma_e}{dh}$. Fig. 5.11(a) plots g_e calculated via this approach for dimple center positions z_f of 0 and -2 μm .

Note that g_e calculated using this approach does not take into account contributions from coupling to higher-order fiber modes that are converted to the fundamental mode, which may in part explains its lower magnitude with respect to the calculation shown in Fig. 5.8(a). Although this treatment is approximate, it captures several features of the full FEA

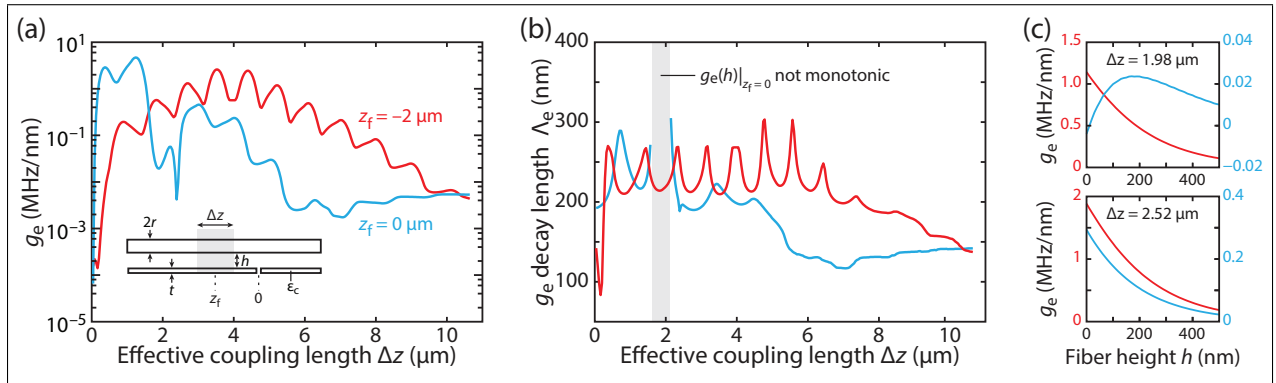


Figure 5.11: Dissipative coupling coefficient g_e calculated from mode-coupling theory for a fiber height of 200 nm; the simulation geometry is shown in the inset to (a), where the grey box denotes the integration limits on z . In all cases, blue (red) corresponds to a z_f of 0 (-2) μm . (a) g_e as a function of effective coupling length. (b) Decay lengths obtained from single-exponential fits of $g_e(h)$. (c) g_e vs. h for coupling lengths of 1.98 μm (top) and 2.52 μm (bottom).

approach, including non-monotonic behavior of $g_e(h)$ with $z_f = 0 \mu\text{m}$ for certain coupling lengths (Fig. 5.11(c), top), and sensitivity of the magnitude of g_e (Fig. 5.11(a)) and its decay length Λ_e (Fig. 5.11(b)) to dimple position z_f . The richer physics of this coupling mechanism compared with g_{om} may be traced to its origin as an interference effect, which does not enter into the dispersive coupling calculation.

5.7 Dissipative – dispersive coupling transition via axial fiber motion

As demonstrated so far, the presence of the fiber affects both the strength and the dispersive versus dissipative character of the optomechanical signal. With the fiber taper dimple aligned with the center of the device, a transition from predominantly dissipative to dispersive coupling is observed as the fiber moves vertically toward the nanobeam, as illustrated in Fig. 5.6(b). A complementary measurement further demonstrating this effect is to monitor the optomechanical signal while moving the dimple along the nanobeam axis (z direction).

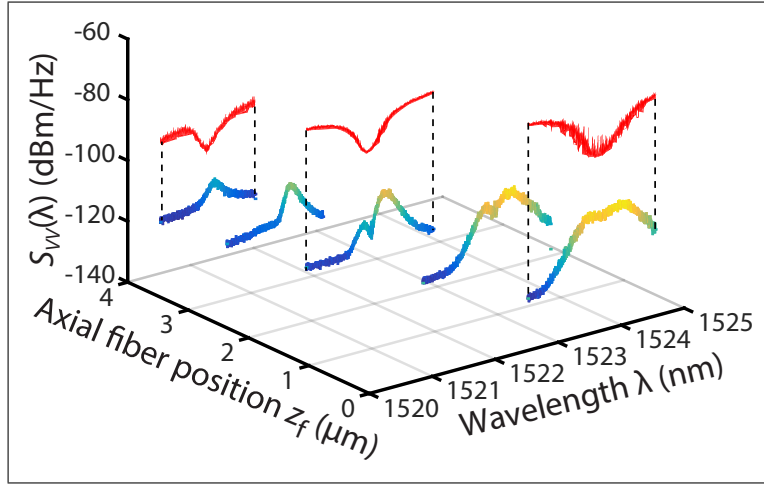


Figure 5.12: S_{VV} vs. λ for varying axial fiber positions z_f along the nanobeam. The fiber is hovering about $h = 100$ nm above M2. At $z = 0$, the fiber dimple is directly above the center of the cavity. $T(\lambda)$ in red is shown for selected heights.

When the fiber taper is far from the center of the cavity, shown on the left in Fig. 5.12, the optomechanical coupling is strongly dissipative in nature. As the fiber moves toward the central gap where the field is concentrated, its influence increases and g_{om} becomes dominant by $z_f = 2 \mu\text{m}$. However, at very close proximity to the center of the cavity ($z_f \leq 1 \mu\text{m}$), both the optical resonance and the optomechanical signal become unstable due to the near-field disturbance of the fiber. This is evident in the noisy nature of the fiber taper transmission, and the low visibility of the “zero” in the optomechanical response.

5.8 Summary and implications

In summary, we have demonstrated that renormalization of the near field of a photonic crystal nanocavity can be used to induce optomechanical coupling. Tuning of the coupling is mediated through evanescent interaction between the nanocavity formed between two cantilevers and a fiber taper near-field probe which induces both dispersive and dissipative optomechanical couplings. We showed that these effects can result in optomechanical cou-

plings close to $g_{\text{om}} \sim 1$ GHz/nm experimentally and potentially exceeding several GHz/nm in theory while g_e can reach 10 MHz/nm. The translational flexibility of the fiber taper gives us the ability to tune the ratio of dissipative-to-dispersive coupling. These enable measurement of mechanical cantilever modes which otherwise have zero optomechanical coupling. Furthermore, the features studied here allow spatially selective optical readout of mechanical resonances, providing information describing their spatial localization.

Taken together, these effects have the potential to extend the range of device geometries used for optomechanics-based sensing applications, including out-of-plane cantilever modes used in atomic force microscopy and magnetometry applications [58]. These experiments provide further opportunities for utilizing dissipative coupling to manipulate optomechanical systems [148] with potential implications for quantum optomechanics as discussed in chapter 4.

Chapter 6

Torque magnetometry

This final chapter covers work done under the collaborative project with the research group of Dr. Freeman which was published in Nature Nanotechnology in October, 2016 [149]. The fruits of this collaboration are manifold. An exchange of expertise and knowledge allowed melding of the fields of optomechanics and micromagnetism. The first section of this chapter is a brief summary of micromagnetic theory that will help understand the concepts described in the experiment. A new laboratory space and measurement setup at NINT now incorporates both a fiber taper and magnetic fields. Most importantly, an optomechanical device was successfully employed for torque magnetometry measurements with high sensitivity in ambient conditions. These measurements include probing the magnetization and susceptibility responses under applied fields of a micron-sized permalloy island as well as measuring its fine magnetic structure exhibited by Barkhausen steps or peaks.

6.1 Micromagnetic theory

Micromagnetism deals with the fundamental physics of magnetic phenomena at the micrometer scale where the effect of individual atoms can be averaged but the size of the sample plays an important role in its magnetic behaviour. Here we describe the various forces or energies that interact at that scale in permalloy thin films followed by magnetic effects resulting from their interactions and observed in this work [24, 150].

Micromagnetic energies

1. Exchange energy

The exchange energy is a quantum mechanical phenomena that includes Coulomb interac-

tion and Pauli exclusion principle. It is a short-range interaction between two nearby atoms. The spins of an unpaired electron in each atom will align in the same direction as they repel each other and move further apart, forming a stable and lower energy configuration. This results in spin continuity within a short distance where spins tend to be mostly aligned with their neighbors. In magnetic materials, this energy is much stronger than dipole-dipole interactions.

2. Magnetostatic energy (or demagnetization energy)

Magnetostatic energy is a self-induced energy caused by the interaction of the magnetization of one part of the sample with another part. A long-range interaction, it is measured by the magnetic field extending outside the sample. To reduce this energy, the spins on the edge of the sample can align parallel to it while spins located further inside will overall tend to misalign from each other. Therefore, this interaction is shape-dependent and is responsible for domain formation (see below).

3. Zeeman energy

This is the main energy exploited for torque magnetometry. The interaction between the magnetization of the sample and the external field causes spin to align with the applied field.

Total energy and torque

All the energies will contribute together to form an effective field \mathbf{H}_{eff} (derivative as a function of \mathbf{M}) which will dictate the magnetization direction and strength of the particular spin. A torque is exerted on the electrons to align their spin with the magnetization direction. Conservation of angular momentum dictates a reactive torque which pushes groups of spin to flip. This is the origin of domain wall movement or distortion (see below). The coupling of the spin to the crystal lattice finally creates a mechanical torque to the surrounding

material. The definitive mechanism behind magneto-mechanics or spin mechanics remains complex [5, 17, 151–153].

Note that many other energies may play a role in magnetic materials such as magnetocrystalline anisotropy energy and magnetoelastic energy. The first originates from crystal symmetry combined with spin-orbital coupling which creates certain axes where the magnetization prefers to align (easy axis). The latter creates local lattice distortions or strains induced by the direction of the magnetization and is the mechanism behind magnetostriction. Thin films of polycrystalline permalloy have negligible magnetocrystalline anisotropy and magnetostriction thus these two energies will be neglected in this work.

Landau-Lifshitz-Gilbert equation

The Landau-Lifshitz-Gilbert (LLG) equation is the equation of motion for micromagnetics. It describes the interaction between the magnetic moment and an externally applied field:

$$\frac{d\mathbf{M}}{dt} = -\gamma\mu_0(\mathbf{M} \times \mathbf{H}_{\text{eff}}) + \frac{\alpha}{M_S} \left(\mathbf{M} \times \frac{d\mathbf{M}}{dt} \right) \quad (6.1)$$

where α is the phenomenological Gilbert damping parameter, γ is the gyromagnetic ratio, and M_S is the magnetization saturation. The first term creates a torque which causes the magnetization to precess. The second term is a damping term.

The LLG equation can be solved spatially and in time using FEA or FDTD numerical methods.

Magnetic domains and walls

Magnetic domains are regions in the magnetic sample where magnetic moments are aligned and pointing in the same direction (as in Fig. 6.1(a)). The formation of domains is due to the minimization of magnetostatic energy. Domain walls are regions separating the individual

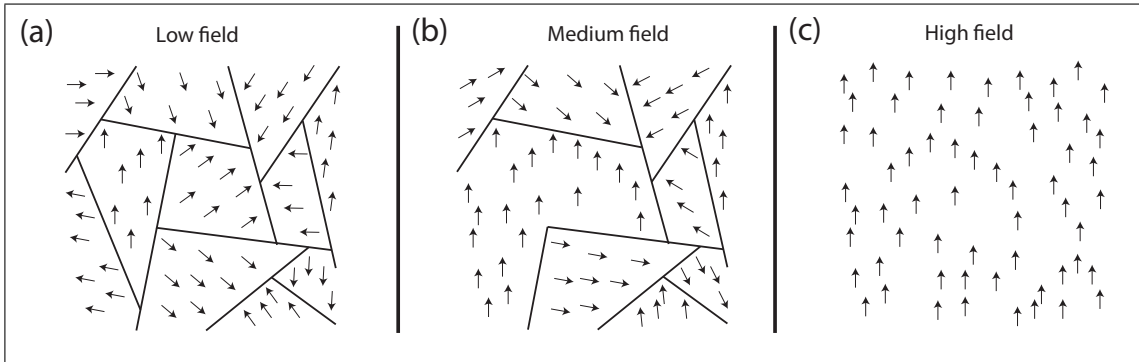


Figure 6.1: Schematic of magnetic domains (section with arrows pointing in the same direction) and walls (lines) under (a) low, (b) medium, and (c) high applied fields.

domains and are represented by lines in Fig. 6.1. When an external magnetic field is applied, domains can move or distort as the Zeeman energy causes moments to align to the field (Fig. 6.1(b)). If a strong enough field is applied, all moments in a sample might point toward the direction of the field and the sample reaches saturation (as shown in Fig. 6.1(c)).

Magnetic vortex state

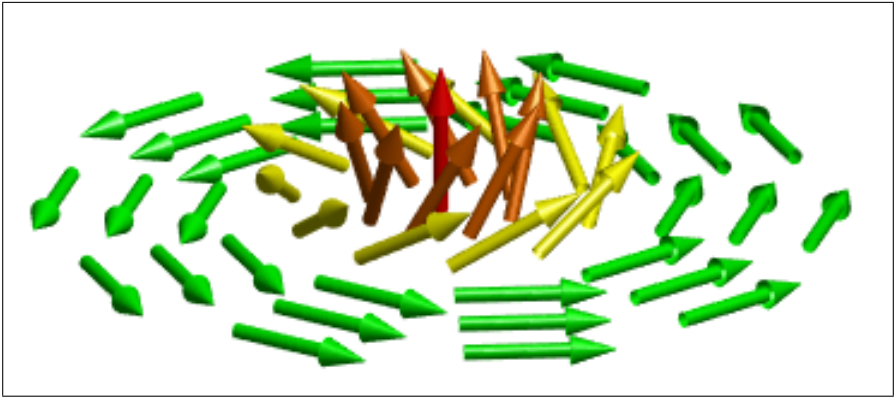


Figure 6.2: Schematic of a magnetic vortex state where the spins represented by the arrows align in a circular fashion.

A magnetic vortex state is a configuration of magnetic moments where spins align in a circular fashion as illustrated in Fig. 6.2. This micromagnetic ordering allows for minimal

magnetostatic energy at the expense of exchange energy. The spins near the “eye” of the vortex, collectively called the “core”, attempt to reduce their exchange energies by remaining as parallel to their neighbors as possible. However, this forces the central spins to point upward or downward depending on the chirality (direction of rotation) of the vortex. The width of the core can be as small as a few tens of nanometers.

Magnetic pinning site and Barkhausen steps

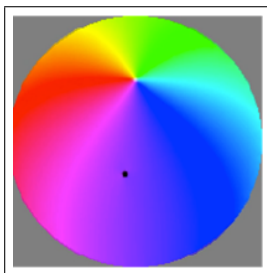


Figure 6.3: Micromagnetic simulation of a toy model for a pinning site using a vacancy in the simulation grid as represented by the black dot. Picture graciously provided by Fatemeh Fani Sani [154].

A pinning site is a physical defect or imperfection on a thin film of magnetic material such as a nanoscale dislocation in the crystalline lattice, surface roughness, or grain boundaries. When a magnetic domain moves through a pinning site due to increased applied field, its wall can remain caught until it separates from the site. The sudden switch of a small ensemble of spins is observed as a small jump in the magnetization signal and is called Barkhausen noise [155]. As for a magnetic vortex configuration, the vortex moving close to a pinning site can suddenly be “pinned” (stuck to the defect) until “depinning” occurs at which point a Barkhausen step is measured. The location of defects on a sample cannot be reproduced exactly by micromagnetic simulations but its effects can be studied using artificial methods such as randomly generated domains or a vacancy in the simulation grid as shown in Fig.

6.3 [154].

6.2 Torque magnetometry: experimental preparation

Nanofabrication with permalloy

Current fabrication capabilities have vastly improved, including the ability to deposit a single atomic layer in a uniform film. For magnetic materials, thin films have relied on the traditional molecular beam epitaxy and sputtering machines. These are joined by many modern techniques including electrodeposition, evaporation, self-assembly, and others. After deposition, the thin film can be patterned using lithography, carved using a focused ion beam, or stamped using microprinting techniques [18].

Permalloy, the magnetic material used in this work, is a soft ferromagnetic alloy made from 80% nickel and 20% iron. Invented by Bell Labs back in 1914, it is known for its high magnetic permeability (higher than steel), making it easy to magnetize under applied magnetic field. Its other magnetic properties include low coercivity (easy to demagnetize) and almost no magnetostriction (in contrast to Terfenol-D [52]). Its lack of ductility makes the material sometimes hard to work with. However, the low magnetostrictive properties and the softness of the material eases deposition and fabrication into nanomechanical resonators. Industrial applications of permalloy include electrical equipment as a magnetic core as well as magnetic shielding.

Fabrication process

The fabrication of optomechanical devices with magnetometry capabilities continues after the first process described in section 3.3. The second cycle of fabrication involves critical deposition and lift-off processes of the permalloy material ($\text{Ni}_{80}\text{Fe}_{20}$) on top of undercut devices [156]. The steps are shown in Fig. 6.4 and described below with more practical details found in appendix D.

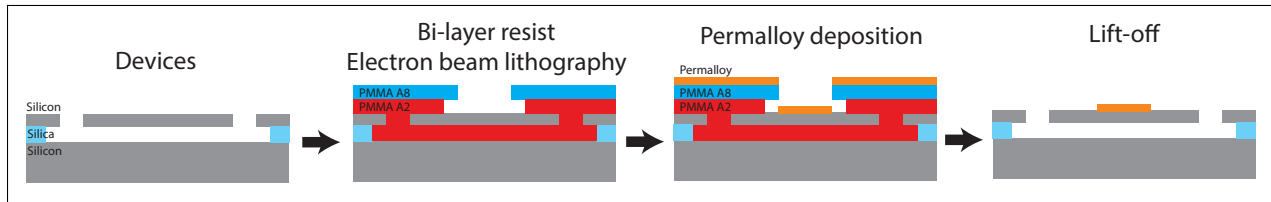


Figure 6.4: Second cycle of fabrication including bi-layer resist deposition, permalloy deposition, and lift-off.

1. Cleaning

The fabricated optomechanical devices fabricated in silicon earlier were cleaned using a piranha process.

2. Resist deposition

For the lithography process, a decision was made to deposit a PMMA bi-layer to ensure a thick resist and also detachment of the permalloy from the walls of the resist. First, PMMA A2 495k was spun on the chip. After baking, a layer of PMMA A8 950k was laid on top. The resist is expected to flow inside the undercut trenches below the device.

3. Electron beam lithography for second layer

This second lithography step will define the shape and location of the permalloy on the optomechanical device. The alignment between this second layer and the device is crucial, and is facilitated by alignment markers previously defined. After a pass through the electron beam lithography tool, the resist is developed in a MIBK mixture.

4. Permalloy deposition

A thin film of permalloy is deposited using a collimated electron beam evaporator inside a ultra-high vacuum chamber located in the laboratory of Dr. Freeman. Details of the permal-

loy deposition tool and process can be found in the appendix D.

5. Lift-off

During deposition, permalloy material that landed in the lithographically defined shapes should be directly on top of the optomechanical device. The rest of the magnetic material lays on the resist which is stripped away during this lift-off process. A bath of Remover-PG was used to dissolve the resist, leaving the patterned shape of permalloy on the silicon.

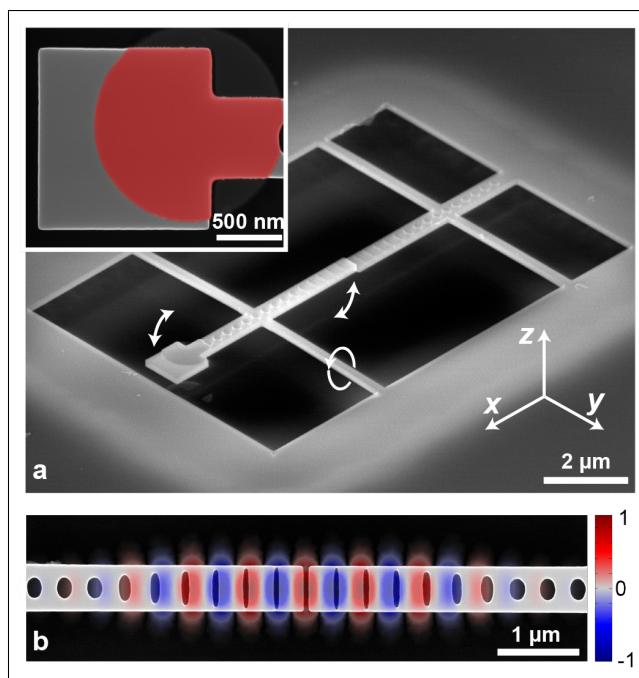


Figure 6.5: (a) Tilted scanning electron micrograph (SEM) of a split-beam cavity optomechanical torque sensor supporting a 40 nm thick permalloy island (highlighted in red in the inset). (b) Top-view SEM of the nanocavity overlaid with a finite element simulation (COMSOL) of the normalized field distribution E_y of its optical mode.

The final SBC device design consists of two suspended silicon photonic crystal nanobeams – one anchored in three sections, and the other “moving nanobeam” anchored by two supports. Vibrations of nanobeam mechanical resonances modulate both the gap width and the distance between the SBC and the fiber taper waveguide used to evanescently couple light

into and out of the nanocavity. Of particular interest for torque magnetometry is the torsional resonance T_y of the moving nanobeam, where the nanobeam ends move anti-symmetrically out-of-plane as shown schematically in Fig. 6.5(a). This mechanical mode can be efficiently excited by nanoscale sources of torque coupled to the SBC such as the permalloy structure (thickness of 40 nm) patterned on top of the device. The vertical motion is more suitable to the measurement setup described further below combined with the in-plane direction of the magnetization \mathbf{m} of the permalloy film according to $\boldsymbol{\tau} = \mathbf{m} \times \mu_0 \mathbf{H}$. The pad of area $1.4 \times 1.3 \mu\text{m}^2$ is partially covered with permalloy due to imperfect lithographic alignment during the lift-off process, resulting in the “mushroom” shape of the island. Because polycrystalline permalloy is optically absorbing, the permalloy island is positioned far from the nanocavity center, where it does not degrade Q_o by interacting directly with the nanocavity optical mode (overlaid in Fig. 6.5(b)).

Magnetometry measurement setup

To perform nanocavity-optomechanical torque magnetometry, the fiber taper setup for nanophotonic cavity optomechanics experiments described in chapter 3 was upgraded to support magnetometry capabilities as shown in the schematic in Fig. 6.6. A permanent magnet (N50 neodymium iron boron, 2.5 cm^3) was mounted on a motorized stepper rail and used to apply a stable and finely adjustable H_x^{DC} . The RF coil positioned beneath the sample chip was used for generating H_z^{RF} and H_x^{RF} . As before, the detection of the nanobeam motion was made through a dimpled optical fiber taper. The optical transmission of a tunable laser (Santec TSL-510, wavelength range 1,500 nm to 1,630 nm) source through the fiber taper was detected using a low-noise photodetector (New Focus 1811) and analyzed using a real-time spectrum analyzer (Tektronix RSA 5103B) and lock-in amplifier (Zurich Instruments HF2LI). For driving the RF coil, a reference tone was passed from the lock-in amplifier through an RF power amplifier (ENI 403L, 37 dB gain). All measurements were conducted at ambient temperature and pressure within a nitrogen-purged environment (see Fig. 6.7).

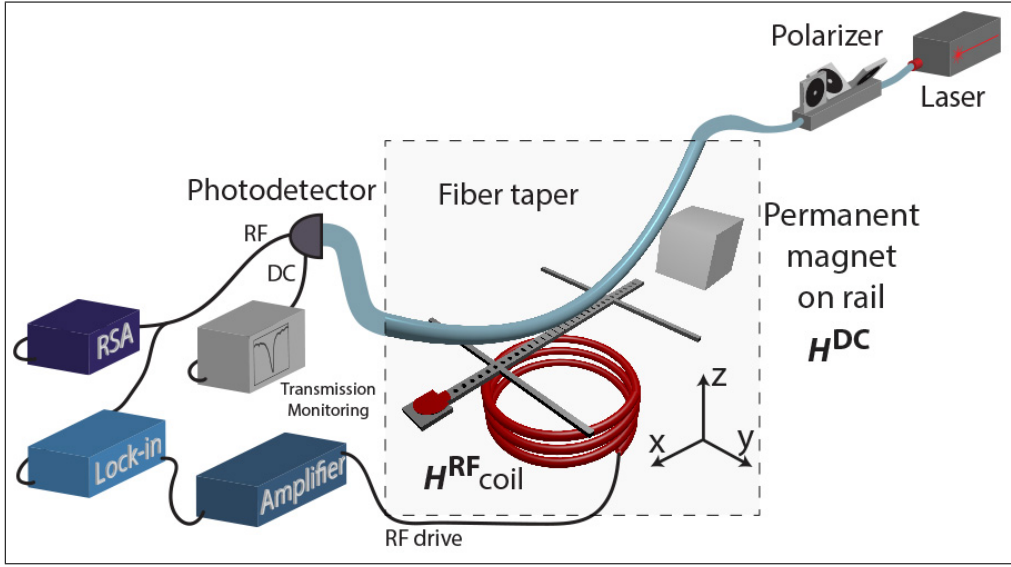


Figure 6.6: (a) Experimental setup for nanocavity optomechanical torque magnetometry measurements (not to scale). All measurements are performed in an ambient nitrogen purged environment (gray region). A dimpled fiber taper is used to probe the optomechanical nanocavity. A permanent magnet with adjustable position provides varying static magnetic fields. The lock-in amplifier reference is power amplified and sent to coils below the device to create an RF magnetic field in the \hat{z} -direction.

Application and calibration of RF and DC magnetic fields

A permanent magnet on an adjustable stepper rail is used to create a DC magnetic field H_x^{DC} aligned along the device \hat{x} axis. The 1-inch neodymium cubic magnet has a field magnitude of 760 G at a distance of about 2.5 cm from the torque sensors. This is sufficient for near complete saturation of the moments in the soft magnetic system studied in this work. The attachment of the fiber taper coming from above the sample is currently limiting the proximity of the magnet.

The implementation of permanent magnets is less common for variable magnetic field generation in magnetometry compared to the use of electromagnets, though the former offers advantages. Permanent magnets provide high and homogeneous fields over small regions, where the field stability is limited mainly by the resolution of the stepper motor used to vary the applied field. The very fine field resolution allows for direct correlation of events

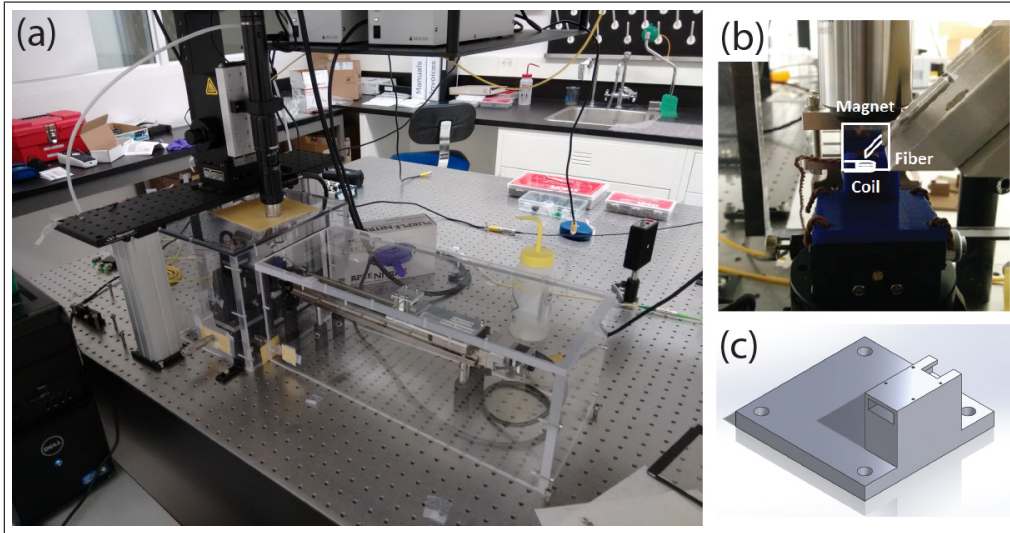


Figure 6.7: Pictures of our magnetometry measurement setup in our NINT laboratory. (a) The nitrogen box has been expanded to fit a rail for the permanent magnet compared to the original version at the University of Calgary. (b) Close-up of the probes surrounding the device under study. A coil is placed under the sample while a fiber taper probes the optical cavity from above. A microscope objective above is used to image the device for proper alignment with the fiber. The permanent magnet (white box) attached to a stepper rail is located behind the sample. (c) Design of the sample holder with openings carved for placement of the coil. The holder was fabricated using a 3D printer and a type of plastic called polylactic acid.

from multiple measurements (and are not prone to thermal drift as in electromagnets). The measurement setup is also greatly simplified, as using permanent magnets does not require a high power supply and cooling system as needed with electromagnets.

In addition to H_x^{DC} , DC field H_z^{DC} aligned along \hat{z} is created by introducing a small tilt ($\theta = 8^\circ$) of the sample with respect to horizontal. This allows generation of a torque proportional to the susceptibility χ_x (see experiment in section 6.3). The vector DC magnetic field in the frame of reference of the sample was calibrated with a 3-axis Hall probe (Sentron 3M12-2) placed at the sample location when the sample was removed. The magnetic field values were then measured as a function of magnet position on the stepper rail, and fit to a polynomial function. The fields were monitored during the measurements with the Hall probe sitting just below the sample, but the stepper position and a calibration procedure

are used for more accurate values of the applied field strength.

The RF magnetic fields generated by the coil were measured indirectly through the use of a current probe inserted between the output of the RF power amplifier (ENI Model 403L) and the coil. The maximum RF drive amplitude was $H_z^{\text{RF}} = 35$ A/m at 3 MHz, limited by harmonic distortion of the power amplifier. In laying out the cabling for the measurement, it is necessary to adjust the arrangement to minimize RF crosstalk from the drive to the photoreceiver.

The coil used in our measurements has 3 turns of 0.49 mm diameter wire wound to have an inner diameter of 3.4 mm. Using the measured RF current, the corresponding RMS magnetic field values were determined using Eq. (6.2) describing the on-axis field of a finite solenoid [157],

$$H_z^{\text{RF}} = \frac{IN}{2L(r_o - r_i)} \left[z_2 \ln \left(\frac{\sqrt{r_o^2 + z_2^2} + r_o}{\sqrt{r_i^2 + z_2^2} + r_i} \right) - z_1 \ln \left(\frac{\sqrt{r_o^2 + z_1^2} + r_o}{\sqrt{r_i^2 + z_1^2} + r_i} \right) \right], \quad (6.2)$$

with I the RMS current, N the number of turns, and L , r_o , r_i the length, outer radius, and inner radius of the solenoid, respectively. z_1 is the vertical distance from the device to the top of the solenoid, and $z_2 = z_1 + L$.

Optimization of optomechanical signal

The high sensitivity of the nanocavity optomechanical device arises from a combination of large optomechanical coupling, large mechanical resonator susceptibility (low mass m_{eff} and high Q_m) and sharp optical cavity response (high Q_o). The SBC device, shown earlier in Fig. 6.5(a), is designed with these properties in mind on top of lessons learned throughout this work.

In experiments described in this chapter, detection of the vertical motion of the T_y resonance will rely on the dispersive optomechanical interaction between the SBC and the fiber taper. The dimple is positioned in contact with the top surface of the fixed nanobeam such

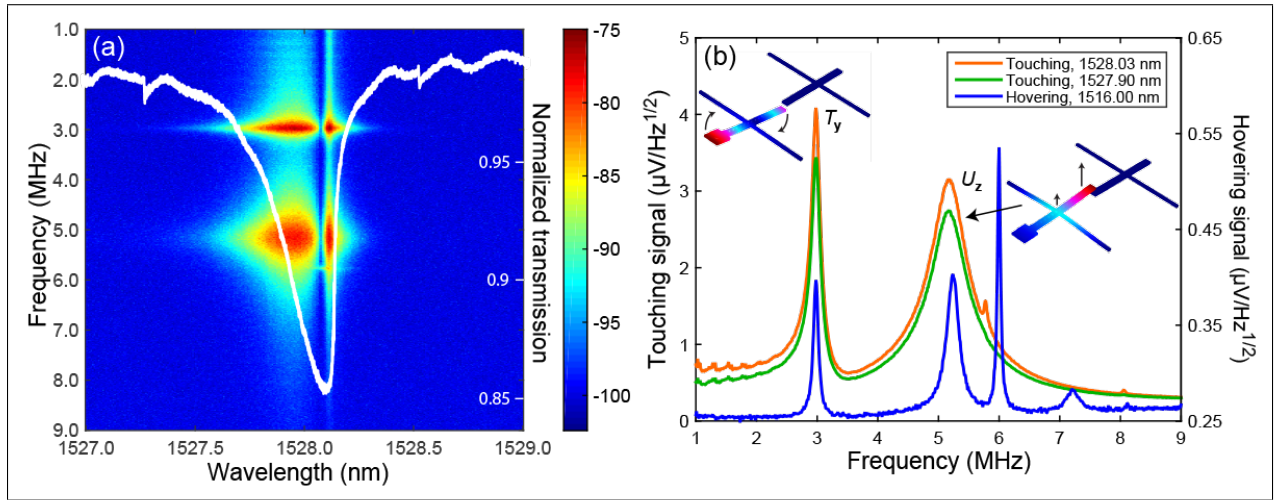


Figure 6.8: (a) Optomechanical response, $S_{VV}(\lambda, \omega)$, in ambient conditions as the fiber taper is touching the anchored nanocavity nanobeam. Scale bar on the right is in dBm. The white overlay with axis on the right is the optical transmission showing the optical resonance at 1,528 nm. Sharp low amplitude features are laser mode-hops. (b) Thermomechanical frequency response of the device at various wavelengths (left axis) and when hovering (right axis). Measurements were performed with no applied magnetic field ($H_z^{\text{RF}} = H_x^{\text{DC}} = 0$). Two mechanical modes of interest, T_y and U_z , are indicated, with their displacement fields predicted by finite element simulations inset. Black arrows indicate prominent displacement direction.

that, in the vicinity of the nanocavity gap region, the fiber taper is aligned < 200 nm from the device due to the curvature of the fiber. The fiber taper thus interacts with the near-field of the moving nanobeam without touching it. This provides stable fiber-nanocavity coupling without affecting the motion of the moving nanobeam, while also enhancing optomechanical coupling to the mechanical resonance of interest (see chapter 5). The fiber taper renormalizes the nominally symmetric nanocavity field and induces $g_{\text{om}}/2\pi$ up to 1.4 GHz/nm.

Figure 6.8 shows typical $T(\lambda)$ when probing an SBC optical mode at $\lambda_0 = 1,528$ nm with optical quality factor $Q_o \sim 5,000$. Note that the fiber taper input power, $P_i \sim 175 \mu\text{W}$, in this experiment is sufficiently large to introduce a slight thermal nonlinearity and associated non-Lorentzian optical response [107]. Optomechanically transduced motion of the moving nanobeam is probed by monitoring the fluctuations in $T(\lambda)$ detected by a photoreceiver

and a real-time spectrum analyzer (RSA). The RSA outputs an electronic power spectrum $S_{VV}(\lambda, \omega)$, as shown in Fig. 6.8a for λ swept from 1,527–1,529 nm across the optical mode of the device at $\lambda_o = 1,528$ nm. Peaks resulting from thermomechanical motion of the T_y and U_z nanomechanical resonances are observed at $\omega_m/2\pi = 3$ MHz and 5.3 MHz, respectively. Their frequencies closely match with predictions from finite element simulations (COMSOL).

Peaks in the observed bimodal λ dependence of $S_{VV}(\lambda, \omega_m)$ are approximately aligned with maxima in $|dT/d\lambda|$ near detunings $|\lambda - \lambda_o|$ equal to half an optical mode linewidth. This is a signature of predominantly dispersive optomechanical coupling present in the device for sideband unresolved operation ($\omega_m \ll \omega_o/Q_o$). Thus, for the measurements in this device, contributions from g_{om} dominate over both dissipative optomechanical couplings (see chapter 4).

At all times, λ is adjusted to maximize the optomechanical signal over noise. As shown in Fig. 6.8(b), by fixing λ on the red detuned shoulder of the optical resonance, a slightly stronger signal is obtained (orange trace). Although all main measurements are performed with the fiber taper in contact with the anchored nanobeam, it is also possible to transduce nanomechanical motion when the fiber is “hovering” above the device (shown in Fig. 6.8(b)). In these measurements the mechanical signal was found to be weaker and relatively unstable, as small fluctuations in fiber positioning would affect the coupling of light into the device (see chapter 5). Moreover, additional mechanical modes are present in the signal, as shown in Fig. 6.8(b), since the hovering fiber does not damp out resonances of the fixed nanobeam. Such hovering measurements are made at a shorter operating wavelength as the position of the fiber away from the cavity decreases the local effective index and λ_o .

6.3 Torque magnetometry measurements

Nanocavity torque magnetometry was performed by actuating the T_y mode with a magnetic field \mathbf{H} interacting with a magnetic moment \mathbf{m} on the nanobeam [158, 159]. Here we inves-

tigate the magnetic properties of the ferromagnetic thin-film permalloy island integrated on the rectangular pad at the end of the moving nanobeam, shown in the inset in Fig. 6.5(a). When an in-plane static field H_x^{DC} is applied, the permalloy becomes magnetized with net moment $m_x(H_x^{\text{DC}})$ along the field \hat{x} -direction. By applying an additional RF field H_z^{RF} directed in the out-of-plane \hat{z} -direction, a magnetic torque τ_y is generated proportional to m_x and directed along the torsion rod supporting the moving nanobeam. When the RF field is applied at the T_y resonance angular frequency ω_m , the resulting driven beam displacement can be detected optomechanically from the nanocavity optical response.

Sensitivity calibrations

The displacement sensitivity of the fiber-coupled SBC device can be calibrated by measuring the optomechanically transduced thermal motion without applied magnetic fields, as shown in Figs. 6.9(a) and (b), using the framework expounded in chapter 2 as well as the thermo-mechanical calibration procedure in Ref. [60]. For typical operating conditions, it is in the tens of $\text{fm}/\sqrt{\text{Hz}}$ range with an equivalent torque of $1.3 \times 10^{-20} \text{ Nm}/\sqrt{\text{Hz}}$. All measurements in this chapter are performed in ambient conditions, resulting in $Q_m < 100$ due to viscous air damping.

For the device studied here, Fig. 6.9(a) shows two overlapping peaks and thus the power spectral density can be fitted to an uncorrelated double Lorentzian curve with total noise floor $S_{\text{VV}}^{\text{noise}}(\omega)$:

$$S_{\text{VV}}(\omega) = S_{\text{VV}}^{\text{noise}}(\omega) + G_1^2 S_{\text{zz},1}^{\text{th}}(\omega) + G_2^2 S_{\text{zz},2}^{\text{th}}(\omega) \quad (6.3)$$

Here, $G_{1,2}$ correspond to the optomechanical gain introduced in chapter 2. The thermal displacement density $S_{\text{zz}}^{\text{th}}(\omega)$ of a particular resonance is given by the fluctuation-dissipation theorem as [72]:

$$S_{\text{zz}}^{\text{th}} = \frac{4k_B T_b \omega_m}{Q_m} \frac{1}{m_{\text{eff}}[(\omega^2 - \omega_m^2)^2 + (\frac{\omega \omega_m}{Q_m})^2]} \quad (6.4)$$

where k_B is Boltzmann's constant and T_b is the temperature of operation. After fitting Eq.

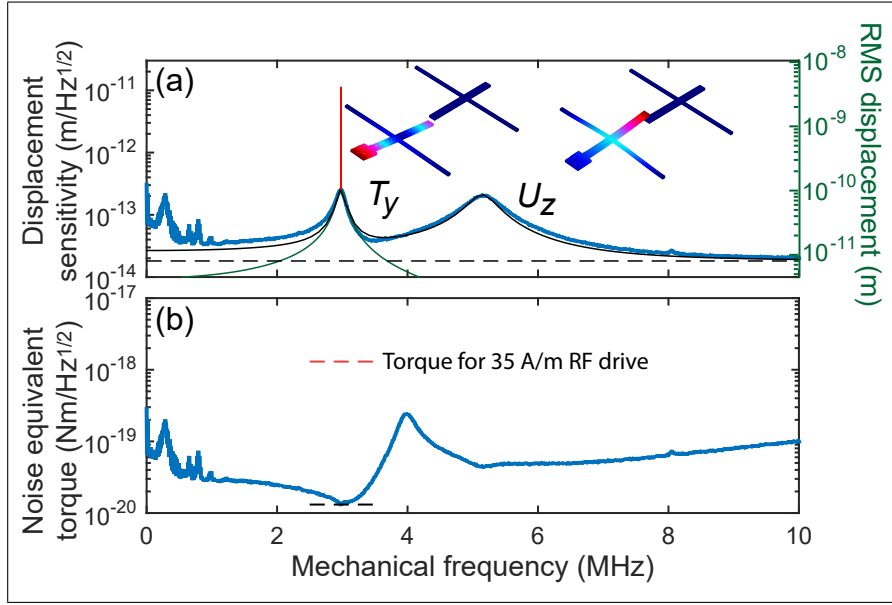


Figure 6.9: (a) Displacement density (left axis) from the real-time spectrum analyzer (RSA) showing thermally driven mechanical modes T_y and U_z (blue) and the magnetically driven signal (narrow peak highlighted in red) generated by a magnetic driving field H_z^{RF} of 35 A/m applied with the permalloy island magnetization saturated by $H_x^{\text{DC}} = 45$ kA/m. Black lines are fits to the T_y and U_z Lorentzian-shaped peaks (solid line) and the measurement noise floor (dashed line). The green curve (right axis) indicates the predicted RMS displacement of the T_y resonance in the presence of 35 A/m RF magnetic field as a function of frequency. Insets show simulated displacement profiles of T_y and U_z . (b) Torque equivalent noise of the thermomechanical displacement signal in (a). The red dotted line indicates the predicted torque in the presence of a 35 A/m H_z^{RF} field, and is labeled by the values on the left axis assuming a 1 s integration time.

(6.3) to the data with Q_m for each mode and $G_{1,2}$ as fitting parameters, the spectral response can be calibrated (i.e., converted from V^2/Hz to m^2/Hz) to a particular peak. In Fig. 6.9(a), the y -axis is calibrated such that the total displacement resolution of the torsional mode T_y is:

$$S_{zz,1}(\omega) = \frac{S_{\text{VV}}(\omega)}{G_1^2} = S_{zz,1}^{\text{th}}(\omega) + S_{zz}^{\text{noise}}(\omega) + \frac{G_2^2}{G_1^2} S_{zz,2}^{\text{th}}(\omega) \quad (6.5)$$

where $S_{zz}^{\text{noise}}(\omega) = S_{\text{VV}}^{\text{noise}}(\omega)/G_1^2$ gives the displacement sensitivity for T_y in this case. Its effective mass and torsional spring constant (relating displacement to force) is calculated to be $m_{\text{eff}} = 1$ pg and $k_{\text{eff}} = 4.6 \times 10^{-12}$ N m with an extracted $Q_m = 25$, limited by damping

from the N_2 operating environment.

From the displacement sensitivity, the equivalent torque sensitivity (plotted in Fig. 6.9(b)) can be found using $\mathbf{S}_\tau(\omega) = \mathbf{r}^2 \times S_{zz}(\omega)\hat{\mathbf{z}}/|\chi_m(\omega)|^2$ as we have shown in chapter 2. Here, \mathbf{r} corresponds to the distance between the axis of rotation formed by the supports on the moving beam and the tip of the pad (approximately $3.5 \mu\text{m}$). The mechanical susceptibility $\chi_m(\omega)$ from Eq. (2.2) relates the displacement density to the applied force, and the torque is calculated from $\boldsymbol{\tau} = \mathbf{r} \times \mathbf{F}$.

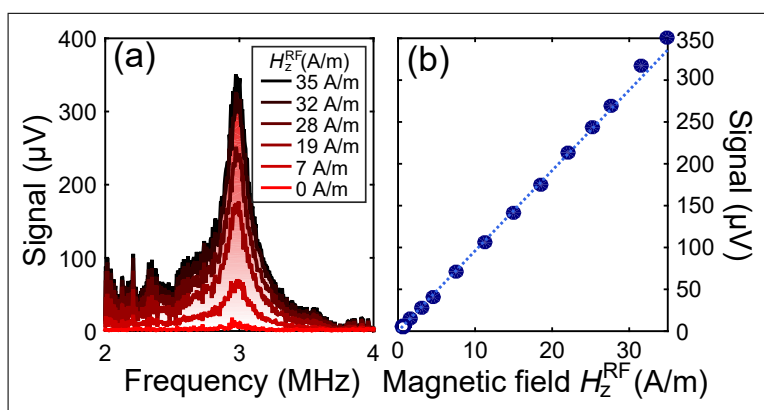


Figure 6.10: Magnetic moment sensitivity. (a) Device response as RF magnetic fields of various intensities are applied and swept from 2 to 4 MHz using the lock-in amplifier, for a constant DC field $H_x^{\text{DC}} = 45 \text{ kA/m}$. (b) Maximum device response (located at 3 MHz) vs applied RF field strength. When the applied field H_z^{RF} is turned off, the minimum signal is limited by thermomechanical noise leading to an effective minimum detectable field $H_{\text{min}} \sim 0.61 \text{ A/m}$ indicated by the open circle.

Our next calibration measurement consists in turning on and varying the RF drive field H_z^{RF} near the T_y resonance. The measured frequency response is shown in Fig. 6.10(a), with an applied bias field $H_x^{\text{DC}} = 45 \text{ kA/m}$ saturating the permalloy moment. When the drive angular frequency ω_{RF} is tuned onto resonance with ω_m of the T_y resonance, a sharp signal superimposed upon the broad thermomechanical peaks in the RSA spectrum is observed (see Fig. 6.9(a)), indicating that H_z^{RF} is actuating the nanobeam.

The device's magnetic moment sensitivity may be calculated from the observed linear relationship of the response of the device with RF drive shown in Fig. 6.10(b). At

$H_z^{\text{RF}} = 0$ A/m, the thermomechanical contribution limits the measurement sensitivity. For our particular device, this corresponds to an effective RF drive of $H_{\text{min}} = 0.61$ A/m, as indicated by the open circle. With the assumption that all magnetic moments contribute to driving the signal, the sensitivity is calculated to be $2.7 \times 10^9 \mu_B$ (A/m). This sensitivity under ambient conditions is on par with nanotorsional resonators using interferometric detection in vacuum [16, 160]. The corresponding torque sensitivity was calculated to be around 3.2×10^{-20} Nm, which was close to the thermally limited minimum torque sensitivity measured using the RSA. The slightly poorer sensitivity here is believed to be caused by additional technical noise due to RF pickup in the electronics, which can be alleviated with shielding.

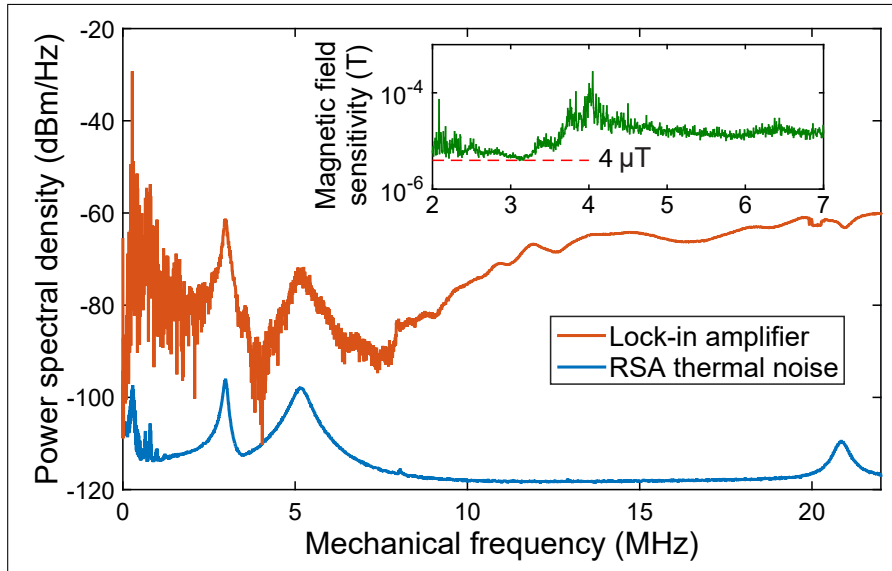


Figure 6.11: Wide bandwidth power spectral density of the nanocavity coupled optical signal. In blue, the RSA signal for $H_z^{\text{RF}} = 0$ shows the two main mechanical modes with secondary modes at 8 MHz and 21 MHz. In orange, the RF coil with $H_z^{\text{RF}} = 35$ A/m drives the device while the signal is recorded by the lock-in amplifier. An RF power amplifier was used (37 dB amplification, 150 kHz - 250 MHz range). Large noise at low frequency (< 1 MHz) is due to the fiber taper vibrations. At higher frequencies, the noise generated by the RF coil increases. Inset: Measured magnetic field sensitivity.

The broader bandwidth response ($\omega_{\text{RF}}/2\pi$ from 0 – 22 MHz) of the nanocavity with and

without driving field is plotted in Fig. 6.11. At $H_z^{\text{RF}} = 0$, the signal $S(\omega)$ is broadband with low noise. The mechanical mode at 21 MHz is a second-order torsional mode. With H_z^{RF} on, shown in red and denoted as $N(\omega)$, the lock-in amplifier is able to detect the two main driven mechanical resonances T_y and U_z . The torsional mode T_y produced the strongest response due to the favorable geometry for the orthogonality of magnetic torque terms; thus all torque measurements were performed at the frequency of T_y . The second mode responds weakly since its motional shape is less efficiently (about 50%) actuated by torque. The overall noise floor is also much higher due to technical noise coming from the current in the RF coil and cables. This accounts for the slightly worse torque sensitivity of 3.2×10^{-20} Nm measured with the lock-in amplifier.

Although the primary function of our device is not field sensing, its magnetic field sensitivity can be estimated from the spectral analysis following the procedure laid out in Ref. [51]. First, a reference signal is calibrated at a particular frequency shown as the peak in Fig. 6.9a where a field $H^{\text{RF}} = 35$ A/m or equivalently $B_{\text{ref}} = \mu_0 H^{\text{RF}} = 44$ μT was applied. The minimum detectable magnetic field can then be expressed as $B_{\text{min}}(\omega_{\text{ref}}) = B_{\text{ref}}/\sqrt{SNR \cdot RBW}$ where SNR is the signal to noise ratio of the reference peak. To map this to an overall spectral sensitivity, the spectral responses with and without applied field, $N(\omega)$ and $S(\omega)$ respectively, can be combined to obtain the graph in the inset of Fig. 6.11 using the following equation [51]:

$$B_{\text{min}}(\omega) = \sqrt{\frac{S(\omega)N(\omega_{\text{ref}})}{S(\omega_{\text{ref}})N(\omega)}} B_{\text{min}}(\omega_{\text{ref}}). \quad (6.6)$$

The highest sensitivity of 4 μT occurs near the mechanical resonance at 3 MHz. This relatively low field sensitivity is typical for a permalloy pad with small volume $V_{\text{py}} \sim 1 \mu\text{m}^2 \times 40$ nm compared to the orders of magnitude larger volumes of magnetic material used in other optomechanical or torsional systems [52, 161, 162].

Comparison with other technologies

Among torque magnetometers, the reported device has state-of-the-art sensitivity of 1.3×10^{-20} Nm/ $\sqrt{\text{Hz}}$, despite operating in ambient conditions where its mechanical resonances are significantly damped. Among optomechanical torque sensor devices not yet used for magnetometry, devices with better sensitivity have been demonstrated operating in vacuum and/or cryogenic conditions. For example, a see-saw double-photon-crystal nanobeam [55] reaches torque sensitivity of 9.6×10^{-21} Nm/ $\sqrt{\text{Hz}}$ in 10^{-4} Torr vacuum, and optomechanical devices in mK conditions have been measured with record 10^{-24} Nm/ $\sqrt{\text{Hz}}$ sensitivity [54]. However, none of these devices have yet been used for magnetometry or to probe other systems. Our devices can reach, if not surpass, those sensitivities in similar conditions, where Q_m is expected to increase by orders of magnitude owing to elimination of air damping in vacuum and reduction of internal damping in silicon at low temperatures [31].

Torque magnetometry is not in direct competition with existing methods, but offers a complementary magnetometry tool at the nanoscale. In comparison to most other magnetometry methods involving nanodevices our torque magnetometry method provides direct, non-invasive, and fast acquisition of the magnetostatic hysteresis loop while also being able to capture the associated RF susceptibility. Magnetic force [163] and diamond NV centre [164–175] magnetometry offer extremely high magnetic moment sensitivity for electron and nuclear spin resonance detection, and they are practically ideal for localized probing. However, experimental acquisition of the volumetric static moment of a micromagnetic element (and acquiring its hysteresis loop) would require lengthy imaging and reconstruction. This is further complicated if complex three-dimensional microstructures are to be measured (of which torque magnetometry is capable [23]).

A slightly faster scanning technique, the Scanning Electron Microscopy with Polarization Analysis (SEMPA), is less invasive since electrons are used to probe the magnetization of the sample [176]. Real-time (within the scanning speed of the SEM) and high resolution images

can be obtained using this method but measurements are fundamentally limited to surfaces only.

Micro-SQUID has also recently achieved single spin sensitivity [177], though their limited operating temperature does not allow for room-temperature measurement. Planar micro-Hall measurements that are sensitive to the perpendicular component of stray field offer room temperature sensitivities near that of nanoscale torque magnetometers, and have measured Barkhausen signatures associated with vortex core pinning in fabricated defect sites [178]. However, Johnson noise dominates and limits their detection sensitivity at high frequencies, and there have been no reports, to the knowledge of the our collaborative group, of RF susceptibility measurements associated with Barkhausen signatures in single nanoscale elements using the micro-Hall method.

Similar techniques using magnetoresistance for measuring spin transfer torques in metallic multilayers can only infer torque dynamics from measurements of resistance [153]. The same can be said for electrostatic detection using voltage readout [179]. However, the use of alternative information from measurement such as dissipation and mechanical frequency shift can reveal different vortex dynamics in superconducting crystals [180]

Recently, inductive methods for the sensitive measurement of magnetic resonance in single nanoscale elements have been developed [181, 182]. For inductive measurement of the irreversible magnetization changes at the static limit (DC), superconducting electronics would be required (see Ref. [183], section 4.7).

Micromagnetic simulations

Micromagnetic simulations were performed to visualize the magnetization amplitudes and states of the permalloy sample. Torque magnetometry is able to directly measure the net magnetization via the generated torque. However, this method does not give us direct imaging capabilities compared to other techniques. Therefore, numerical simulations were used to correlate our results by applying the Landau-Lifshitz-Gilbert equation for micromagnetism

on a MuMax 3.5 GPU-accelerated open-source software [184].

The parameters used are as follows: three dimensional grid size of 5 nm, saturation magnetization $M_S = 780$ kA/m and an exchange stiffness constant $A_{\text{ex}} = 13$ pJ/m. From the calibration of a similar permalloy film (under the same conditions), an experimental value of $M_S = 770$ kA/m was obtained. Since the calibrated film was not deposited at the same time as the permalloy pad under study here however, there is some uncertainty in the value of M_S . The Gilbert damping constant was set to $\alpha = 1$ to minimize the simulation time required for the quasi-static hysteresis. From the simulations, the net magnetization of the structure at an applied field of 45 kA/m was found to be $M = 0.965 M_S$, and this number was assumed also to be representative for the experiment.

Magnetization hysteresis curve

To perform magnetometry on the permalloy island, magnetic hysteresis loops were measured by varying H_x^{DC} via translation of the permanent magnet while recording the optomechanically transduced RF signal for fixed H_z^{RF} using the lock-in amplifier. Figure 6.12 shows the torque signal normalized to the value at saturation, with the corresponding scale for the net magnetization on the right axis. Beginning at high field (blue curve in Fig. 6.12), the magnetization was nearly saturated (section of the curve labeled A; the correspondingly lettered frames in the bottom section of Fig. 6.12 are representations of the spin textures from micromagnetic simulation). As the field decreases, three large discontinuities in the net moment inferred from the optomechanical signal are observed and correspond to irreversible changes in the spin texture, beginning with nucleation of a magnetic vortex with an out-of-plane core surrounded by in-plane curling magnetization (section B of the curve). As the DC field is further decreased, the vortex core translates towards the center of the element until an intermediate texture arises, featuring pronounced closure domains along the short edges perpendicular to the applied field (section C). The transition near zero field forms a two-vortex state, shown in frame D of Fig. 6.12, where the permalloy island's mushroom-like

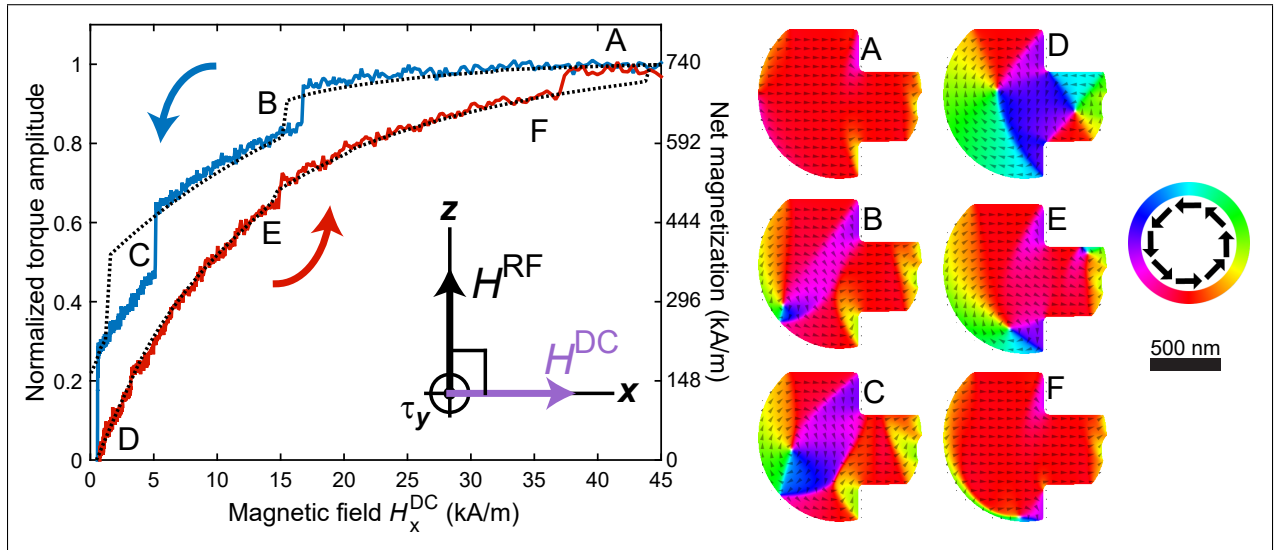


Figure 6.12: Hysteresis and magnetization response of the permalloy element with varying applied DC field along \hat{x} (5 runs averaged). The RF drive field is $H_z^{\text{RF}} = 35$ A/m. The solid blue trace is a decreasing field sweep and the solid red trace is an increasing field sweep. Results from micromagnetic simulations of the permalloy island (highlighted in red in the SEM inset in Fig. 6.5(a) and also used as the simulation mask) are plotted with black dashed lines. Bottom: simulated magnetization textures at different points in the hysteresis loop. The color wheel shows the in-plane direction of magnetization, with red parallel to the applied DC field.

shape supports a Landau state in the stem (right side) and a distorted circular vortex in the cap (left side) [185] in keeping with the demagnetizing energetic preference for the moments near edges to be nearly tangential to the boundaries. When H_x^{DC} is subsequently increased (red curve), the net moment increases monotonically with applied field. In section D of the simulation the two vortex cores move in opposite directions perpendicular to the field as the two circulations have opposite chiralities in this instance. The simulation frames E and F show the spin configurations just before each individual vortex core annihilates, after being pushed too close to the edge to remain stable by the field-increasing sweep. The simulated hysteresis loop (black dashed line) shows good qualitative agreement with observation, with the difference in the transition field values in part due to the simulations having been performed without including thermal energy.

Hysteresis of additional working devices

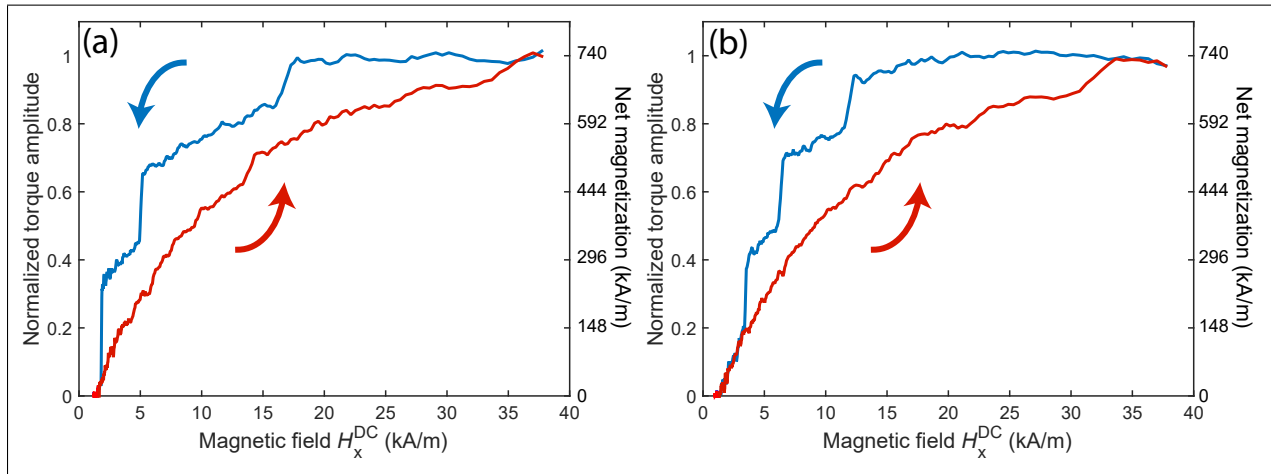


Figure 6.13: Magnetic hysteresis of neighbouring devices. Magnetic hysteresis measurements for devices fabricated immediately to the left (a) and right (b) on the same chip as the device studied in this chapter.

The data presented above was obtained from a single device that was observed to display the largest optomechanical magnetic transduction of those fabricated for this study. However, other devices were observed to display similar magnetic properties. The quality of the signal obtained from these devices was typically lower owing to poorer fiber coupling, lower Q_o , or larger misalignment of the permalloy pad with the nanobeam pad. These limitations are primarily a result of fluctuations in electron beam lithography dose during device fabrication.

Figure 6.13 shows low-resolution magnetic hysteresis measurements of the devices fabricated immediately to the left and right of the device studied throughout the text. The magnetization of these devices displays qualitatively similar jumps and hysteresis related to vortex formation. Note that these measurements are affected by larger than optimal drift in device relative position, as well as irregular magnetic field step size. These technical issues were reduced prior to the main measurements.

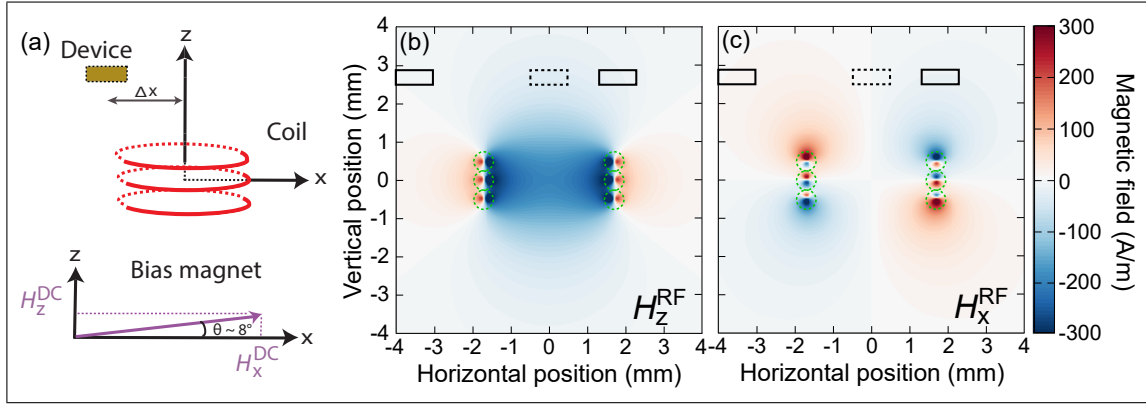


Figure 6.14: (a) Schematic of the positioning Δx of the device relative to the center of the coil (red) and tilt θ relative to the plane of the permanent magnet. RF magnetic field simulations of the coil (green dotted circles) for H_z^{RF} in (b) and H_x^{RF} in (c) at a current of 0.24 A. The approximate positions of the device for experiments in Figs. 6.15(a-c, e) are shown by the dashed boxes.

Susceptibility peaks

When the chip is centered ($\Delta x = 0$ mm, about 2 mm above coils), H_z^{RF} is at its strongest point while H_x^{RF} is approximately zero due to symmetry. For non-normal \mathbf{H}^{RF} , the nanocavity torque sensor can function as a susceptometer that probes RF magnetic susceptibility and provides new insight into the properties of the pinning processes. For these measurements, an in-plane \hat{x} -component of the RF field (parallel to the nominal DC field direction) is introduced by tuning the relative RF coil position off-centre to the device about $\Delta x = 1.9$ and -3.6 mm relative to the center of the coil as depicted in Fig. 6.14(a). Note that adjusting the relative chip-coil position is simplified experimentally by the ambient operating conditions and fiber-based readout.

In contrast to the on-axis case, there is no analytical formula for off-axis field values. The Biot-Savart law was used to calculate the magnetic field of a finite solenoid at an offset position near the coil by integrating over the current source. When the chip is offset to the right ($\Delta x = 1.9$ mm), it is found from Figs. 6.14(b) and (c)s that both x and z-components have comparable amplitudes such that $H_x^{\text{RF}} = H_z^{\text{RF}} = H^{\text{RF}}$. When offset to the left at

$\Delta x = -3.6$ mm, then $H_x^{\text{RF}} \approx -6H_z^{\text{RF}}$.

A small out-of-plane DC field H_z^{DC} combines with the oscillating field H_x^{RF} to generate torque in the \hat{y} -direction proportional to the in-plane susceptibility. Signals recorded using both \hat{z} and \hat{x} components of RF drive contain both torque contributions: from the net moment along \hat{x} ($\propto m_x^{\text{DC}} H_z^{\text{RF}}$) and from the RF susceptibility along \hat{x} ($\propto \chi_x^{\text{RF}} H_x^{\text{RF}} H_z^{\text{DC}}$), where χ is the magnetic susceptibility tensor of the permalloy island.

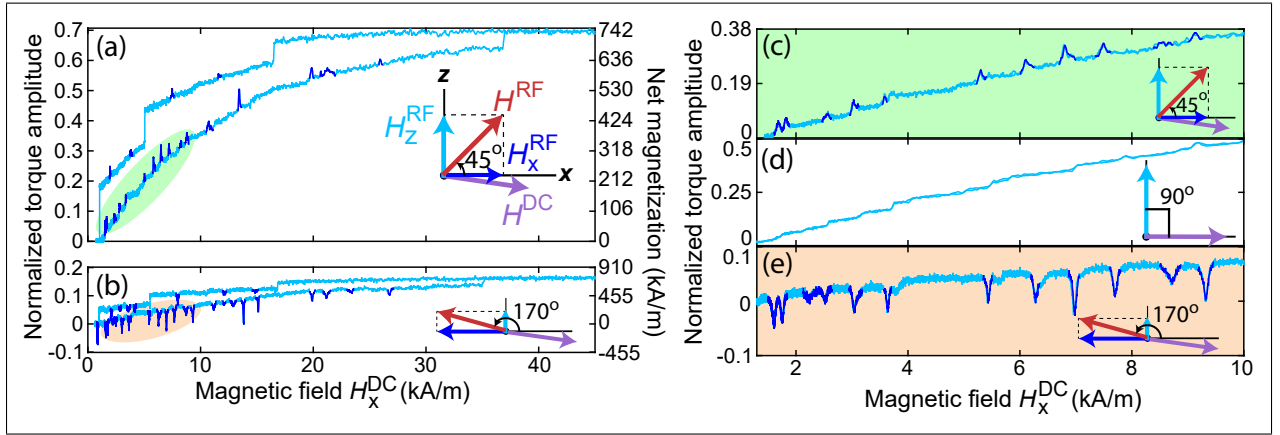


Figure 6.15: Enhanced room temperature magnetic susceptibility at Barkhausen steps. Hysteresis sweep with H^{RF} set to (a), 45° (equal and same sign x and z components) and (b), 170° (opposite sign x and z components). A select number of upward and downward peaks have been highlighted in blue to show contribution to torque from susceptibility. Low field H_x^{DC} single forward and backward sweeps at three H^{RF} positions: (c) 45° , (d) 90° , and (e) 170° . In all cases, the drive field $H^{\text{RF}} = 35$ A/m.

Figure 6.15 demonstrates the ability of the nanocavity optomechanical torque sensor to capture, in high resolution measurements, fine structure in the hysteresis that is the fingerprint of intrinsic disorder unique to a given permalloy island. These can not be predicted by the idealized micromagnetic simulations described above. The high energy density of vortex cores make them susceptible to pinning at defects in the polycrystalline island. With diameters on the order of ten nanometers, the cores finely probe the magnetic landscape as their positions change with applied field [21]. Pinning and depinning events are captured as Barkhausen steps, with notable reductions in slope of the hysteresis curve seen while cores

are pinned. Figure 6.15 shows a rich spectrum of repeatable events whose character varies depending on the orientation of \mathbf{H}^{RF} . Repeatable events for \mathbf{H}^{RF} perpendicular to the permalloy film (i.e., along \hat{z}) visible in section D of Fig. 6.12 are shown in close-up in Fig. 6.15(d). If the applied field is kept below the first vortex core annihilation field, curves like Fig. 6.15(d) show distinct steps without hysteresis when the field strength is ramped down. The absence of any minor hysteresis at each step is the result of very rapid (in comparison to the measurement bandwidth) thermally-activated hopping between neighboring pinning centers [21, 186], such that the apparatus records a temporal average weighted by the relative dwell times in the two sites.

Figures 6.15(a) and (b) show the full hysteresis loops for two different RF field orientations: 45° and 170° , respectively, anticlockwise from horizontal. The torque values remain normalized to the 90° orientation. Corresponding close-ups of the low-field sections are shown in Figs. 6.15(c) and (e), respectively. The peaks and dips newly found in the data are RF susceptibility signatures arising when the energy barrier between neighboring pinning sites is small enough that the in-plane RF field is able to drive the core synchronously back-and-forth. To the best of our knowledge, these measurements are the first report of RF susceptibility due to the Barkhausen effect at the single pinning event level, though averaged events have been studied previously [187]. Note that the larger transitions between spin textures in the main loop are irreversible and therefore exhibit no accompanying RF susceptibility features. The effective susceptibility $\delta\mathbf{m}/\delta\mathbf{H}$ (calculated in the following section) will be largest when the RF drive amplitude is just above the threshold required for a synchronous response, where the ratio of $\delta\mathbf{m}$ (set to first approximation by the moment change at the Barkhausen jump) to $\delta\mathbf{H}$ is largest. Observed enhancements of up to 25 times over the susceptibilities while the core is pinned suggest applications to RF susceptibility engineering in applications such as field-sensing magnetometry and detecting small volumes of magnetic material.

Both the ratios of amplitudes and the relative signs of the net moment and susceptibility contributions in Fig. 6.15 are consistent with the changes of the RF field direction. Implementation of a scheme with independent control of RF field components will enable quantitative separation of the susceptibility and magnetometry components through π phase shifts of individual RF drives without changing anything else, providing further confirmation of the phenomena reported above. A proof-of-principle demonstration of our ability to probe different components of the susceptibility through reconfiguration of the RF field direction is presented later, where the off-diagonal susceptibility of the pinning events is detected in this way. Given the already important role of thermally-driven rapid hopping in eliminating observed minor hysteresis at Barkhausen steps [21], the synchronization must be thermally-assisted. Operating the device at low temperature in future work is required to search for threshold behavior.

Quantitative analysis of susceptibility peaks

In this section we investigate analytically the magnetic torque formula including susceptibility terms, and then estimate observed experimental susceptibility values. It is assumed that the net mechanical torque on the torsional resonator is equal to the net magnetic torque on the permalloy island and that the resulting mechanical amplitudes of motion are small enough to neglect all effects of physical rotation of the sample on its magnetism.

With application of an RF field, the net magnetic moment and total applied field can be written as

$$\begin{aligned}
 \mathbf{m} &= \mathbf{m}^{\text{DC}} + V_{\text{py}} \boldsymbol{\chi} \mathbf{H}^{\text{RF}}, \\
 \mathbf{H} &= \mathbf{H}^{\text{DC}} + \mathbf{H}^{\text{RF}}, \\
 \boldsymbol{\chi} &= \begin{pmatrix} \chi_x & 0 & 0 \\ 0 & \chi_y & 0 \\ 0 & 0 & \chi_z \end{pmatrix},
 \end{aligned} \tag{6.7}$$

Torque terms	On-axis $H_x^{\text{RF}} = 0$	Off-axis $H_x^{\text{RF}} \neq 0$
Magnetization	$-\mu_0 m_x^{\text{DC}} H_z^{\text{RF}}$	$\mu_0 (m_z^{\text{DC}} H_x^{\text{RF}} - m_x^{\text{DC}} H_z^{\text{RF}})$
Susceptibility	-	$-\mu_0 \chi_x V_{\text{py}} H_z^{\text{DC}} H_x^{\text{RF}}$

Table 6.1: Torque terms for on- and off-axis sample positioning.

where \mathbf{m}^{DC} is the static response to \mathbf{H}^{DC} , χ is a magnetic susceptibility tensor, and V_{py} is the volume of the permalloy island. The exerted torque at ω_m can be obtained by inserting the above equation into $\boldsymbol{\tau} = \mathbf{m} \times \mu_0 \mathbf{H}$, so that

$$\boldsymbol{\tau} = \mathbf{m}^{\text{DC}} \times \mu_0 \mathbf{H}^{\text{RF}} + \chi V_{\text{py}} \mathbf{H}^{\text{RF}} \times \mu_0 \mathbf{H}^{\text{DC}}. \quad (6.8)$$

The torque in the \hat{y} -direction can then be extracted:

$$\tau_y \equiv \tau_{m_x} + \tau_{m_z} + \tau_{\chi_x} = -\mu_0 m_x^{\text{DC}} H_z^{\text{RF}} + \mu_0 m_z^{\text{DC}} H_x^{\text{RF}} - \mu_0 \chi_x V_{\text{py}} H_z^{\text{DC}} H_x^{\text{RF}}, \quad (6.9)$$

where τ_{m_x} and τ_{m_z} are DC-moment torques, and τ_{χ_x} is the torque generated by the RF moment. Note that H_y^{RF} cannot contribute to this torque term.

When the sample is positioned on the coil axis, it is driven by a pure H_z^{RF} and the torque on the sample is proportional only to m_x^{DC} (χ_z is ignored due to the shape anisotropy inherent in the thin permalloy island). When the sample is offset from the coil axis, $H_x^{\text{RF}} \neq 0$ and the in-plane susceptibility χ_x can contribute to the net torque. The relevant torque terms for both cases are summarized in Table 6.1.

The on-axis torque term $\mu_0 m_x^{\text{DC}} H_z^{\text{RF}}$ is the regular net moment that produces the hysteresis curve shown in Fig. 6.12. The additional torque exhibited at peaks and dips in Fig. 6.15 is described by the term proportional to χ_x . A key feature is the sign change of only the susceptibility contribution when the measurements made with the sample to the left of coil center are compared with those made to the right (inverting the phase of H_x^{RF} relative to H_z^{RF}). Finally, m_z^{DC} is small on account of the shape anisotropy of the permalloy island, but

should be resolvable in future experiments if back-to-back measurements can be performed at different relative phases of H_x^{RF} and H_z^{RF} while keeping all magnitudes constant.

The experimental RF susceptibility χ_x at each Barkhausen step is calculated based on the ratio of τ_{χ_x}/τ_{m_x} , the torques generated by the RF and DC magnetization respectively,

$$\frac{\tau_{\chi_x}}{\tau_{m_x}} = \frac{\mu_0 \chi_x V_{\text{py}} H_z^{\text{DC}} H_x^{\text{RF}}}{\mu_0 m_x^{\text{DC}} H_z^{\text{RF}}}, \quad (6.10)$$

that is simplified to the following:

$$\chi_x = \frac{m_x^{\text{DC}} H_z^{\text{RF}}}{V_{\text{py}} H_z^{\text{DC}} H_x^{\text{RF}}} \frac{\tau_{\chi_x}}{\tau_{m_x}}. \quad (6.11)$$

A numerical estimate of χ_x^{peak} at each peak can be made by considering $|\tau_{\chi_x}|$ as the size of the peak overshoot (or undershoot) normalized to $|\tau_{m_x}|$, the torque from the magnetic moment at that setting of DC applied field. The numerical scale would be set by the saturation moment of the film (V_{py} multiplied by the saturation magnetization $M_s = 700$ kA/m). For $\Delta x = 1.9$ mm, where $|H_x^{\text{RF}}| = |H_z^{\text{RF}}|$, the peak susceptibility is expressed as

$$\chi_x^{\text{peak}} = \frac{m_x^{\text{DC}}}{V_{\text{py}} H_z^{\text{DC}}} \left| \frac{\tau_{\chi_x}}{\tau_{m_x}} \right|. \quad (6.12)$$

The definition of the net magnetization, $m_x^{\text{DC}}/V_{\text{py}} \equiv M_x^{\text{DC}}$ (which can be read off the graph) allows us to write:

$$\chi_x^{\text{peak}} = \frac{M_x^{\text{DC}}}{H_z^{\text{DC}}} \left| \frac{\tau_{\chi_x}}{\tau_{m_x}} \right|. \quad (6.13)$$

The susceptibility values estimated from measurements for five representative peaks are shown in Fig. 6.16(c) as a function of RF drive amplitude. This figure shows that for a given peak, χ_x^{peak} is approximately constant (within measurement uncertainty) as a function of H_x^{RF} , as expected for a linear magnetic response. The measured values of χ_x^{peak} range between 40 – 400, depending on the peak. The maximum value of χ_x^{peak} is ~ 10 times larger than the quasi-static low field susceptibility in absence of pinning (unattainable in practice). On the other hand, the enhancement is ~ 25 times larger than a typical susceptibility with the core pinned.

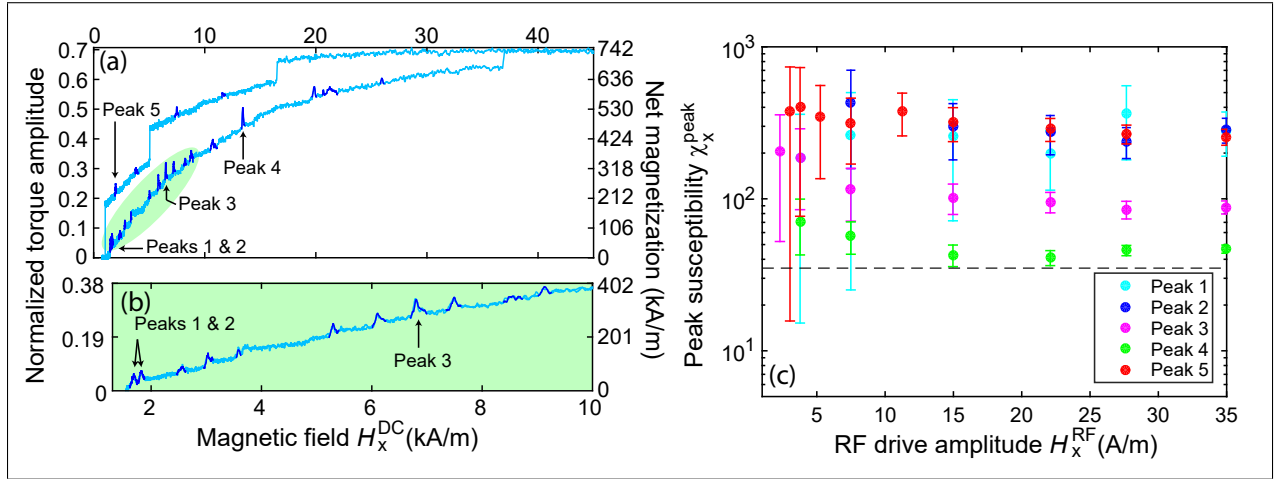


Figure 6.16: Estimated peak susceptibility at select Barkhausen steps for $|H_x^{RF}| = |H_z^{RF}| = 15$ A/m. The full hysteresis and lower branch zoom-in shown in (a) and (b) were measured at non-zero out-of-plane drive amplitude. (c) Susceptibility of each peak identified in (a) and (b) as a function of RF drive. The dotted line shows the low-field quasi-static susceptibility that would be found in the lower branch in the absence of pinning (slope of linear fit to data in (b)).

The enhanced sensitivity provided by these susceptibility peaks can be estimated as follows. For a given minimum detectable torque τ_{\min} , the susceptometry can be performed on a volume of magnetic material $V_{\min} = \tau_{\min} / \mu_0 \chi_x H_x^{RF} H_z^{DC}$. Similarly, this expression can be written in terms of a minimum detectable field $H_{z,\min}^{DC} = \tau_{\min} / V_{py} \mu_0 \chi_x H_x^{RF}$. Each of these expressions illustrates that operating near a point where χ_x is enhanced owing to microscopic properties of the material allows improved sensitivity for a given RF field. Note that owing to the mixing between RF and DC fields responsible for these peaks, the minimum detectable quantities presented above are parametrized by either the H_z^{DC} or H_x^{RF} externally controlled operating conditions.

Effects of magnetic DC bias field direction and thermo-optic heating

To confirm that the fine features seen in the data are Barkhausen steps, another in-plane bias field $H_y^{DC} = 300$ A/m perpendicular to H_x^{DC} was applied using a second one-inch permanent magnet positioned near the device. This additional field shifts the vortex core position in

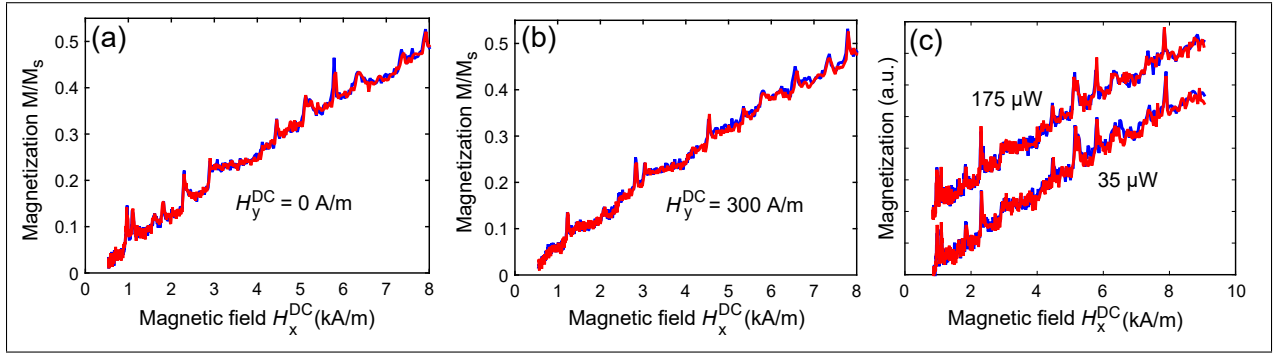


Figure 6.17: Characterization of low field sweeps. (a) Field sweeps with drive field of $H_z^{RF} = 35$ A/m (averaged for a $\sqrt{12}$ noise reduction factor) in the low field regions of the curve reveal features produced by the Barkhausen effect. The blue and red traces show the signals of the decreasing and increasing field sweeps. (b) Same as (a) except an additional bias field $H_y^{DC} = 300$ A/m is applied. (c) Device response at different input laser power as H_x^{DC} is swept at low fields. The responses at 175 μ W and 35 μ W power were normalized and slightly offset for ease in comparison.

the \hat{x} -direction. It is expected then that some different pinning sites will be encountered in the magnetizing curve versus H_x^{DC} , as found in Fig. 6.17(b). Removal of the second magnet also led to a restoration of the peaks shown in Fig. 6.17(a), demonstrating the robustness of these signals.

To rule out possible optical effects such as thermo-optical shift of the cavity resonance influencing the signals, the same measurement was repeated at various laser powers. As shown in Fig. 6.17(c), a reduction of input power by a factor of five did not significantly alter the Barkhausen fingerprint for a given magnetic configuration.

Transmission line platform: susceptibility in response to y-oriented drive

To further demonstrate the Barkhausen susceptibility features arising from RF drive, we have designed and fabricated a circuit board incorporating two separate planar transmission line circuits for generation of both in-plane and out-of-plane RF fields [23], schematically shown in the inset of Fig. 6.18. The rectangular outer loop provides H_z^{RF} while the central stripline applies the in-plane H_y^{RF} component. Each can be driven separately through 50 Ω

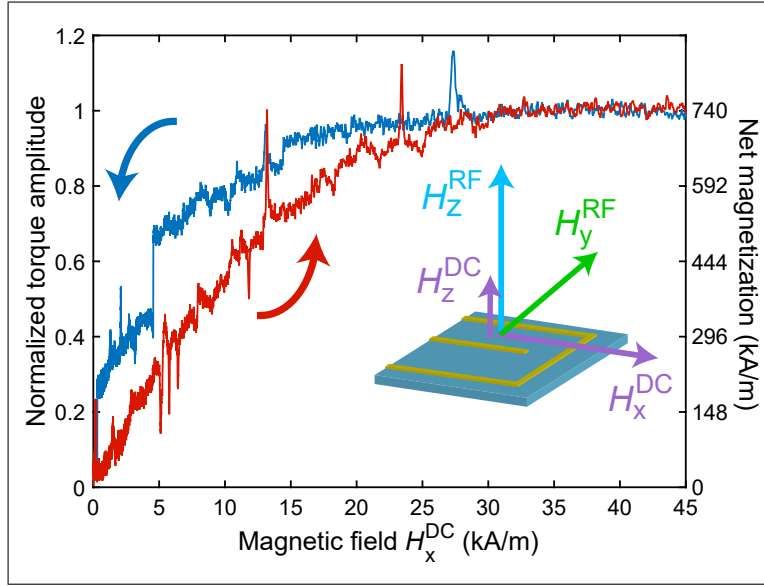


Figure 6.18: Magnetic hysteresis and susceptibility measurement using a planar transmission line. The hysteresis loop was acquired while sweeping H_x^{DC} and applying the RF drive along y using the central stripline (inset). The colors of the trace represent the direction of sweep.

transmission lines using RF power amplifiers, and are designed for reduction of cross-talk between the fields generated by each loop.

Figure 6.18 shows the hysteresis for the case when only the central stripline is driven, applying an RF field that is dominantly in the y -direction. The result is similar to the RF-driven depinning events observed in the main manuscript (where the susceptibility was driven in the x -direction), though in this case both upward and downward peaks are observed. Although the susceptibility response is dominantly in the y -direction, an off-diagonal contribution to the susceptibility can result in an RF driven magnetic moment along x that produces a torque with H_z^{DC} as discussed earlier, resulting in torsional deflection of the device. Depending on the relative position of the pinning sites along x the torque generated through the susceptibility can be positive or negative. The reconfiguration of applied field geometries should allow for precise mapping of the magnetic susceptibility landscape in mesoscopic magnetic structures.

6.4 Summary and implications

The ability of the optomechanical nanocavity to detect nanoscale magnetic phenomena arises from its torque sensitivity of $1.3 \times 10^{-20} \text{ Nm}/\sqrt{\text{Hz}}$, which at field strengths on the order of Earth’s field ($44 - 60 \mu\text{T}$), corresponds to magnetic moment sensitivity of $(2.4 \pm 0.4) \times 10^7 \mu_B$. A minimum detectable volume of magnetic material of $0.015 \pm 0.005 \mu\text{m}^3$ is calculated for the largest susceptibility enhancement; increasing the RF drive would allow for measurement of even smaller volume samples. Compared to previous nanoscale torque magnetometry devices [16, 21, 23] reliant on free-space reflectometry and vacuum or cryogenic operation, this device is of comparable or better sensitivity despite operating in ambient conditions. Furthermore, its relatively low Q_m and MHz operating frequency in-principle allows MHz bandwidth excitation and detection. Operating at MHz frequencies also reduces technical noise related to the operating environment such that the measurement sensitivity is limited by photodetection shot noise. By adjusting the geometry of the supporting structure, higher or lower frequency operation is possible. Among nanoscale optomechanical torque metrology devices, the demonstrated sensitivity is only surpassed by systems operating in vacuum [55] or cryogenic conditions [54], none of which have yet been used for magnetometry or to probe nanoscale condensed matter systems.

Notwithstanding the practical advantages enabled by ambient conditions operation, vacuum and low temperature T_e will reduce the thermal force fluctuations that scale with $\sqrt{T_e/Q_m}$ and limit sensitivity [74]. For example, $Q_m \sim 10^3 - 10^4$ has been observed in our devices in vacuum (see chapter 4), and $Q_m \sim 10^5$ for silicon zipper nanocavity devices has been observed at liquid helium temperatures [31]. This indicates that a 10^4 improvement in the thermally limited sensitivity may be within reach. Even a modest improvement in sensitivity by an order of magnitude, in combination with a maximum driving field of 1 kA/m , could produce magnetic moment sensitivities below $2 \times 10^5 \mu_B$ [53], enabling nanomagnetism-

lab-on-chip studies of a wide range of systems [57, 58].

In conclusion, we have experimentally demonstrated nanocavity optomechanical detection for torque magnetometry and RF susceptometry under ambient conditions. The final device presented in this chapter enabled a detailed study of the magnetostatic response and thermally-assisted driven vortex core hopping dynamics in a mesoscopic permalloy element under applied field. Observations of RF susceptibility due to the Barkhausen effect at the single pinning event level were done for the first time. This torque magnetometry technique complements other device based nanoscale magnetic probes. Compared to planar micro-Hall approaches [178], which have been used to probe single pinning sites but have not been used to measure RF susceptibility, nanocavity torque magnetometry offers higher frequency operation. While it has yet to offer the single spin sensitivity of NV centre based imaging [170, 174], it provides comparatively fast acquisition of net magnetization, allowing measurement of magnetic hysteresis and susceptibility. Reconfiguration of the RF fields allows probing of enhanced susceptibility components of single pinning events, and demonstrates that this magnetometry approach fulfills key requirements for an optomechanical lab-on-a-chip for nanomagnetism.

Time domain measurements, including resonant coupling between mechanical resonances and magnetic dynamics, should be possible in future studies. Furthermore, the magnetometry measurement arrangement presented here opens new possibilities for the study of live biomagnetic samples without the use of vacuum systems [19].

Conclusion

Summary

In this work, nanophotonic optomechanical devices were demonstrated for sensitive detection of torque for magnetometry measurements in ambient conditions. A theoretical framework for optomechanical sensing and numerical simulation capabilities were developed to support the design of photonic crystal split-beam cavities with the goal to enable torsional motion of a mechanical resonator coupled to a source of magnetic torque. The nanoscale devices were fabricated and characterized with torque sensitivity reaching $1.2 \times 10^{-20} \text{ Nm}/\sqrt{\text{Hz}}$ at room temperature and pressure as predicted.

Novel optomechanical phenomena were then discovered within our devices. Beyond dispersive optomechanics (g_{om}), where the mechanical displacement modifies the optical resonance, dissipative-intrinsic (g_i) and dissipative-external (g_e) optomechanical couplings were found to strongly influence the optomechanical response of split-beam cavities. The first is related to the change in optical quality factor Q_o while the latter is due to fiber-cavity coupling γ_e . Both couplings are modulated at the same mechanical frequency as g_{om} . Our experiments show for the first time the combination of all three optomechanical couplings inside a single device with sufficient interference to produce mechanical-mode-dependent optomechanical responses. Moreover, we established the importance of the fiber taper in our experiments beyond optical readout by displaying the capability to tune g_{om} and g_e according to the fiber-cavity distance and the location of the particular mechanical resonator. The ratio of dissipative-external to dispersive coupling can be adjusted in real-time. Future designs might be able to predominantly exhibit dissipative coupling where optomechanics can be performed at resonance ω_o with potential research pointing in this direction.

The high torque sensitivity of our nanophotonic optomechanical sensor was employed

as a torque magnetometer and radio-frequency (RF) magnetic susceptometer. We have demonstrated observations of the unique net magnetization and RF driven responses of single mesoscopic magnetic structures in ambient conditions. The magnetic moment resolution is sufficient for observation of Barkhausen steps in the magnetic hysteresis of a lithographically-patterned permalloy island. In addition, significantly enhanced RF susceptibility is found over narrow field ranges and attributed to thermally-assisted driven hopping of a magnetic vortex core between neighboring pinning sites. The on-chip magneto-susceptometer scheme offers a promising path to powerful integrated cavity optomechanical devices for quantitative characterization of magnetic micro- and nanosystems in science and technology.

Future outlook

With further innovative and creative designs, sensitivity in optomechanical devices can be improved. The thermally-limited torque sensitivity of our devices points to potential improvements of its mechanical properties. At room temperature and fixed operating mechanical frequency, only smaller ($m_{\text{eff}} < 0.5$ pg) nanomechanical resonators with lower dissipation (higher Q_m) will allow for lower thermal noise floor. Phononic shielding provides a glimpse of feasibility however band-gap engineering requires micron to millimeter scale structures at low frequencies, adding fabrication complexity. Moreover, the majority of phonon shielding systems, with ω_m in the 100 MHz to GHz range of operation [83, 85], is incompatible with large scale torsional displacement due to mismatched geometry.

In the regime with negligible thermal noise (eg. low temperature), technical noise is the next challenge for sensitivity. Prospects for higher g_{om} and Q_o are available such as nanophotonic cavities exploiting the strongly confined mode in a slot between two dielectric structures [90, 188, 189]. A shift to a different fiber coupling scheme can provide opportunities to optimize our optical readout system and our photon collection efficiency as well as T_o [111].

It is reasonable then to turn our future outlook to higher frequencies of operation and

even novel forms of torsional motion. A GHz-range mechanical resonance would set the stage for a possible intersection with ferromagnetic resonance frequencies [5]. This magneto-mechanical coupling will allow coherent exchange of energy between spin and phonons. One potential configuration is the coupling of spin waves to surface acoustic waves [190]. The periodic arrangement of spins through an RF current can impart local rotation on the crystal lattice at the same periodicity causing an acoustic wave to propagate at the surface of the material. These mechanical waves can transduce an optical cavity via photoelastic optomechanical coupling [62, 65]. In this regard, acoustic waves have already been shown to integrate efficiently with optomechanical devices [95, 191]. The transfer of energy between spins to phonons to photons is therefore conceivable (and vice-versa). This congruence of magnetism, mechanics, and optics in a package might prove to be a research boon to come with many potential applications. Some already call this field “cavity magnomechanics” [192].

Bibliography

- [1] C. A. Coulomb. Premier mémoire sur l'électricité et le magnétisme. *Histoire de l'Académie Royale des Sciences*, 88:569–577, 1785.
- [2] H. Cavendish. Experiments to determine the density of the earth. *Phil. Trans. Roy. Soc. Lond.*, 88:469–526, 1798.
- [3] S. J. Barnett. Magnetization by rotation. *Phys. Rev.*, 6:239–270, 1915.
- [4] A. Einstein and W. J. de Haas. Experimental proof of the existence of Ampère's molecular currents. *Royal Neth. Acad. Arts Sciences*, 18:696–711, 1915.
- [5] J. E. Losby and M. R. Freeman. Spin mechanics. *arXiv:1601.00674*, 2016.
- [6] M. N. Baibich, J. M. Broto, A. Fert, F. Nguyen Van Dau, F. Petroff, P. Etienne, G. Creuzet, A. Friederich, and J. Chazelas. Giant magnetoresistance of (001)Fe/(001)Cr magnetic superlattices. *Phys. Rev. Lett.*, 61:2472, 1988.
- [7] G. Binasch, P. Grunberg, F. Saurenbach, and W. Zinn. Enhanced magnetoresistance in layered magnetic structures with antiferromagnetic interlayer exchange. *Phys. Rev. B*, 39:4828, 1989.
- [8] J. A. Katine and E. E. Fullerton. Device implications of spin-transfer torques. *J. Magn. Magn. Mater.*, 320:1217–1226, 2008.
- [9] S. D. Bader and S. S. P. Parking. Spintronics. *Annu. Rev. Condens. Matter Phys.*, 1:71–88, 2010.
- [10] T. Shinjo. *Nanomagnetism and Spintronics*. Elsevier LTD, Oxford, 2013.
- [11] E. D. Dahlberg and R. Proksch. Magnetic microscopies: the new additions. *Journal of magnetism and magnetic materials*, 200(1):720–728, 1999.

- [12] S. A. Wolf, D. D. Awschalom, R. A. Buhrman, J. M. Daughton, S. von Molnar, M. L. Roukes, A. Y. Chtchelkanova, and D. M. Treger. Spintronics: a spin-based electronics vision for the future. *Science*, 294:1488–1495, 2001.
- [13] K. Tajima and S. Chikazumi. Conventional torque magnetometer for measuring a large magnetic anisotropy. *Japanese Journal of Applied Physics*, 6(7):897–897, 1967.
- [14] D. W. Carr, S. Evoy, L. Sekaric, H. G. Craighead, and J. M. Parpia. Parametric amplification in a torsional microresonator. *Appl. Phys. Lett.*, 77(10):1545, 2000.
- [15] J. Moreland. Micromechanical instruments for ferromagnetic measurements. *J. Phys. D: Appl. Phys.*, 36(R39):R39–R51, 2003.
- [16] J. P. Davis, D. Vick, D. C. Fortin, J. A. J. Burgess, W. K. Hiebert, and M. R. Freeman. Nanotorsional resonator torque magnetometry. *Appl. Phys. Lett.*, 96:072513, 2010.
- [17] S.-H. Lim, A. Imtiaz, T. M. Wallis, S. Russek, P. Kabos, L. Cai, and E. M. Chudnovsky. Magneto-mechanical investigation of spin dynamics in magnetic multilayers. *Europhys. Lett.*, 105(3):37009, 2014.
- [18] J. E. Losby, Z. Diao, F. Fani Sani, D. T. Grandmont, M. Belov, J. A. J. Burgess, W. K. Hiebert, and M. R. Freeman. Nanomechanical ac susceptometry of an individual mesoscopic ferrimagnet. *Solid State Comm.*, 198:3–6, 2014.
- [19] T. Firdous, D. Vick, M. Belov, F. Fani Sani, A. McDermott, J. E. Losby, D. A. Bazylinski, T. Prozorov, D. K. Potter, and M. R. Freeman. Nanomechanical torque magnetometry of an individual aggregate of 350 nanoparticles. *Can. J. Phys.*, 93:1–5, 2015.
- [20] A. Buchter, J. Nagel, D. Ruffer, F. Xue, D. P. Weber, O. F. Kieler, T. Weimann, J. Kohlmann, A. B. Zorin, E. Russo-Averchi, R. Huber, P. Berberich, A. Fontcuberta i Morral, M. Kemmler, R. Kleiner, D. Koelle, D. Grundler, and M. Poggio. Reversal

- mechanism of an individual ni nanotube simultaneously studied by torque and SQUID magnetometry. *Physical Review Letters*, 111(6), 2013.
- [21] J. A. J. Burgess, A. E. Fraser, F. Fani Sani, D. Vick, B. D. Hauer, J. P. Davis, and M. R. Freeman. Quantitative magneto-mechanical detection and control of the barkhausen effect. *Science*, 339(16):1051–1054, 2013.
- [22] C. Ascoli, P. Baschieri, C. Frediani, L. Lenci, M. Martinelli, G. Alzetta, R. M. Celli, and L. Pardi. Micromechanical detection of magnetic resonance by angular momentum absorption. *Appl. Phys. Lett.*, 69:3920–3922, 1996.
- [23] J. E. Losby, F. Fani Sani, D. T. Grandmont, Z. Diao, M. Belov, J. A. J. Burgess, S. R. Compton, W. K. Hiebert, D. Vick, K. Mohammad, E. Salami, G. E. Bridges, T. J. Thomson, and M. R. Freeman. Torque-mixing magnetic resonance spectroscopy. *Science*, 350(6262):798–801, 2015.
- [24] J. E. Losby. *Nanomechanical Torque Magnetometry and AC Susceptometry of Mesoscopic Magnetic Structures*. PhD thesis, University of Alberta, 2014.
- [25] M. Aspelmeyer, T. J. Kippenberg, and F. Marquardt. Cavity optomechanics. *Reviews of Modern Physics*, 86(4):1391, 2014.
- [26] M. Eichenfield, J. Chan, R. M. Camacho, K. J. Vahala, and O. Painter. Optomechanical crystals. *Nature*, 462(7269):78–82, 2009.
- [27] E. Gavartin, R. Braive, I. Sagnes, O. Arcizet, A. Beveratos, T. J. Kippenberg, and I. Robert-Philip. Optomechanical coupling in a two-dimensional photonic crystal defect cavity. *Phys. Rev. Lett.*, 106(20):203902, 2011.
- [28] X. Sun, J. Zhang, M. Poot, C.W. Wong, and H.X. Tang. Femtogram doubly clamped nanomechanical resonators embedded in a high-Q two-dimensional photonic crystal nanocavity. *Nano Lett.*, 12(5):2299–2305, 2012.

- [29] J. Chan, T. P. Mayer Alegre, A. H. Safavi-Naeini, J. T. Hill, A. Krause, S. Groblacher, M. Aspelmeyer, and O. Painter. Laser cooling of a nanomechanical oscillator into its quantum ground state. *Nature*, 478:89–92, 2011.
- [30] A. H. Safavi-Naeini, J. Chan, J. T. Hill, T. P. M. Alegre, A. Krause, and O. Painter. Observation of quantum motion of a nanomechanical resonator. *Phys. Rev. Lett.*, 108(3):033602, 2012.
- [31] A. Safavi-Naeini, S. Groblacher, J.T. Hill, J. Chan, M. Aspelmeyer, and O Painter. Squeezed light from a silicon micromechanical resonator. *Nature*, 500:185–189, 2013.
- [32] S. Weis, R. Rivière, S. Deléglise, E. Gavartin, O. Arcizet, A. Schliesser, and T. J. Kippenberg. Optomechanically induced transparency. *Science*, 330(6010):1520–1523, 2010.
- [33] A. H Safavi-Naeini, T.P. M. Alegre, J. Chan, M. Eichenfield, M. Winger, Q. Lin, J. T. Hill, D. E. Chang, and O. Painter. Electromagnetically induced transparency and slow light with optomechanics. *Nature*, 472(7341):69–73, 2011.
- [34] D. M. Meekhof, C Monroe, B. E. King, W. M. Itano, and D. J. Wineland. Generation of nonclassical motional states of a trapped atom. *Phys. Rev. Lett.*, 76(11):1796, 1996.
- [35] W. Marshall, C. Simon, R. Penrose, and D. Bouwmeester. Towards quantum superpositions of a mirror. *Phys. Rev. Lett.*, 91:130401, Sep 2003.
- [36] J. D. Teufel, T. Donner, D. Li, J. W. Harlow, M. S. Allman, K. Cicak, A. J. Sirois, J. D. Whittaker, K. W. Lehnert, and R. W. Simmonds. Sideband cooling of micromechanical motion to the quantum ground state. *Nature*, 475(7356):359–363, 2011.
- [37] A. Schliesser, O. Arcizet, R. Rivière, G. Anetsberger, and T. J. Kippenberg. Resolved-sideband cooling and position measurement of a micromechanical oscillator close to the heisenberg uncertainty limit. *Nature Phys.*, 5(7):509–514, 2009.

- [38] S. Schreppler, N. Spethmann, N. Brahms, T. Botter, M. Barrios, and D. M. Stamper-Kurn. Optically measuring force near the standard quantum limit. *Science*, 344(6191):1486–1489, 2014.
- [39] L. F. Buchmann, S. Schreppler, J. Kohler, N. Spethmann, and D. M. Stamper-Kurn. Complex squeezing and force measurement beyond the standard quantum limit. *Phys. Rev. Lett.*, 117(3), 2016.
- [40] LIGO Scientific Collaboration. A gravitational wave observatory operating beyond the quantum shot-noise limit. *Nature Phys.*, 7(12):962–965, 2011.
- [41] B. P. Abbott, R. Abbott, T. D. Abbott, M. R. Abernathy, F. Acernese, K. Ackley, C. Adams, T. Adams, P. Addesso, and R. X. *et al.* Adhikari. Observation of gravitational waves from a binary black hole merger. *Physical review letters*, 116(6):061102, 2016.
- [42] O. Arcizet, P.-F. Cohadon, T. Briant, M. Pinard, A. Heidmann, J.-M. Mackowski, C. Michel, L. Pinard, O. Français, and L. Rousseau. High-sensitivity optical monitoring of a micromechanical resonator with a quantum-limited optomechanical sensor. *Phys. Rev. Lett.*, 97:133601, 2006.
- [43] M. Li, W. H. P. Pernice, and H. X. Tang. Broadband all-photonic transduction of nanocantilevers. *Nat. Nano.*, 4(6):377–382, 2009.
- [44] G. Anetsberger, O. Arcizet, Q. P. Unterreithmeier, R. Rivière, A. Schliesser, E. M. Weig, J. P. Kotthaus, and T. J. Kippenberg. Near-field cavity optomechanics with nanomechanical oscillators. *Nature Phys.*, 5(12):909–914, 2009.
- [45] G. Anetsberger, E. Gavartin, O. Arcizet, Q. P. Unterreithmeier, E. M. Weig, M. L. Gorodetsky, J. P. Kotthaus, and T. J. Kippenberg. Measuring nanomechanical motion with an imprecision below standard quantum limit. *Phys. Rev. A*, 82(6):061804, 2010.

- [46] K. Srinivasan, H. Miao, M.T. Rakher, M. Davanço, and V. Aksyuk. Optomechanical transduction of an integrated silicon cantilever probe using a microdisk resonator. *Nano Lett.*, 11:791, 2011.
- [47] E. Gavartin, P. Verlot, and T. J. Kippenberg. A hybrid on-chip optomechanical transducer for ultrasensitive force measurements. *Nat. Nano.*, 7(8):509–514, 2012.
- [48] Y. Liu, H. Miao, V. Aksyuk, and K. Srinivasan. Wide cantilever stiffness range cavity optomechanical sensors for atomic force microscopy. *Opt. Express*, 20(16):18268–18280, 2012.
- [49] C. Doolin, P. H. Kim, B. D. Hauer, A. J. R. MacDonald, and J. P. Davis. Multidimensional optomechanical cantilevers for high frequency atomic force microscopy. *New J. Phys.*, 16:035001, 2014.
- [50] A. G. Krause, M. Winger, T. D. Blasius, W. Lin, and O. Painter. A high-resolution microchip optomechanical accelerometer. *Nat. Photon.*, 6(11):768–772, 2012.
- [51] S. Forstner, S. Prams, J. Knittel, E. D. van Ooijen, J. D. Swaim, G. I. Harris, A. Szorkovszky, W. P. Bowen, and H. Rubinsztein-Dunlop. Cavity optomechanical magnetometer. *Phys. Rev. Lett.*, 108:120801, 2012.
- [52] S. Forstner, E. Sheridan, J. Knittel, C. L. Humphreys, G. A. Brawley, H. Rubinsztein-Dunlop, and W. P. Bowen. Ultrasensitive optomechanical magnetometry. *Adv. Mater.*, 26(36):6348–6353, 2014.
- [53] P. H. Kim, C. Doolin, B. D. Hauer, A. J. R. MacDonald, M. R. Freeman, P. E. Barclay, and J. P. Davis. Nanoscale torsional optomechanics. *Appl. Phys. Lett.*, 102(1852):053102, 2013.
- [54] P. H. Kim, B. D. Hauer, C. Doolin, F. Souris, and J. P. Davis. Approaching the standard quantum limit of mechanical torque sensing. *Nature Communications*, 7(13165),

2016.

- [55] H. Li and M. Li. Optomechanical photon shuttling between photonic cavities. *Nat. Nano.*, 9(11):913–919, 2014.
- [56] L. He, H. Li, and M. Li. Optomechanical measurement of photon spin angular momentum and optical torque in integrated photonic devices. *Sci. Adv.*, 2(9):e1600485, 2016.
- [57] D. Rugar, R. Budakian, H. J. Mamin, and B. W. Chui. Single spin detection by magnetic resonance force microscopy. *Nature*, 430(6997):329–332, 2004.
- [58] A. C. Bleszynski-Jayich, W. E. Shanks, B. Peaderf, E. Ginossar, F. von Oppen, L. Glazman, and J. G. E. Harris. Persistent currents in normal metal rings. *Science*, 326(5950):272–275, 2009.
- [59] M. Eichenfield, J. Chan, A. H. Safavi-Naeini, K. J. Vahala, and O. Painter. Modeling dispersive coupling and losses of localized optical and mechanical modes in optomechanical crystals. *Opt. Express*, 17(22):20078–20098, 2009.
- [60] B. D. Hauer, C. Doolin, K. S. D. Beach, and J. P. Davis. A general procedure for thermomechanical calibration of nano/micro-mechanical resonators. *Annals of Physics*, 339:181–207, 2013.
- [61] S. G. Johnson, M. Ibanescu, M. A. Skorobogatiy, O. Weisberg, J. D. Joannopoulos, and Y. Fink. Perturbation theory for maxwell’s equations with shifting material boundaries. *Phys. Rev. E*, 65:066611, 2002.
- [62] J. Chan, A. H. Safavi-Naeini, J. Hill, S. Meenehan, and O. Painter. Optimized optomechanical crystal cavity with acoustic radiation shield. *Appl. Phys. Lett.*, 101(8):081115, 2012.

- [63] V. T. K. Sauer, Z. Diao, M. R. Freeman, and W. K. Hiebert. Nanophotonic detection of side-coupled nanomechanical cantilevers. *Appl. Phys. Lett.*, 100(26):261102, 2012.
- [64] T. Ono and M. Esashi. Magnetic force and optical force sensing with ultrathin silicon resonator. *Rev. Sci. Instr.*, 74(12):5141, 2003.
- [65] K. C. Balram, M. Davanço, J. Y. Lim, J. D. Song, and K. Srinivasan. Moving boundary and photoelastic coupling in gas optomechanical resonators. *Optica*, 1:414–420, 2014.
- [66] F. Tian, G. Zhou, F. S. Chau, and J. Deng. Torsional optical spring effect in coupled nanobeam photonic crystal cavities. *Opt. Lett.*, 39:6289–6292, 2014.
- [67] C. W. Gardiner and M. J. Collett. Input and output in damped quantum systems: Quantum stochastic differential equations and the master equation. *Phys. Rev. A*, 31(6):3761–3774, jun 1985.
- [68] C. W. Gardiner and P. Zoller. *Quantum Noise*. Springer, Berlin, 1991.
- [69] A. G. Krause. *Acceleration sensing, feedback cooling, and nonlinear dynamics with nanoscale cavity-optomechanics devices*. PhD thesis, California Institute of Technology, 2015.
- [70] A. Cleland. Thermomechanical noise limits on parametric sensing with nanomechanical resonators. *New J. Phys.*, 7:135, 2005.
- [71] A. A. Clerk, M. H. Devoret, S. M. Girvin, F. Marquardt, and R. J. Schoelkopf. Introduction to quantum noise, measurement, and amplification. *Reviews of Modern Physics*, 82(2):1155–1208, 2010.
- [72] A. N. Cleland and M. L. Roukes. Noise processes in nanomechanical resonators. *J. Appl. Phys.*, 92(5):2758, 2002.

- [73] T. D. Blasius. *Optomechanical Inertial Sensors and Feedback Cooling*. PhD thesis, California Institute of Technology, 2016.
- [74] M. Wu, A. C. Hryciw, C. Healey, D. P. Lake, H. Jayakumar, M. R. Freeman, J. P. Davis, and P. E. Barclay. Dissipative and dispersive optomechanics in a nanocavity torque sensor. *Phys. Rev. X*, 4:021052, 2014.
- [75] S. Forstner, J. Knittel, E. Sheridan, J. D. Swaim, H. Rubinsztein-Dunlop, and W. P. Bowen. Sensitivity and performance of cavity optomechanical field sensors. *Photonic Sensors*, 2(3):259–270, 2012.
- [76] O. Geřardin, H. Le Gall, M. J. Donahue, and N. Vukadinovic. Micromagnetic calculation of the high frequency dynamics of nano-size rectangular ferromagnetic stripes. *J. Appl. Phys.*, 89(11):7012, 2001.
- [77] M. Yamaguchi, Y. Miyazawa, K. Kaminishi, H. Kikuchi, S. Yabukami, K.I. Arai, and T. Suzuki. Soft magnetic applications in the RF range. *Journal of Magnetism and Magnetic Materials*, 268(1-2):170–177, 2004.
- [78] N. G. Chechenin. Ultra-soft magnetic films: micromagnetism and high frequency properties. *Microelectronic Engineering*, 81(2-4):303–309, 2005.
- [79] N. Liu, F. Giesen, M. Belov, J. Losby, J. Moroz, A. E. Fraser, G. McKinnon, T. J. Clement, V. Sauer, W. K. Hiebert, and M. R. Freeman. Time-domain control of ultrahigh-frequency nanomechanical systems. *Nature Nanotechnology*, 3(12):715–719, 2008.
- [80] A. M. Yao and M. J. Padgett. Orbital angular momentum: Origins, behavior and applications. *Advances in Optics and Photonics*, 3:161–204, 2011.
- [81] M. Bhattacharya. Rotational cavity optomechanics. *J. Opt. Soc. Amer. B*, 32:B55–B60, 2015.

- [82] H. Shi and M. Bhattacharya. Optomechanics based on angular momentum exchange between light and matter. *J. Phys. B: At. Mol. Opt. Phys.*, 49(153001), 2015.
- [83] F. C. Hsu, J. C. Hsu, T. C. Huang, C. H. Wang, and P. Chang. Reducing support loss in micromechanical ring resonators using phononic band-gap structures. *J. Phys. D: Appl. Phys.*, 44(37):375101, 2011.
- [84] G. D. Cole, I. Wilson-Rae, K. Werbach, M. R. Vanner, and M. Aspelmeyer. Phonon-tunnelling dissipation in mechanical resonators. *Nature Communications*, 2:231, 2011.
- [85] T. P. Mayer Alegre, A. Safavi-Naeini, M. Winger, and O. Painter. Quasi-two-dimensional optomechanical crystals with a complete phononic bandgap. *Opt. Express*, 19(6):5658, 2011.
- [86] H. Zhu and J. E.-Y. Lee. Design of phononic crystal tethers for frequency-selective quality factor enhancement in AlN piezoelectric-on-silicon resonators. *Procedia Engineering*, 120:516–519, 2015.
- [87] H. Benisty, V. Berger, J.-M. Gerard, J.-M. Lourtioz, and D. Maystre. *Photonic Crystals*. Springer, 2008.
- [88] J. D. Joannopoulos. *Photonic Crystals*. University Press Group Ltd, 2008.
- [89] J. Chan, M. Eichenfield, R. Camacho, and O. Painter. Optical and mechanical design of a zipper photonic crystal optomechanical cavity. *Opt. Express*, 17:3802–3817, 2009.
- [90] M. Eichenfield, R. Camacho, J. Chan, K. J. Vahala, and O. Painter. A picogram and nanometer scale photonic crystal opto-mechanical cavity. *Nature*, 459:550–555, 2009.
- [91] S. M. Meenehan, J. D. Cohen, S. Gröblacher, J. T. Hill, A. H. Safavi-Naeini, M. Aspelmeyer, and O. Painter. Silicon optomechanical crystal resonator at millikelvin temperatures. *Phys. Rev. A*, 90(1), jul 2014.

- [92] P. B. Deotare, M. W. McCutcheon, I. W. Frank, M. Khan, and M. Lončar. High quality factor photonic crystal nanobeam cavities. *Appl. Phys. Lett.*, 94:121106, 2009.
- [93] Q. Quan, P. B. Deotare, and M. Lončar. Photonic crystal nanobeam cavity strongly coupled to the feeding waveguide. *Appl. Phys. Lett.*, 96:203102, 2010.
- [94] X. Sun, X. Zhang, and H. X. Tang. High-q silicon optomechanical microdisk resonators at gigahertz frequencies. *Appl. Phys. Lett.*, 100(17):173116, 2012.
- [95] K. C. Balram, M. I. Davanço, J. D. Song, and K. Srinivasan. Coherent coupling between radiofrequency, optical and acoustic waves in piezo-optomechanical circuits. *Nature Photonics*, 10(5):346–352, 2016.
- [96] A. C. Hryciw and P. E. Barclay. Optical design of split-beam photonic crystal nanocavities. *Opt. Lett.*, 38(10):1612–1614, 2013.
- [97] C. H. Mastrangelo and C. H. Hsu. Mechanical stability and adhesion of microstructures under capillary forces - part ii: Experiments. *J. MEMS*, 2:44–55, 1993.
- [98] Y. Zhang and Y. Zhao. Flexural contact in mems stiction. *Int. J. Solids and Struc.*, 49:2208–2214, 2012.
- [99] Y. Zhao. Stiction and anti-stiction in mems and nems. *Acta Mechanica Sinica*, 19:1–10, 2003.
- [100] A. A. Stekolnikov and F. Bechstedt. Shape of free and constrained group-IV crystal-lites: Influence of surface energies. *Phys. Rev. B*, 72(12), sep 2005.
- [101] N. Bernstein, M. J. Aziz, and E. Kaxiras. Amorphous-crystal interface in silicon: A tight-binding simulation. *Phys. Rev. B*, 58(8):4579–4583, aug 1998.
- [102] K. E. Grutter, M. Davanço, and K. Srinivasan. Si₃N₄ nanobeam optomechanical crystals. *IEEE J. Sel. Topics Quantum Electron.*, 21:2700611, 2015.

- [103] C. P. Michael, M. Borselli, T. J. Johnson, C. Chrystala, and O. Painter. An optical fiber-taper probe for wafer-scale microphotonic device characterization. *Opt. Express*, 15:4745–4752, 2007.
- [104] B. D. Hauer, P. H. Kim, C. Doolin, A. J. R. MacDonald, H. Ramp, and J. P. Davis. On-chip cavity optomechanical coupling. *EPJ Techniques and Instrumentation*, 1(1), 2014.
- [105] P. E. Barclay, K. Srinivasan, M. Borselli, and O. Painter. Efficient input and output optical fiber coupling to a photonic crystal waveguide. *Opt. Lett.*, 29(7):697–699, 2004.
- [106] P. E. Barclay, K. Srinivasan, M. Borselli, and O. Painter. Probing the dispersive and spatial properties of planar photonic crystal waveguide modes via highly efficient coupling from optical fiber tapers. *Appl. Phys. Lett.*, 85(1):4–6, 2004.
- [107] P. E. Barclay, K. Srinivasan, and O. Painter. Nonlinear response of silicon photonic crystal microresonators excited via an integrated waveguide and a fiber taper. *Opt. Express*, 13:801–820, 2005.
- [108] P. E. Barclay, B. Lev, K. Srinivasan, H. Mabuchi, and O. Painter. Integration of fiber coupled high-q sinx microdisks with atom chips. *Appl. Phys. Lett.*, 89:131108, September 2006.
- [109] P. E. Barclay, O. Painter, C. Santori, K.-M. Fu, and R.G. Beausoleil. Coherent interference effects in a nano-assembled optical cavity-qed system. *Opt. Express*, 19:8081, 2009.
- [110] J. Lipfert, J. W. J. Kerssemakers, T. Jager, and N. H. Dekker. Magnetic torque tweezers: measuring torsional stiffness in dna and reca-dna filaments. *Nat. Methods*, 7(12):977–980, 2010.

- [111] S. Groblacher, J. Hill, A. Safavi-Naeini, J. Chan, and O Painter. Highly efficient coupling from an optical fiber to a nanoscale silicon optomechanical cavity. *Appl. Phys. Lett.*, 103(181104), 2013.
- [112] T. Lin, X. Zhang, Y. Zou, F. S. Chau, J. Deng, and G. Zhou. Out-of-plane nano-electro-mechanical tuning of the fano resonance in photonic crystal split-beam nanocavity. *Appl. Phys. Lett.*, 107:153107, 2015.
- [113] T. Lin, F. Tian, P. Shi, F. S. Chau, G. Zhou, X. Tang, and J. Deng. Design of mechanically-tunable photonic crystal split-beam nanocavity. *Opt. Lett.*, 40:3504–3507, 2015.
- [114] P. Shi, H. Du, F. S. Chau, G. Zhou, and J. Deng. Tuning the quality factor of split nanobeam cavity by nanoelectromechanical systems. *Opt. Express*, 23:19338–19347, 2015.
- [115] O. Basarir, S. Bramhavar, and K. L. Ekinici. Near-field optical transducer for nanomechanical resonators. *Appl. Phys. Lett.*, 97(25):253114, 2010.
- [116] O. Basarir, S. Bramhavar, G. Basilio-Sanchez, T. Morse, and K. L. Ekinici. Sensitive micromechanical displacement detection by scattering evanescent optical waves. *Optics Letters*, 35(11):1792, 2010.
- [117] O. Basarir, S. Bramhavar, and K. L. Ekinici. Motion transduction in nanoelectromechanical systems (NEMS) arrays using near-field optomechanical coupling. *Nano Letters*, 12(2):534–539, 2012.
- [118] M. Li, W.H.P. Pernice, and H.X. Tang. Reactive cavity optical force on microdisk-coupled nanomechanical beam waveguides. *Phys. Rev. Lett.*, 103:223901, 2009.
- [119] G. Anetsberger, E. M. Weig, J. P. Kotthaus, and T. J. Kippenberg. Cavity optomechanics and cooling nanomechanical oscillators using microresonator enhanced evanes-

- cent near-field coupling. *Comptes Rendus Physique*, 12:800–816, 2011.
- [120] K. Srinivasan, P. E. Barclay, M. Borselli, and O. Painter. Optical-fiber based measurement of an ultra-small volume high-q photonic crystal microcavity. *Phys. Rev. B*, 70:081306(R), 2004.
- [121] B.-Q. Shen, X.-C. Yu, Y. Zhi, L. Wang, D. Kim, Q. Gong, and Y.-F. Xiao. Detection of single nanoparticles using the dissipative interaction in a high-Q microcavity. *Phys. Rev. Applied*, 5(2), 2016.
- [122] M. I. Cheema, S. Mehrabani, A. A. Hayat, Y.-A. Peter, A. M. Armani, and A. G. Kirk. Simultaneous measurement of quality factor and wavelength shift by phase shift microcavity ring down spectroscopy. *Opt. Express*, 20(8):9090, 2012.
- [123] J. Knittel, J. H. Chow, M. B. Gray, M. A. Taylor, and W. P. Bowen. Ultrasensitive real-time measurement of dissipation and dispersion in a whispering-gallery mode microresonator. *Optics Letters*, 38(11):1915, 2013.
- [124] K. Eom, H. S. Park, D. S. Yoon, and T. Kwon. Nanomechanical resonators and their applications in biological/chemical detection: Nanomechanics principles. *Physics Reports*, 503(4-5):115–163, jun 2011.
- [125] F. Elste, S. M. Girvin, and A. A. Clerk. Quantum noise interference and backaction cooling in cavity nanomechanics. *Phys. Rev. A*, 102:207209, 2009.
- [126] S. Huang and G. S. Agarwal. Reactive coupling can beat the motional quantum limit of nanowaveguides coupled to a microdisk resonator. *Phys. Rev. A*, 82:033811, 2010.
- [127] A. Xuereb, R. Schnabel, and K. Hammerer. Dissipative optomechanics in a michelson-sagnac interferometer. *Phys. Rev. Lett.*, 107:213604, 2011.
- [128] T. Weiss and A. Nunnenkamp. Quantum limit of laser cooling in dispersively- and dissipatively-coupled optomechanical systems. *Phys. Rev. A*, 88:023850, 2013.

- [129] S. P. Tarabrin, H. Kaufer, F. Y. Khalili, R. Schnabel, and K. Hammerer. Anomalous dynamic backaction in interferometers. *Phys. Rev. A*, 88:023809, 2013.
- [130] Y. C. Liu, Y. F. Xiao, X. Luan, and C. W. Wong. Dynamic dissipative cooling of a mechanical resonator in strong coupling optomechanics. *Phys. Rev. Lett.*, 110(15):153606, 2013.
- [131] W.-J. Gu, G.-X. Li, and Y.-P. Yang. Generation of squeezed states in a movable mirror via dissipative optomechanical coupling. *Phys. Rev. A*, 88(1):013835, 2013.
- [132] R. M. Cole, G. A. Brawley, V. P. Adiga, R. De Alba, J. M. Parpia, B. Ilic, H. G. Craighead, and W. P. Bowen. Evanescent-field optical readout of graphene mechanical motion at room temperature. *Phys. Rev. Applied*, 3(2), 2015.
- [133] K. Qu and G. S. Agarwal. Generating quadrature squeezed light with dissipative optomechanical coupling. *Phys. Rev. A*, 91(6), jun 2015.
- [134] D. Kilda and A. Nunnenkamp. Squeezed light and correlated photons from dissipatively coupled optomechanical systems. *Journal of Optics*, 18(1):014007, 2015.
- [135] T. Chen and X.-B. Wang. Fast cooling in dispersively and dissipatively coupled optomechanics. *Sci. Rep.*, 5:7745, 2015.
- [136] S. P. Vyatchanin and A. B. Matsko. Quantum speed meter based on dissipative coupling. *Phys. Rev. A*, 93(6), 2016.
- [137] A. Sawadsky, H. Kaufer, R. M. Nia, S. P. Tarabrin, F. Y. Khalili, K. Hammerer, and R. Schnabel. Observation of generalized optomechanical coupling and cooling on cavity resonance. *Physical Review Letters*, 114(4), jan 2015.
- [138] L. Tian. Cool and heavy. *Physics*, 8, 2015.

- [139] A. C. Hryciw, M. Wu, B. Khanaliloo, and P. E. Barclay. Tuning of nanocavity optomechanical coupling using a near-field fiber probe. *Optica*, 2(5):491–496, 2015.
- [140] M. Li, W. H. P. Pernice, C. Xiong, T. Baehr-Jones, M. Hochberg, and H. X. Tang. Harnessing optical forces in integrated photonic circuits. *Nature*, 456(7221):480–484, 2008.
- [141] H. C. Liu and A. Yariv. Designing coupled-resonator optical waveguides based on high- Q tapered grating-defect resonators. *Opt. Express*, 20(8):9249–9263, 2012.
- [142] A. F. Oskooi, D. Roundy, M. Ibanescu, P. Bermel, J. D. Joannopoulos, and S. G. Johnson. Meep: A flexible free-software package for electromagnetic simulations by the FDTD method. *Comp. Phys. Comm.*, 181(3):687–702, 2010.
- [143] I. Avrutsky, R. Gibson, J. Sears, G. Khitrova, H. M. Gibbs, and J. Hendrickson. Linear systems approach to describing and classifying fano resonances. *Phys. Rev. B*, 87:125118, 2013.
- [144] S. M. Spillane, T. J. Kippenberg, O. J. Painter, and K. J. Vahala. Ideality in a fiber-taper-coupled microresonator system for application to cavity quantum electrodynamics. *Phys. Rev. Lett.*, 91(4):043902, 2003.
- [145] C. Manolatou, M. J. Khan, S. Fan, P. R. Villeneuve, H. A. Haus, and J. D. Joannopoulos. Coupling of modes analysis of resonant channel add-drop filters. *IEEE J. Quantum Electron.*, 35:1322–1331, 1999.
- [146] M. Eichenfield, C. P. Michael, R. Perahia, and O. Painter. Actuation of micro-optomechanical systems via cavity-enhanced optical dipole forces. *Nat. Photon.*, 1:416–422, 2007.
- [147] S. G. Johnson and J. D. Joannopoulos. Block-iterative frequency-domain methods for maxwell’s equations in a planewave basis. *Opt. Express*, 8:173–190, 2001.

- [148] V. Tsvirkun, A. Surrente, F. Raineri, G. Beaudoin, R. Raj, I. Sagnes, I. Robert-Philip, and R. Braive. External control of dissipative coupling in a heterogeneously integrated photonic crystal—SOI waveguide optomechanical system. *Photonics*, 3(4):52, 2016.
- [149] M. Wu, N. L.-Y. Wu, T. Firdous, F. Fani Sani, J. E. Losby, M. R. Freeman, and P. E. Barclay. Nanocavity optomechanical torque magnetometry and rf susceptometry. *Nat. Nano.*, 2016.
- [150] M. Belov. *Spatiotemporal Magnetization Dynamics of Patterned Ni80Fe20*. PhD thesis, University of Alberta, 2004.
- [151] E. M. Chudnovsky and D. A. Garanin. Phonon superradiance and phonon laser effect in nanomagnets. *Physical Review Letters*, 93(25), 2004.
- [152] R. Jaafar, E. M. Chudnovsky, and D. A. Garanin. Dynamics of the einstein-de haas effect: Application to a magnetic cantilever. *Phys. Rev. B*, 79:104410, 2009.
- [153] D. C. Ralph and M. D. Stiles. Spin transfer torques. *J. Magn. Magn. Mater.*, 320:1190–1216, 2008.
- [154] F. Fani Sani, J. E. Losby, Z. Diao, L. C. Parsons, J. A. J. Burgess, D. Vick, W. K. Hiebert, and M. R. Freeman. Strong vortex core pinning and barkhausen-free magnetization response in thin permalloy disks induced by implantation of 1×10^4 Ga⁺ ions. *J. Appl. Phys.*, 115:17D131, 2014.
- [155] H. Barkhausen. Two phenomena uncovered with help of the new amplifiers. *Z. Phys*, 20(401), 1919.
- [156] Z. Diao, J. E. Losby, J. A. J. Burgess, V. T. K. Sauer, W. Hiebert, and M. R. Freeman. Stiction-free fabrication of lithographic nanostructures on resist-supported nanomechanical resonators. *J. Vac. S. Tech. B*, 31(5):051805, 2013.

- [157] J. D. Jackson. *Classical Electrodynamics*. Wiley, 1998.
- [158] J. Rigue, D. Chrischon, A. M. H. de Andrade, and M. Carara. A torque magnetometer for thin films applications. *J. Magn. Magn. Mater.*, 324:1561–1564, 2012.
- [159] J. E. Losby, J. A. J. Burgess, C. M. B. Holt, J. N. Westwood, D. Mitlin, W. K. Hiebert, and M. R. Freeman. Nanomechanical torque magnetometry of permalloy cantilevers. *J. Appl. Phys.*, 108(12):123910, 2010.
- [160] J. E. Losby, J. A. J. Burgess, Z. Diao, D. C. Fortin, W. K. Hiebert, and M. R. Freeman. Thermo-mechanical sensitivity calibration of nanotorsional magnetometers. *J. Appl. Phys.*, 111(7):07D305, 2012.
- [161] J. W. van Honschoten, W. W. Koelmans, S. M. Konings, L. Abelmann, and M. Elwenspoek. Nanotesla torque magnetometry using a microcantilever. In *Euroensors XXII, European Conference on Solid-State Transducers*, 2008.
- [162] X. Yin, Q. Jiao, L Yuan, and S.-H. Liou. Mems torsion oscillator magnetic field sensor. *IEEE Transactions on Magnetics*, 49:3890–3892, 2013.
- [163] H. J. Mamin, T. H. Oosterkamp, M. Poggio, C. L. Degen, C. T. Rettner, and D. Rugar. Isotope-selective detection and imaging of organic nanolayers. *Nano letters*, 9(8):3020–3024, 2009.
- [164] C. L. Degen. Scanning magnetic field microscope with a diamond single-spin sensor. *Appl. Phys. Lett.*, 92:243111, 2008.
- [165] J. M. Taylor, P. Cappellaro, L. Childress, L. Jiang, D. Budker, P. R. Hemmer, A. Yacoby, R. Walsworth, and M. D. Lukin. High-sensitivity diamond magnetometer with nanoscale resolution. *Nature Phys.*, 4(10):810–816, 2008.

- [166] J. R. Maze, P. L. Stanwix, J. S. Hodges, S. Hong, J. M. Taylor, P. Cappellaro, L. Jiang, M. V. Gurudev Dutt, E. Togan, A. S. Zibrov, A. Yacoby, R. L. Walsworth, and M. D. Lukin. Nanoscale magnetic sensing with an individual electronic spin in diamond. *Nature*, 455(7213):644–647, 2008.
- [167] G. Balasubramanian, I. Y. Chan, R. Kolesov, M. Al-Hmoud, J. Tisler, C. Shin, C. Kim, A. Wojcik, P. R. Hemmer, A. Krueger, T. Hanke, A. Leitenstorfer, R. Bratschitsch, F. Jelezko, and J. Wrachtrup. Nanoscale imaging magnetometry with diamond spins under ambient conditions. *Nature*, 455(7213):648–651, 2008.
- [168] P. Maletinsky, S. Hong, M. S. Grinolds, B. Hausmann, M. D. Lukin, R. L. Walsworth, M. Lončar, and A. Yacoby. A robust scanning diamond sensor for nanoscale imaging with single nitrogen-vacancy centres. *Nat. Nano.*, 7(5):320–324, 2012.
- [169] L. Rondin, J.-P. Tetienne, S. Rohart, A. Thiaville, T. Hingant, P. Spinicelli, J.-F. Roch, and V. Jacques. Stray-field imaging of magnetic vortices with a single diamond spin. *Nature Communications*, 4:2279, 2013.
- [170] J.-P. Tetienne, T. Hingant, J.-V. Kim, L. H. Diez, J.-P. Adam, K. Garcia, J.-F. Roch, S. Rohart, A. Thiaville, D. Ravelosona, et al. Nanoscale imaging and control of domain-wall hopping with a nitrogen-vacancy center microscope. *Science*, 344(6190):1366–1369, 2014.
- [171] T. Staudacher, F. Shi, S. Pezzagna, J. Meijer, J. Du, C. A. Meriles, F. Reinhard, and J. Wrachtrup. Nuclear magnetic resonance spectroscopy on a (5-nanometer) 3 sample volume. *Science*, 339(6119):561–563, 2013.
- [172] M. Grinolds, S. Hong, P. Maletinsky, L. Luan, M.D. Lukin, R. Walsworth, and A. Yacoby. Nanoscale magnetic imaging of a single electron spin under ambient conditions. *Nature Phys.*, 9:215–219, 2013.

- [173] C. Müller, X. Kong, J.-M. Cai, K. Melentijević, A. Stacey, M. Markham, D. Twitchen, J. Isoya, S. Pezzagna, J. Meijer, et al. Nuclear magnetic resonance spectroscopy with single spin sensitivity. *Nature Communications*, 5, 2014.
- [174] D. Rugar, H. J. Mamin, M. H. Sherwood, M. Kim, C. T. Rettner, K. Ohno, and D. D. Awschalom. Proton magnetic resonance imaging using a nitrogen-vacancy spin sensor. *Nat. Nano.*, 10:120–124, 2015.
- [175] M. Pelliccione, A. Jenkins, P. Ovartchaiyapong, C. Reetz, E. Emmanouilidou, N. Ni, and A. C. B. Jayich. Scanned probe imaging of nanoscale magnetism at cryogenic temperatures with a single-spin quantum sensor. *Nat. Nano.*, 2016.
- [176] J. Unguris. Scanning electron microscopy with polarization analysis (SEMPA) and its applications. In *Magnetic Imaging and its Applications to Materials*, volume 36. Academic Press, 2000.
- [177] D. Vasyukov, Y. Anahory, L. Embon, D. Halbertal, J. Cuppens, L. Neeman, A. Finkler, Y. Segev, Y. Myasoedov, M. L Rappaport, et al. A scanning superconducting quantum interference device with single electron spin sensitivity. *Nat. Nano.*, 8(9):639–644, 2013.
- [178] M. Rahm, J. Biberger, V. Umasky, and D. Weiss. Vortex pinning at individual defects in magnetic nanodisks. *J. Appl. Phys.*, 93:7429, 2003.
- [179] D. Antonio, M. I. Dolz, and H. Pastoriza. Micromechanical magnetometer using an all-silicon nonlinear torsional resonator. *Appl. Phys. Lett.*, 95(13):133505, 2009.
- [180] D. J. Bishop, C. A. Bolle, V. Aksyuk, F. Pardo, P. L. Gammel, E. Zeldov, E. Bucher, R. Boie, and D. R. Nelson. Observation of mesoscopic vortex physics using micromechanical oscillators. *Nature*, 399(6731):43–46, 1999.
- [181] A. Banholzer, R. Narkowicz, C. Hassel, R. Meckenstock, S. Stienen, O. Posth, D. Suter, M. Farle, and J. Lindner. Visualization of spin dynamics in single nanosized magnetic

- elements. *Nanotechnology*, 22(29):295713, 2011.
- [182] S. Tamaru, K. Yakushiji, A. Fukushima, S. Yuasa, and H. Kubota. Ultrahigh sensitivity ferromagnetic resonance measurement based on microwave interferometer. *IEEE Magnetism Letters*, 5:1–4, 2014.
- [183] M. R. Freeman. Cryogenic electronics. In Robert C. Richardson and Eric N. Smith, editors, *Experimental Techniques In Condensed Matter Physics At Low Temperatures*, volume 67 of *Frontiers in Physics*, pages 200–210. Addison–Wesley, 1988.
- [184] A. Vansteenkiste, J. Leliaert, M. Dvornik, M. Helsen, F. Garcia-Sanchez, and Bartel van Waeyenberge. The design and verification of mumax3. *AIP Advances*, 4:107133, 2014.
- [185] R. P. Cowburn, D. K. Koltsov, A. O. Adeyeye, M. E. Welland, and D. M. Tricker. Single-domain circular nanomagnets. *Phys. Rev. Lett.*, 82:1042, 1999.
- [186] R. L. Compton and P. A. Crowell. Dynamics of a pinned magnetic vortex. *Phys. Rev. Lett.*, 97:137202, 2006.
- [187] N. Abu-Libdeh and D. Venus. Dynamics of domain growth driven by dipolar interactions in a perpendicularly magnetized ultrathin film. *Phys. Rev. B*, 81:195416, 2010.
- [188] Y. Li, J. Zheng, J. Gao, J. Shu, M.S. Aras, and C.W. Wong. Design of dispersive optomechanical coupling and cooling in ultrahigh-Q/V slot-type photonic crystal cavities. *Opt. Express*, 18(23):23844–23856, 2010.
- [189] M. Davanço, J. Chan, A.H. Safavi-Naeini, O. Painter, and K. Srinivasan. Slot-mode-coupled optomechanical crystals. *Opt. Express*, 20(22):24394–24410, 2012.
- [190] M. Matsuo, J. Ieda, and S. Maekawa. Mechanical generation of spin current. *Frontiers in Physics*, 3:54, 2015.

- [191] S. A. Tadesse, H. Li, Q. Liu, and M. Li. Acousto-optic modulation of a photonic crystal nanocavity with lamb waves in microwave k band. *Appl. Phys. Lett.*, 107(20):201113, nov 2015.
- [192] X. Zhang, C. L. Zou, L. Jiang, and H. X. Tang. Cavity magnomechanics. *Sci. Adv.*, 2(3):1501286, 2016.
- [193] A. Hryciw. Raith_gdsii matlab toolbox. https://github.com/nrc-cnrc/Raith_GDSII. Accessed: 2016-10-03.
- [194] M. A. Mohammad, T. Fito, J. Chen, M. Aktary, M. Stepanova, and S. K. Dew. Interdependence of optimum exposure dose regimes and the kinetics of resist dissolution for electron beam nanolithography of polymethylmethacrylate. *Journal of Vacuum Science & Technology B: Microelectronics and Nanometer Structures*, 28(1):L1, 2010.
- [195] I. Yu. Evchuk, R. I. Musii, R. G. Makitra, and R. E. Pristanskii. Solubility of polymethyl methacrylate in organic solvents. *Russian Journal of Applied Chemistry*, 78(10):1576–1580, oct 2005.

Appendix A

List of publications

M. Wu, N. L.-Y. Wu, T. Firdous, F. Fani Sani, J. E. Losby, M. R. Freeman, P. E. Barclay. *Nanocavity Optomechanical Torque Magnetometry and Radiofrequency Susceptometry*, Nature Nanotechnology. Published October 31, 2016.

C. Healey, H. Kaviani, **M. Wu**, B. Khanaliloo, M. Mitchell, A. C. Hryciw, P. E. Barclay. *Design and Experimental Demonstration of Optomechanical Paddle Nanocavities*, Appl. Phys. Lett. **107**, 231107. Published December 10, 2015.

A. C. Hryciw, **M. Wu**, B. Khanaliloo, P. E. Barclay. *Tuning of Nanocavity Optomechanical Coupling using a Near-field Fiber Probe*. Optica **2**, 491-496. Published May 14, 2015.

H Kaviani, C. Healey, **M. Wu**, R. Ghobadi, P. E. Barclay. *Nonlinear Optomechanical Paddle Nanocavities*. Optica **2**, 271-274. Published March 20, 2015.

M. Wu, A. C. Hryciw, C. Healey, D. P. Lake, H. Jayakumar, M. R. Freeman, J. P. Davis, P. E. Barclay. *Dissipative and Dispersive Optomechanics in a Nanocavity Torque Sensor*. Phys. Rev. X **4**, 021052. Published June 19, 2014.

Appendix B

Numerical simulations using COMSOL

This appendix gives practical instructions to calculate parameters related to the optical, mechanical, and optomechanical properties of our devices. The numerical simulations presented here were performed using a commercial software, COMSOL, on a 96 Gb memory desktop computer. The steps described here are compatible from version 4.2 until the latest release in version 5.0. The model used as an example here is a nanobeam photonic crystal cavity with a breathing mode as mechanical mode (see Fig. B.1).

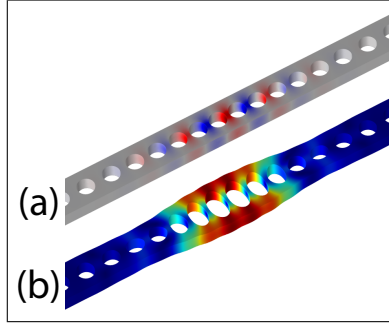


Figure B.1: Numerical simulation of the (a) optical mode and the (b) mechanical mode (here a breathing mode) of a nanobeam photonic crystal cavity.

Optomechanical coupling

The optomechanical coupling g_{om} from moving boundaries is expressed as [59]:

$$g_{om} = \frac{\omega_o}{4} \int dA (\mathbf{u}_n \cdot \hat{\mathbf{n}}) \left[\Delta\epsilon |\mathbf{e}_{\parallel}|^2 - \Delta(\epsilon^{-1}) |\mathbf{d}_{\perp}|^2 \right] \quad (\text{B.1})$$

where ω_o is the optical resonance frequency and the integral is performed over the surface dA of the device. Inside the integral, the overlap of the mechanical mode \mathbf{u}_n and the optical field represented by the parallel electric and perpendicular displacement fields, \mathbf{e}_{\parallel} and \mathbf{d}_{\perp} ,

will involve two computation steps inside the same model. The first requires the Solid Mechanics module while the second requires the Electromagnetic Waves module, both using an eigenfrequency solver.

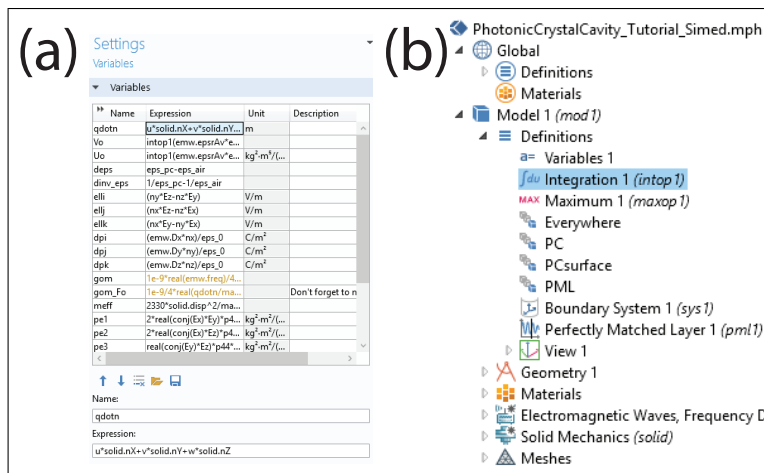


Figure B.2: (a) Settings for the variables under the definitions of the model. These variables can use built-in expressions in COMSOL. (b) Important definitions are the integral and the maximum. The first is defined over the surface of the device (PCsurface) while the latter is defined over globally (Everywhere).

After defining the geometry, materials, and mesh for the device, including a perfectly matched layer on the outer boundaries, the following variables must be added to the definitions of the model as shown in Fig. B.2. The expression $\mathbf{u}_n \cdot \hat{\mathbf{n}}$ is defined as the dot product of the mechanical mode and the surface normal. The refractive index contrast of the optical cavity, $\Delta\varepsilon = \varepsilon_1 - \varepsilon_2$ and $\Delta(\varepsilon^{-1}) = \varepsilon_1^{-1} - \varepsilon_2^{-1}$, where $\varepsilon_{1,2}$ are the dielectric constants of the structure (silicon here) and the surrounding medium (air), respectively. The electric field is a cross product $\mathbf{e}_{\parallel} = \mathbf{n} \times \mathbf{e}$ while the displacement field is a dot product $\mathbf{d}_{\perp} = \mathbf{n} \cdot \mathbf{d}$. The expressions for each of the mechanical and optical fields must be normalized such that the first term is divided by the maximum displacement and the second is divided by the optical energy $\frac{1}{2} \int \epsilon(r) E^2$ [59].

It is often the case that a single optical mode can couple to many mechanical modes. Moreover, the numerical simulation of optical mode consume more computation time than for

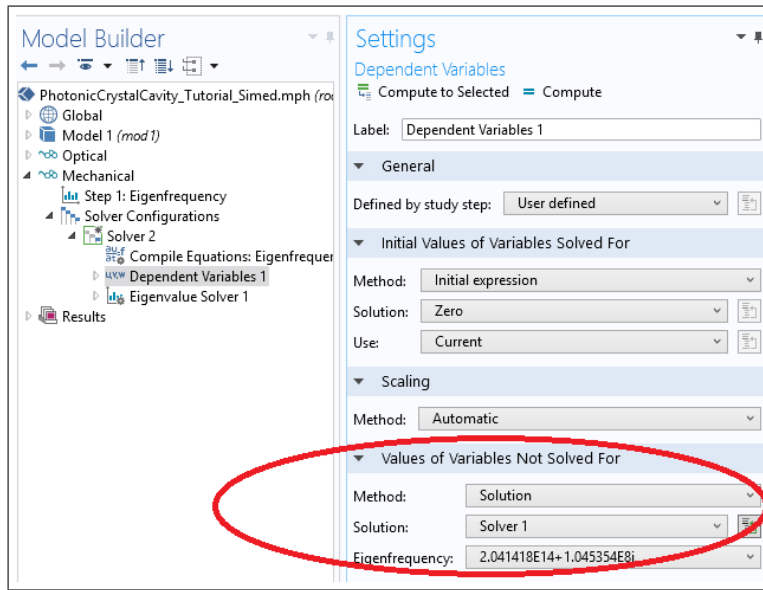


Figure B.3: Settings inside the Solid Mechanics solver in COMSOL. Under dependent variables, solution from the desired optical mode is added before solving for the mechanical mode.

a mechanical mode using the same mesh. Therefore it is typical to first solve for the optical mode. After the desired eigenfrequency solution is found, the crucial step for calculating g_{om} involve adding the solution for the optical mode to the solver for the mechanical mode as shown in Fig. B.3. The solver will then proceed to compute for mechanical modes while storing the solution of the optical mode.

After both solutions are found, the value of g_{om} can be extracted by creating a derived value under the result section (Fig. B.4). Since the full expression of g_{om} (without integral) was defined earlier in the model variables, surface integration is chosen and g_{om} is directly written in the expression box. The surface of the device is chosen as the integration domain. Once the expression is evaluated, the value of g_{om} will appear on a table. This method can also be used to compute the photoelastic coefficient g_{pe} [62].

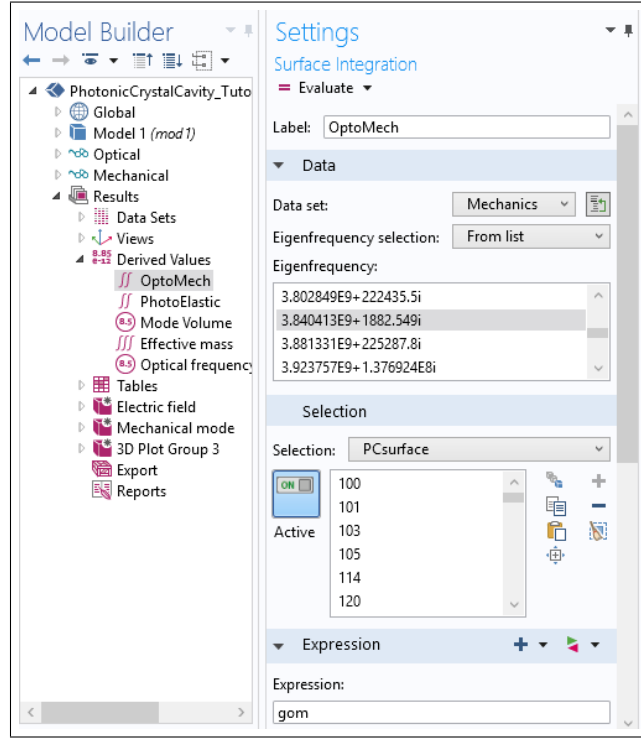


Figure B.4: Settings in COMSOL showing the result section. User created expressions must be extracted in the Derived Values sub-menu.

Calculating effective mass

The effective mass m_{eff} for a particular mechanical mode is given by [59]:

$$m_{\text{eff}} = \rho \int dV \left(\frac{|\mathbf{u}|}{\max(|\mathbf{u}|)} \right)^2 \quad (\text{B.2})$$

where $\rho(r)$ is the density of the material, \mathbf{u} is the mechanical displacement computed earlier, and the denominator is a normalization factor. The volume integral is performed over the whole computational domain.

Using the same steps for calculating g_{om} , the effective mass can be extracted by selecting volume integral over all domains. The m_{eff} is displayed in Fig. B.5 for the breathing mode.

Eigenfrequency	m _{eff} (m ³)
3.840413E9+1882.549i	261.0331

Figure B.5: Table of results from derived values in COMSOL. The value for effective mass m_{eff} in femtograms is calculated here.

Calculating mode volume

The mode volume V_o of the optical field is a general indication of the strength of light-matter interactions inside a cavity. It describes the effective volume occupied by the optical mode; a smaller value points to stronger field confinement. The effective mode volume can be defined as:

$$V_o = \int dV \frac{\varepsilon |\mathbf{E}|^2}{\max(\varepsilon |\mathbf{E}|^2)} \quad (\text{B.3})$$

where \mathbf{E} is the electric field and the denominator is a normalization factor. V_o is usually expressed in units of $(\lambda_o/n)^3$, where λ_o is the optical resonance and n is the index of refraction of the material. The effective mode volume is computed similarly to the effective mass.

Calculating mode overlap efficiency

The efficiency η_n of a mode overlap quantifies the amount of commonality between two modes, whether it be optical or mechanical. A high efficiency (η_n near 1) indicates stronger energy transfer between modes. Its importance can be observed in coupled modes inside a waveguide or the effectiveness of an applied driving force unto a mechanical mode. η_n is given by

$$\eta_n = \frac{\int dV \mathbf{u}_1(x) \mathbf{u}_2(x)}{\sqrt{\int dV \mathbf{u}_1(x)^2 \int dV \mathbf{u}_2(x)^2}} \quad (\text{B.4})$$

where \mathbf{u}_1 and \mathbf{u}_2 are the overlapping modes over a geometrical extent x (field profile or domain) and the denominator is a normalization factor. In COMSOL, the extraction of two modes consists of a “Join” operation on the data set to explicitly combine two solutions. These two modes can originate from any solver for the same structure and mesh. The overlap efficiency can be calculated by creating a volume integral in the derived values and an expression calling for the first mode (“data1”) and the second mode (“data2”) as shown in Fig. B.6.

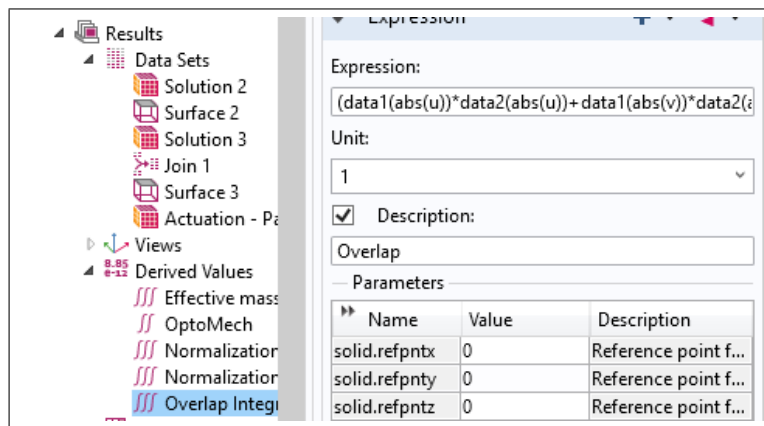


Figure B.6: Settings in COMSOL showing the result section. A “Join” operation combines two solutions from the same solver. An overlap integral uses data from both.

Appendix C

Signal processing

The following appendix gives details on the derivation of power spectral density during signal processing in the real-time spectrum analyzer (RSA).

The RSA demodulates the time-series voltage $V(t)$ and outputs IQ data, $V_{IQ}(t) = I(t) - iQ(t)$, where $I(t) = \cos(\omega_c t)V(t) * h(t)$ and $Q(t) = \sin(\omega_c t)V(t) * h(t)$. Here ω_c is the demodulation frequency, and $h(t)$ is a low-pass anti-aliasing filter, whose span is determined by the sampling rate (up to 40 MHz). The Fourier transform of the IQ data is related to the input spectrum by $\bar{V}_{IQ}(\omega) = V(\omega + \omega_c)H(\omega)$. Note that a scaling factor is built into $H(\omega)$ to ensure that $|\bar{V}_{IQ}(\omega - \omega_c)|^2$ can be accurately treated as a single-sided (positive frequency) representation of the symmetrized input power spectrum.

The two-sided power spectral density of the optomechanical contribution to input signal is given by

$$S_{VV}^{\text{om}}(\omega) = |V_{\text{om}}(\omega)|^2 / RBW, \quad (\text{C.1})$$

where RBW is the resolution bandwidth used in the RSA and $V_{\text{om}}(\omega)$ is the Fourier transform of the time-series optomechanical signal such that $V(\omega) = \int_0^{\Delta t} dt e^{-i\omega t} V(t)$. For clarity, the DC component is ignored in the following analysis. Using Eq. (2.17), S_{VV}^{om} can be related to the stochastically varying displacement $x(t)$ of the nanocavity,

$$S_{VV}^{\text{om}}(\omega) = \left(\eta_{\text{qe}} g_{\text{ti}} P_{\text{det}} \frac{d\Gamma(\lambda)}{dx} \right)^2 \frac{1}{\Delta t} \left| \int_0^{\Delta t} dt e^{-i\omega t} x(t) \right|^2 \quad (\text{C.2})$$

$$= \frac{G^2}{\Delta t} \int_0^{\Delta t} dt' \int_{-t'}^{\Delta t - t'} dt e^{-i\omega t} x^*(t' + t)x(t'), \quad (\text{C.3})$$

where G is the optomechanical gain described in chapter 2 and describes the detector and optomechanical response. The stationary nature of $x(t)$, i.e., $\langle x^*(t + t')x(t) \rangle = \langle x^*(t')x(0) \rangle$

for measurement time $\Delta t \gg 2\pi/\gamma_m$, allows us to write the above equation as

$$S_{VV}^{\text{om}}(\omega) = G^2 \int_0^{\Delta t} dt' e^{-i\omega t'} \langle x^*(t+t')x(t) \rangle \quad (\text{C.4})$$

$$= G^2(\lambda) S_{xx}(\omega), \quad (\text{C.5})$$

where $S_{xx}(\omega)$ is the displacement noise spectral density of the mechanical resonator. The total single-sided power spectral density measured by the RSA is

$$\bar{S}_{VV}(\lambda, \omega) = G^2(\lambda) \bar{S}_{xx}(\omega) + \bar{S}_{VV}^{\text{n}}(\lambda, \omega), \quad (\text{C.6})$$

where the contribution from the technical noise is labeled $\bar{S}_{VV}^{\text{n}}(\lambda, \omega)$. Note that the spectral density can also be expressed as true power over a load resistance Z such that $\bar{S}_p = \bar{S}_{VV}/Z$ in units of W/Hz or dBm/Hz.

Appendix D

Nanofabrication tools and processes

The operation of nanofabrication tools and the processes involved in fabricating devices described in this thesis are detailed here. Our typical samples are 1 cm² chips diced from a SOI (silicon-on-insulator) wafer with a 220 nm layer of silicon on top of a 3 μm layer of buffer oxide.

Piranha cleaning

Piranha cleaning is a oxidizing etch process used to eliminate undesirable organic compounds on substrates. The mixture is a combination of 3:1 sulfuric acid (H₂SO₄) and hydrogen peroxide (H₂O₂). The samples must be immersed the piranha solution for 15 minutes. For less than 4 chips, blue tweezers are used to hang the chips inside a glass beaker. For 5 and 8 chips, they can be inserted vertically in individual slots of a small honeycomb tray that can be then put inside a beaker with appropriate size. For a large number of chips, a larger matrix tray with a cover on top and a rectangular glass container must be used. After piranha, the samples are rinsed with water five times and dried with nitrogen gas (N₂).

Photoresist deposition

Photoresists (resist for short) are deposited or coated on the chip using two Brewer tools at the UofA nanoFab: a spinner and a hotplate.

ZEP coating

To deposit 300-400 nm of ZEP-520A resist, the hotplate is first set to 180 °C. After grabbing the ZEP resist bottle from the fridge, the following items are also needed: a pipette, 2 metal tweezers with flat pads, a timer, and a small glass bowl. The coating recipe in the Brewer machine is named "AHRYCIW_ZEP". The main step in the process is a 40 s spin cycle at more than 4,000 rpm. There are short ramp up cycles (100 rpm) before and after. The sample must be carefully aligned on the suction pad inside the spinner followed by activation of the vacuum. Using the pipette, 3 drops of ZEP are added on the chip. After closing the lid, start the recipe. Once the recipe ends, the chip is carefully and slowly transferred to the hotplate. The timer is now set to 5 minutes. Many chips can be coated in sequence while others are baking on the hotplate as long as time is kept for each one. After 5 minutes on the hotplate, the chips are carefully removed using metal tweezers and onto a clean paper towel for cooling. A glass bowl is used to cover the chips. Once the chips are cooled, they can be retrieved into a sample holder.

PMMA bi-layer coating

The procedure for depositing PMMA bi-layer are similar to the instructions for ZEP. PMMA A2 495k and PMMA A8 950k can be found in the resist cabinet. PMMA A2 is first coated on the chip at 4,000 rpm for 45 s then baked at 180 °C for 5 minutes. After cooling, PMMA A8 is deposited as a second layer also at 4,000 rpm for 45 s and baked. This yields many hundreds of nanometers of thick resist used for a lift-off process.

Electron beam lithography

Electron beam lithography is the defining step in the process where the design pattern is transferred to the photoresist using a raster beam of electrons. In the UofA nanoFab, this

Cycle	Voltage	Aperture	Area dose	Line dose	Dot dose	Step size
1	30 kV	10 μm	80 $\mu\text{C}/\text{cm}^2$	200 pC/cm	0.005 pC	10 nm
2	10 kV	10 μm	120 $\mu\text{C}/\text{cm}^2$	200 pC/cm	0.005 pC	10 nm

steps uses a Raith 150-Two machine. The table below lists the settings used for exposure in each cycle. The first cycle described in chapter 3 defines the optomechanical device while the second cycle is for the addition of permalloy (chapter 6).

With an area dose of 80 pC/cm² in the first cycle, the dose factor to clear for large areas is about 4.0, and about 3.5 for small holes with large areas in close proximity (e.g., holes in a nanobeam). A value of 0.005 pC is generally used when manually writing ellipses as ensembles of single-pixel dots, to allow for a reasonably high dot density (e.g., 10 nm spacing) while maintaining an overall areal ellipse dose factor of 3.5.

To generate the design pattern, a Matlab script for was used to write GDSII files from the toolbox developed in-house by Aaron Hryciw [193].

Cold development of ZEP photoresist

The ZEP resist must be developed in order to reveal the pattern exposed by the electron beam lithography step. For high-quality and high-resolution patterns with sharp resist walls, a cold development process was created at the UofA nanoFab under the direction of Mohammad Ali Mohammad [194]. The solvent for ZEP is the ZED-N50 developer solution and the equipment is a Stir-Kool SK-12D cold plate.

The cooling process must be started 30 minutes before the end of the lithography step. First, the valve for the water flow must be flipped on. Two 50 ml beakers, with the bottom grinded for thermal contact, are used: one for 15 ml of ZED-N50 and the other for 15 ml of IPA. A custom-made foam box with two inserts for the beakers is placed over the cold plate. 5 drops of silicone oil is added in each of the opening before inserting the two beakers

in the foam box. The bottom of the beaker should have optimal contact with the cold plate via the silicone oil by avoiding the formation of small bubbles. After adding small magnetic stir bars (1 cm) in each beaker, a thermometer probe connected to the tool is inserted inside the beaker with ZED. Finally, the cold plate can be turned on. The stirring level is set to 60 and the temperature is set to -15 °C. After 20 minutes, the temperature reading should reach less than -13 °C.

After retrieving the sample from the lithography tool, the chip is dipped in the cold ZED-N50 solution for 20 s followed by a 20 s dip in the IPA solution. Then the chip is dried with nitrogen.

Resist development of PMMA bi-layer

Samples with PMMA bi-layer can be developed in a typical wet deck in a photolithography area. First the chip is dipped in a solution of 3:1 MIBK/IPA for 60 s, followed by a dip in IPA for 20 s, and then dried with nitrogen.

Silicon etching

Reactive ion etching (RIE) was used to transfer the pattern from the photoresist to the layer of silicon using Oxford Instruments PlasmaLab System 100 inductive coupled plasma RIE (ICPRIE). The recipe in the tool is called “Si Mixed Etch - Opt 1”. The chamber must first be conditioned using the recipe for 10 minutes on a dummy wafer. The sample is attached to a carrier wafer using a small dot of vacuum grease (silicone). The specimen should be flat against the wafer with no grease exposed. After conditioning, the chip is loaded and the recipe is run again with an etch time of 45 s.

The etching recipe mixes two gases: 16 sccm of SF₆ and 12 sccm of C₄F₈. These gases are ionized inside the chamber with an RF power of 25 W and a ICP power of 3,500 W. In each

run, the helium gas leakage flow must be less than 10 sccm and the chuck temperature near 15 °C for optimal operation. After unloading, the chip can be removed and its underside cleaned with IPA to remove grease residue.

Silica undercut

The buffer oxide layer is undercut in order to release the free-standing silicon structures. To remove the silicon dioxide (or silica SiO_2), a concentrated solution of hydrogen fluoride (HF) at 49% purity will quickly etch a 3 μm layer in less than 90 seconds. Teflon containers should be used instead of glass since the latter will be eaten away by the HF. Only a small container and small quantity of HF are necessary for a small chip. The sample is then quickly transferred to 2 large Teflon beakers filled with water, plunging the chip in water for some time before moving to the other one. Caution must be taken and proper personal protective equipment worn at all times when manipulating HF. The leftover HF and its container must be neutralized with copious amount of calcium chloride. The wet deck is then thoroughly cleaned with water. Fragile samples with long suspended structures can be transferred within a liquid environment to a critical point dryer for a slower and controlled release to avoid stiction.

Ultra-high vacuum permalloy thin film deposition

Thin films of permalloy ($\text{Ni}_{80}\text{Fe}_{20}$) are deposited using a ultra-high vacuum evaporator EFM 3, Omicron Vakuumphysik GMBH, with base pressure down to 10^{-10} Torr [24]. Located in the laboratory of Dr. Freeman, the tool consists of a loadlock chamber, a rotating transfer arm, and a deposition chamber. The loadlock chamber is pumped down in two steps, the first with a rough pump down to $10^{-4} - 10^{-6}$ Torr then with a turbo pump to at least below 10^{-8} Torr. At the same time, the sample is baked at 70 °C to remove traces of volatile

compounds which might outgas inside the vacuum chamber. The pumping process is usually left to run overnight.

After high vacuum is obtained, the sample is transported from the loadlock to the deposition chamber using a rotating transfer arm system. A high voltage (up to 0.8 kV) is applied to the permalloy to be deposited which is in the form of a rod. The deposition process is a delicate series of steps to prepare and condition the electron gun. High current (up to 2 A) runs through a filament placed near the rod. The resulting electron beam causes heating on the tip of the permalloy rod producing evaporation of the material. The gas of permalloy is then guided down a collimation tube to the target.

The rate of deposition (0.3 – 3.5 nm per minute) varies with the applied current as well as conditions inside the chamber and the permalloy rod. The deposited films are smooth to approximately 0.3 nm average roughness. Typical thickness deposited range from 10 to 80 nm.

PMMA bi-layer lift-off

A lift-off process is used to remove unwanted permalloy on top of the PMMA bi-layer while leaving patterned permalloy on top of the targeted locations. The process involves a heated solution of Remover-PG although more potent solvents for PMMA exist such as trichloromethane and trichloroethylene [195].

A large glass beaker, with enough Remover-PG solution to immerse the chips suspended by tweezers, is heated on a hot plate to 70 °C. The lift-off should last about 30 minutes with a stir rod slowly agitating the solution. A warning is given here: do not use acetone once permalloy is deposited with resist on the chip. The combined reaction leaves insoluble residue on the sample.

Appendix E

Coupled mode theory including indirect coupling

In this appendix, we show modifications to the usual waveguide–cavity temporal coupled mode theory to include indirect coupling between the cavity and the fundamental waveguide mode, mediated by higher-order modes of the waveguide.

The detected optical signal consists of the output field in the fundamental mode of an optical fiber taper waveguide positioned in the near field of the optical cavity. The polarization of this mode is chosen to maximize its coupling to the cavity. The modal output amplitude is

$$t_o = s_o + \kappa_{co}a + \kappa_{c+}a, \quad (\text{E.1})$$

where s_o is the input field amplitude and a is the cavity field amplitude. Coupling from the cavity field into the fundamental fiber taper mode is described by coupling coefficients κ_{co} and κ_{c+} . κ_{co} describes coupling from the cavity directly into the fundamental fiber taper mode, while κ_{c+} describes coupling into higher-order modes of the fiber taper which are converted into the fundamental mode along the length of the fiber taper. Typically $|\kappa_{c+}| \ll |\kappa_{co}|$, as both the cavity to higher-order mode coupling process and the fiber taper higher-order to fundamental mode conversion rates are small.

The cavity field amplitude is governed by the equation of motion,

$$\frac{da}{dt} = -(i\Delta + \frac{\gamma_t}{2})a + \kappa_{oc}s_o \quad (\text{E.2})$$

where $\Delta = \omega_l - \omega_c$ is the detuning between the input field laser and the cavity frequency, and κ_{oc} is the fiber to cavity coupling coefficient. The total cavity optical loss rate is given by

$$\gamma_t = \gamma_{i+p} + 2\gamma_e \quad (\text{E.3})$$

where γ_e is the coupling rate into the forward (or backward) propagating mode of the fiber taper, and γ_{i+p} describes the intrinsic cavity loss and fiber-induced parasitic loss into modes other than the fundamental fiber taper mode, e.g., scattering into radiation modes and light coupled into higher-order fiber modes which are not converted into the fundamental waveguide mode within the fiber taper.

In the steady state, $\dot{a} = 0$, and the cavity field amplitude is:

$$a = \frac{\kappa_{oc} s_o}{i\Delta + \frac{\gamma_t}{2}}. \quad (\text{E.4})$$

In the case of a two-port coupler, unitarity requires that $\kappa_{oc} = -\kappa_{co}^* = i\sqrt{\gamma_e}$ for the phase convention chosen in Eq. (E.1). Assuming that the correction due to coupling to higher-order taper modes considered here is small, so that the above relationship still holds, the transmitted field is

$$t_o = s_o \left(1 - \frac{\gamma_e + \kappa_{oc}\kappa_{c+}}{i\Delta + \frac{\gamma_t}{2}} \right). \quad (\text{E.5})$$

A key property of the output coupling mediated by the higher-order waveguide mode is that *a priori* the complex phase of κ_{c+} is not defined relative to the phase of κ_{oc} , as it depends on the modal coupling process between the cavity's coupling region and the fiber taper. This variable phase leads to a non-Lorentzian cavity response, as seen by writing $\kappa_{c+} = \kappa_+^r + i\kappa_+^i$ where κ_+^r and κ_+^i are both real, and calculating the normalized taper transmission:

$$T = \frac{\Delta^2 + \left(\frac{\gamma_{i+p}}{2}\right)^2 + 2\sqrt{\gamma_e}\kappa_+^r\Delta - \sqrt{\gamma_e}\kappa_+^i\gamma_{i+p}}{\Delta^2 + \left(\frac{\gamma_t}{2}\right)^2}, \quad (\text{E.6})$$

where we have only kept terms to lowest order in $\kappa_+^{i,r}$. For weak fiber-cavity coupling, $\gamma_e \ll \gamma_{i+p}$, the last term in the denominator can be ignored, and

$$T \sim \frac{\Delta^2 + \left(\frac{\gamma_{i+p}}{2}\right)^2 + C_f\gamma_e\Delta}{\Delta^2 + \left(\frac{\gamma_t}{2}\right)^2}, \quad (\text{E.7})$$

where $C_f = 2\kappa_+^r/\sqrt{\gamma_e}$ represents a Fano modification to the cavity response mediated by the higher-order fiber taper modes and is expected to be small.

Appendix F

Copyright permissions

Paper published in Physical Review X

From the website of the American Physical Society, publisher of the Physical Review X journal:

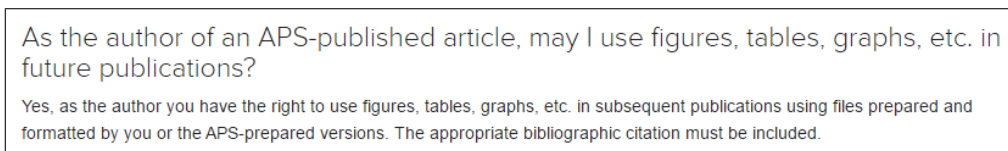


Figure F.1: Screenshot capture of the American Physical Society website page pertaining to copyright permission for use of manuscript in a thesis. Date: November 17, 2016

Paper published in Optica

From the website of the Optical Society of America, publisher of the Optica journal:

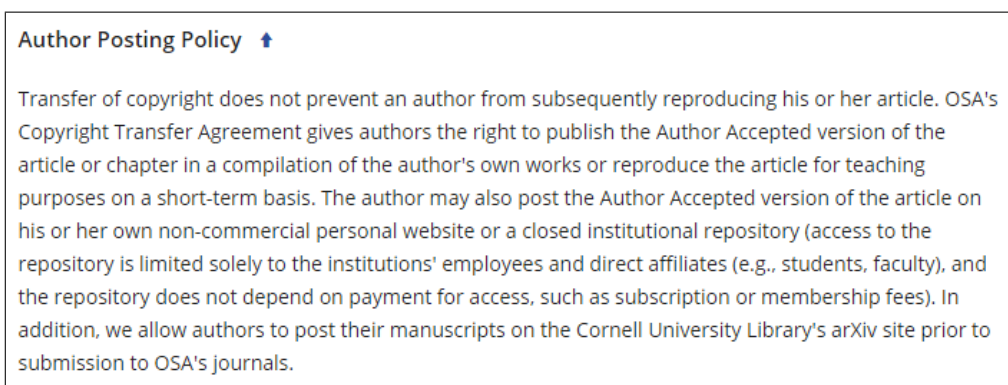
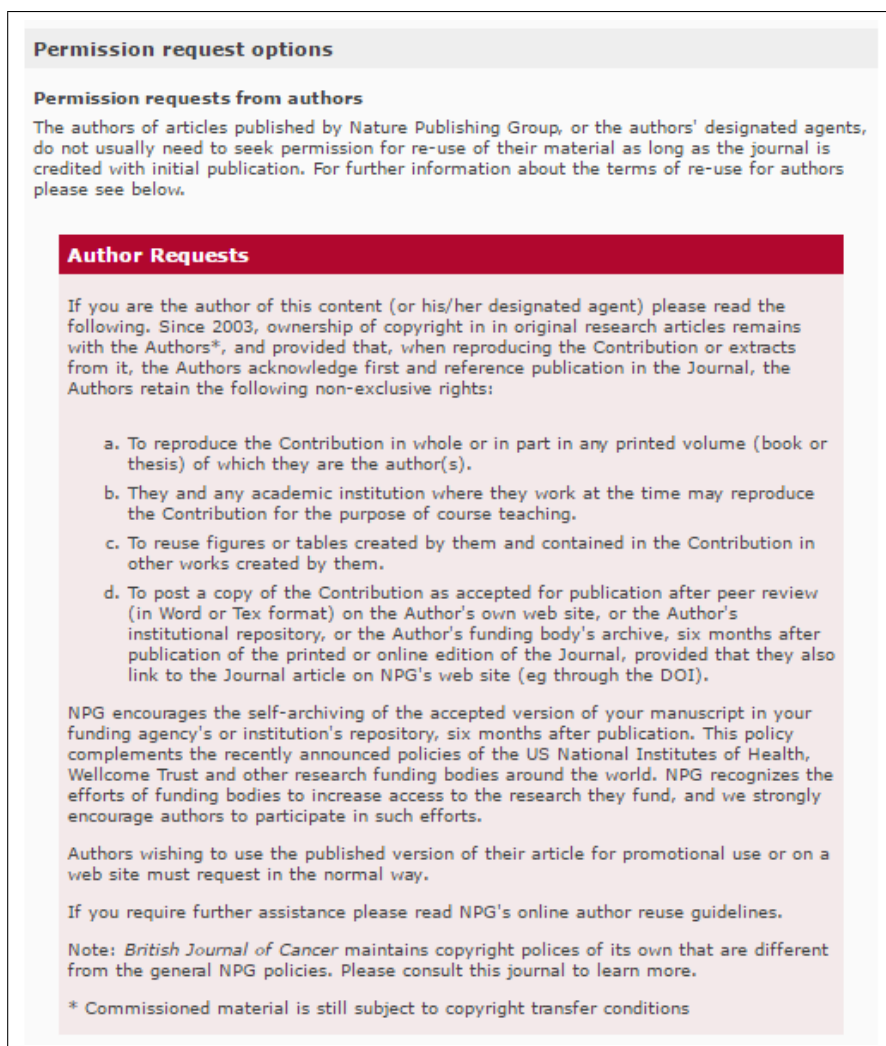


Figure F.2: Screenshot capture of the Optical Society of America website page pertaining to copyright permission for use of manuscript in a thesis. Date: November 17, 2016

Paper published in Nature Nanotechnology

From the website of the Nature Publishing Group, publisher of the Nature Nanotechnology journal:



Permission request options

Permission requests from authors

The authors of articles published by Nature Publishing Group, or the authors' designated agents, do not usually need to seek permission for re-use of their material as long as the journal is credited with initial publication. For further information about the terms of re-use for authors please see below.

Author Requests

If you are the author of this content (or his/her designated agent) please read the following. Since 2003, ownership of copyright in original research articles remains with the Authors*, and provided that, when reproducing the Contribution or extracts from it, the Authors acknowledge first and reference publication in the Journal, the Authors retain the following non-exclusive rights:

- To reproduce the Contribution in whole or in part in any printed volume (book or thesis) of which they are the author(s).
- They and any academic institution where they work at the time may reproduce the Contribution for the purpose of course teaching.
- To reuse figures or tables created by them and contained in the Contribution in other works created by them.
- To post a copy of the Contribution as accepted for publication after peer review (in Word or Tex format) on the Author's own web site, or the Author's institutional repository, or the Author's funding body's archive, six months after publication of the printed or online edition of the Journal, provided that they also link to the Journal article on NPG's web site (eg through the DOI).

NPG encourages the self-archiving of the accepted version of your manuscript in your funding agency's or institution's repository, six months after publication. This policy complements the recently announced policies of the US National Institutes of Health, Wellcome Trust and other research funding bodies around the world. NPG recognizes the efforts of funding bodies to increase access to the research they fund, and we strongly encourage authors to participate in such efforts.

Authors wishing to use the published version of their article for promotional use or on a web site must request in the normal way.

If you require further assistance please read NPG's online author reuse guidelines.

Note: *British Journal of Cancer* maintains copyright policies of its own that are different from the general NPG policies. Please consult this journal to learn more.

* Commissioned material is still subject to copyright transfer conditions

Figure F.3: Screenshot capture of the Nature Publishing Group website page pertaining to copyright permission for use of manuscript in a thesis. Date: November 17, 2016